

UNIVERSITY OF BREMEN



MASTER'S THESIS

**Near-surface turbulent fluxes at Kohnen Station
on the East Antarctic Plateau**

Isabell Sonntag

Supervisor:
Dr. Christof Lüpkes

Examiners:
Prof. Dr. Thomas Jung
PD Dr. Ulrike Wacker



February 2017

This master's thesis is submitted for the degree of
M.Sc. in Environmental Physics.

The programme is a cooperation between the
Institute for Environmental Physics (IUP) at the University of Bremen
and the
Alfred Wegener Institute (AWI), Helmholtz Centre for Polar and Marine Research,
Bremerhaven.

The thesis has been prepared in the Polar Meteorology group of the AWI Bremerhaven.

Abstract

The longest ever obtained in-situ turbulence time series at Kohnen Station in Dronning Maud Land, East Antarctica is analysed under the aspect of Monin-Obukhov similarity theory (MOST). The latter forms the basis for the commonly used parametrization schemes for near-surface turbulent fluxes in numerical weather prediction and climate models. Based on the turbulence data and measurements of mean meteorological variables that have been obtained during the campaign from 10 Dec 2013 to 31 Jan 2014, the general meteorological situation and daily evolution of the lower boundary layer is described. We find the measurement period to be representative for summertime conditions at Kohnen Station with a shallow but dynamic boundary layer which is moderately stable at night and slightly unstable during daytime. Average diurnal amplitudes of near-surface temperature and wind speed amount to 10 K and 3 m/s. Different MOST stability functions are compared with those based on the measured momentum and sensible heat fluxes under both stable and unstable stratification. For this purpose, aerodynamic roughness length and temperature roughness length are determined but show to be quite variable. To consider MOST stability functions derived from our measurements we employ a new straight-forward method that uses one measurement level only (instead of usually two). We find that by this method the obtained scatter is large so that a conclusion on the optimal function is not possible. Nevertheless, we show that bulk approaches based on drag coefficient including traditional stability functions can reproduce the measured momentum fluxes well under stable conditions if an aerodynamic roughness length of the order of 10^{-5} m is employed. However, for friction velocities larger than 0.16 m/s the momentum flux under stable conditions is slightly underestimated. Another result of the present study is that the measured functional dependence between the stability parameter z/L and the bulk Richardson number agrees very well with the one shown by Grachev et al. (2007, SHEBA data) under stable conditions. Since the relation between z/L and Ri_B also depends on MOST stability functions, this result suggests the applicability of the Grachev stability functions under stable conditions for the location of Kohnen Station.

The worse agreement for momentum flux parametrization under unstable conditions and also for heat flux parametrization in general based on the initially used single-level method may be due to measurement uncertainties. However, it may also hint at limits of the applicability of MOST for the special and extreme conditions on the high Antarctic plateau.

Acknowledgements

I want to thank the Polar Meteorology Group for their kind and engaged support while working on this thesis. Each member contributed with their knowledge and experience to progress in different parts of this very challenging work. Especially, I want to thank my supervisor Dr. C. Lüpkes for his readiness and time for discussions that have been very helpful on this foreign ground. Since I could not be at the AWI for most of the time, I missed the pleasant working atmosphere of this institute very much. I also want to thank the PHAROS group of the IUP for giving me the opportunity to gain very worthwhile experience in Python programming prior to this thesis. Special thanks go to my friends and family that have been very understanding for my lack of time and always supported me in what I do. At last, my greatest appreciation must go with Stefan and our small growing miracle for staying strong and understanding even during the most frustrating and difficult times. You are my light.

Table of Contents

Abstract	v
Acknowledgements	vii
Table of Contents	ix
List of Figures	xiv
List of Tables	xv
List of Abbreviations	xvii
1 Introduction	1
2 Conditions at Kohnen Station	5
2.1 General information	5
2.2 Climatology	7
2.2.1 Near-surface variables	7
2.2.2 Boundary Layer	9
3 Instrumentation	13
3.1 Instrumentation and data sets	13
3.2 The Sonic	15
3.2.1 General comments	15
3.2.2 Measuring principle	16

4	Theoretical background	21
4.1	Surface layer theory	21
4.2	Monin-Obukhov similarity theory	23
4.3	Bulk transfer relations	27
5	Data preparation	29
5.1	Derivation of surface temperature from longwave radiation	29
5.2	Quality control of AWS air temperature	30
5.3	From raw Sonic data to turbulent fluxes using the eddy covariance method	35
5.3.1	The eddy covariance method	35
5.3.2	Data processing of Sonic raw data	37
5.3.3	Quality control of Sonic data	44
5.3.4	On the use of Theta instead of T	45
5.3.5	Sonic parameter test: Averaging interval	45
6	Results	49
6.1	Meteorological conditions	49
6.1.1	Near-surface variables	49
6.1.2	Summer warming event	52
6.1.3	Boundary layer evolution	53
6.2	Near-surface turbulent fluxes	57
6.2.1	Daily cycle	57
6.2.2	Negative CH values and thermal emissivity of the snow surface .	59
6.2.3	Data selection criteria	63
6.2.4	Stability parameters	64
6.2.5	Roughness lengths and neutral bulk transfer coefficients	65
6.2.6	Parametrization of turbulent surface fluxes	70
7	Conclusion	83
A	Derivation of wind speed and temperature from sonic travel times	89
A.1	Derivation of wind speed from sonic travel times	89
A.2	Derivation of temperature from sonic travel times	90
B	Stability functions according to MOST	91
C	Test of different filter frequencies for FFT (Sonic high-pass filter)	95
D	Time series graphs	99
E	Linear depiction of measured ψ_M	103

Bibliography	104
---------------------	------------

Declaration of Authorship	113
----------------------------------	------------

List of Figures

2.1	6
3.1	Bird's eye view of Kohnen Station	14
3.2	Sonic photo	17
5.1	Corrected AWS temperature time series, 1 min resolution	31
5.2	Temperature differences from Sonic and AWS, plotted together with wind speed	32
5.3	Temperature differences from Sonic and AWS, 4 days close-up	33
5.4	Scatter plot of temperature differences from Sonic and AWS against wind speed	34
5.5	Eddy covariance method	36
5.6	Calibrated and corrected upward and downward sonic travel times	39
5.7	Sonic wind and temperature data in instrument's reference frame	39
5.8	40
5.9	Wind components in streamline coordinates for one hour (i.e. after rotation).	41
5.10	Wind components in streamline coordinates for 13 Dec 2013 (i.e. after rotation).....	41
5.11	Filtered wind components in streamline coordinates for one hour.	42
5.12	Results from Sonic data, based on a fixed density (0.956 kg/m^3 as the mean density during the measurement period, calculated using AWS data).	44
5.13	Influence of averaging length on flux outcome	47
6.1	Daily cycle of near-surface variables	51
6.2	Summer warming event	53
6.3	Mean radiosounding profiles	54

6.4	Radiosounding profiles from 6 days	55
6.5	Potential inertial oscillation in wind profile	56
6.6	Daily cycle of turbulence related quantities in the surface layer	58
6.7	Negative C_H episodes with $\varepsilon=0.97$	60
6.8	Negative C_H episodes with $\varepsilon=1.0$	61
6.9	Retrieval of longwave surface emissivity by minimizing the duration of negative C_H episodes	62
6.10	Connection of the two stability parameters ζ and Ri_B and histograms . . .	65
6.11	Determination of z_0	67
6.12	Neutral transfer coefficient for heat	69
6.13	Measured stability function for momentum vs. z/L (loglog)	71
6.14	Measured stability function for heat vs. z/L (loglog)	72
6.15	Friction velocity parametrization via ζ	77
6.16	Friction velocity parametrization via Ri_B	78
D.1	Time series of main meteorological quantities	100
D.2	Time series from Neumayer Station	101
D.3	Time series of turbulence related quantities	102
E.1	Measured stability function for momentum vs. z/L (linear)	103

List of Tables

3.1	Available data sets and instrumentation	15
6.1	Monthly means of meteorological and turbulence quantities	80
6.2	Neutral bulk transfer coefficients	81

List of Abbreviations

ABL	A tmospheric b oundary l ayer
AWI	A lfred W egener I nstitute, H elmholtz C entre for P olar and M arine R esearch
FFT	F ast F ourier T ransform
LLJ	L ow-level j et
MOST	M onin- O bukhov S imilarity T heory
SBL	S table b oundary l ayer
SHF	S ensible h eat f lux
SL	S urface l ayer
TKE	T urbulent k inetic e nergy

CHAPTER 1

Introduction

The atmospheric boundary layer (*ABL*) is the lowermost portion of the atmosphere which is in direct contact with the Earth's surface and thus rapidly reacts to changes at the ground. Through this layer, the free atmosphere and the surface exchange energy, momentum and moisture e.g. from vegetation, soil or ocean. These exchanges in the form of fluxes are most effectively achieved by turbulence which dominates the *ABL*'s dynamics and is usually continuously present (Stull, 1988). Turbulence time scales range from fractions of a second to one hour while the corresponding length scales of these chaotic motions cover a millimeter up to the depth of the boundary layer or even more in the case of convective clouds (Holtslag et al., 2013). With the development of ground-based remote sensing techniques (e.g. sodar) and in-situ measurement techniques that allow for a sufficient temporal resolution of relevant quantities such as wind speed or temperature, the extensive investigation of the *ABL* began in the late 1960s. Major contributions for the understanding of the *ABL*'s dynamics could be achieved within a decade. In recent years, boundary layer research and the improvement of *ABL* representation in models became not less important. A typical area of application is in air quality investigations. Emitted gaseous and particulate matter are transported within the *ABL* and undergo chemical reactions, distinctively determining air quality in cities and having a potential impact on areas far away from the emitter. Apart from the prediction and study of weather and climate, a correct representation of the *ABL* in models is also important for the field of wind energy. Forces onto the blades and the potential energy that can be gained at a particular site must be evaluated for successful projects.

Turbulence time and length scales are not resolved by numerical weather prediction and

climate models but these subgrid features do have an impact on the large-scale flow (see e.g. Holtslag et al., 2013). Apart from that, turbulent flux terms arise in the set of Reynolds-averaged equations in models. A closure scheme is needed to make up for these additional terms. The turbulent fluxes (e.g. of momentum and sensible heat) between the surface and lower atmosphere thus must be parametrized in the models what is commonly done in terms of the available averaged quantities. Different approaches are in use for that. An established method is the Monin-Obukhov similarity theory *MOST* (Monin and Obukhov, 1954) which predicts the existence of universal functions for turbulence parametrization within the surface layer (a lower layer of the ABL where fluxes are approximately constant with height (Stull, 1988)). In a different form, it is also regularly applied to the complete ABL. Usually based on measurements performed in the mid-latitudes, many functions (so-called flux-profile relationships) have been developed through the decades while some of them, e.g. the Dyer-Businger relations (Dyer, 1974, Businger et al., 1971) are widely accepted and used today. The type of turbulence schemes used for ABL representation in models has a large impact on the modelled momentum and sensible and latent heat transfers between the surface and the atmosphere and, together with other factors, controls the diurnal cycle of near-surface variables such as temperature and wind speed. This in turn influences the modelled lifetime and activity of synoptic-scale systems. Modeled temperature trends also showed to partly depend on the choice of turbulence parametrization (see e.g. Holtslag et al., 2013, who summarizes findings from several publications). Based on the results of numerous studies, the latter also conclude that especially the modelling of a (very) stably stratified lower atmosphere still needs further advances for an improved representation of near-surface variables, vertical mean profiles, turbulent fluxes and their diurnal cycles. Models showed to be very sensitive to the choice of flux-profile relationship functions within the ABL under stable conditions. Modelled boundary layer heights in stable conditions are typically too large and low-level jets often too weak owing to an overestimated turbulent mixing. A reduced turbulent mixing can in turn lead to a decoupling, followed by an unphysical runaway cooling at the ground. In the very stable regime, turbulence parametrization still remains a challenge and is subject to ongoing research.

In polar regions, very stably stratified ABLs occur frequently. During the last decades, research proved that Antarctica plays a major role in the global energy budget and climate system because it is a major heat sink. Even in mid-summer, the Antarctic continent can absorb only little short-wave radiation because of its polar location and high reflectivity of its thick snow pack. That causes only weak buoyancy-driven turbulent mixing compared to lower latitudes, allowing the Antarctic ABL to be only a few hundred meters thick at maximum, in contrast to a few kilometers which is the typical magnitude in the mid-latitudes (e.g. van As et al., 2006, Bonner et al., 2010, Argentini et al., 2013). Due to a negative

surface radiation budget, the Antarctic ABL is mostly stable (a temperature inversion is found above the surface) although in summer convective (unstable) conditions dominate near the surface during the day under solar insolation while upward sensible heat fluxes remain very small (e.g. Argentini et al., 2013, van den Broeke et al., 2005, Vignon et al., 2016). During winter (polar night), the ABL over the plateau is generally stably stratified with average inversion strengths of 1 Kelvin per meter in the lower 45 meters (Genthon et al., 2013, at Dome C). Turbulent mixing in such very stable conditions is weak or even intermittent (sporadic) (e.g. Mauritsen and Svensson, 2007) which makes a correct representation of the stable boundary layer (*SBL*) in models difficult. The development of a low-level jet (*LLJ*), gravity waves and meandering motions can induce shear that is larger than the near-surface wind shear and therefore cause the established ABL theory to fail (e.g. Mahrt, 1999). In addition, fog and dew formation and drainage flows (katabatic winds) can additionally complicate SBL modelling (e.g. Holtslag et al., 2013). In combination with the large size of the Antarctic continent (it makes up about 10% of the global landmass area (King and Turner, 1997), errors in heat or momentum flux parametrization for this region can increase the uncertainty in regional and global model outcomes. Therefore it is very worth investigating whether the common ways of turbulence parametrizations can be applied for this region.

This task is difficult to fulfill for the Antarctic continent. Although more than 50 automatic weather stations have been run operationally in 1995, the Antarctic interior is still generally little observed (King and Turner (1997, ch. 2) and van den Broeke et al. (2005)) which can be a problem for the initialization and validation of regional climate and weather models as well as for global climate models. In-situ turbulence measurements from the Antarctic interior (e.g. Vignon et al., 2016) are also very rare although the growth of SBL research in the last decade increased the number of field campaigns in polar regions. They are more often conducted on shelf ice (e.g. Handorf et al., 1999, Rodrigo and Anderson, 2013) or above Arctic pack ice (e.g. Grachev et al., 2007) than above the remote, highly-elevated inland ice plateau of Antarctica (e.g. Genthon et al., 2013, van As et al., 2006, Bonner et al., 2010, Gallée et al., 2015, Pietroni et al., 2014, investigation of the Dome C area dominates because a 45 m high tower with continuous meteorological observations is available since 2009). The Antarctic plateau offers ideal conditions for SBL research because of its horizontal homogeneity and vast and flat landscape. But on the other hand, application of the established theory and flux measurements can be corrupted by katabatic winds, non-stationarity due to the diurnal cycle (which is weak in polar winter) and phenomena typical to SBLs as mentioned before. In very stable conditions, communication to the surface may be impeded which also fails the assumptions of the classical MOST (see z-less concept, e.g. Monin and Obukhov, 1954 and Mahrt, 1999).

One objective of the present study is testing classical parametrizations for the surface layer especially under weakly to very stable conditions using turbulence measurements from the 2013/2014 summer campaign at Kohnen Station, Dronning Maud Land on the East Antarctic plateau. The common way of testing these flux-profile relationships is based on temperature and wind profiles gained from a tower which is several tens of meters high, with at least two measurement levels within the surface layer. This study, however, attempts testing the functions in their integrated form because only one measurement height is available. This will be done using a straight-forward method that, to our knowledge, has not been applied before. Other studies that are based on single level data use the so-called bulk method (van den Broeke et al., 2005, e.g.) which yields turbulent fluxes from single level wind speed and temperature (and surface temperature).

A three-axis sonic anemometer-thermometer (type uSonic-3 Scientific) by Metek GmbH was employed to determine vertical turbulent fluxes of momentum and sensible heat via the common eddy covariance (or eddy correlation) method. These measurements were taken in about two meters height for a continuous period of 53 days. This data set is very special because in fact, only one case of earlier in-situ turbulence measurements at Kohnen Station could be found in existing literature (van As et al., 2005, 2006, one month in summer 2002). However, in contrast to the present study, they employ the bulk method and do not compare different parametrizations. Apart from turbulent fluxes, bulk transfer coefficients for momentum and heat (depending on stability) and the local aerodynamic roughness length will be determined from the high-response measurements. Together with vertical profiles of temperature and wind speed gained from radiosoundings four times a day, they also serve for describing the state of the boundary layer at Kohnen Station, including a description of thermal stratification via Obukhov length and bulk Richardson number. Furthermore, automatic weather station data, upward and downward longwave radiation and cloud and precipitation records are available to quantify the surface temperature and describe the general meteorological situation at the site.

CHAPTER 2

Conditions at Kohnen Station

This chapter shall give an overview of the campaign's objectives and the meteorological and surface conditions at the measurement site, including knowledge about the ABL over Antarctic plateau stations.

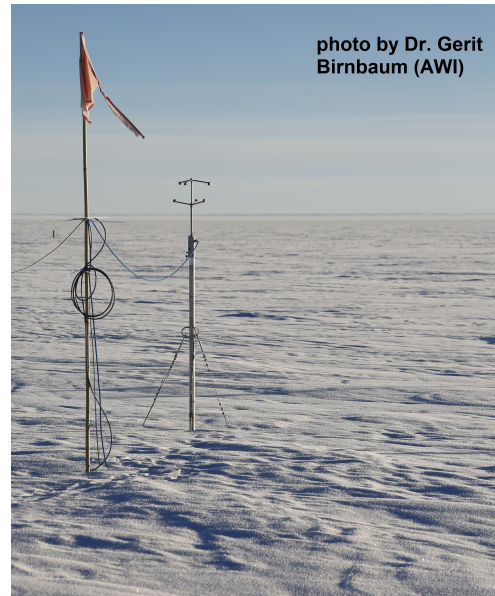
2.1 General information

All data used in this study have been measured at the German research station Kohnen (at 75°00'S, 00°04'E) in December 2013 and January 2014 during the summer expedition "ANT-Land 2013/2014 - Kohnen Station, Dronning Maud Land" that focussed on snow, firn and albedo investigations. The main responsibility of the expedition lay with Dr. Gerit Birnbaum (AWI Bremerhaven) who, together with Michael Schäfer (PhD student at LIM Leipzig), performed the on-site set up and attendance of all installations during the campaign. The preparation of instruments and planning of the measurement set-up has been realized by her, Bernd Loose, Dr. Gert König-Langlo, Wolfgang Cohrs and Dr. Christof Lüpkes (all AWI Bremerhaven).

The overarching research project of the expedition is the CoFi ("Coldest Firn") project of the AWI. CoFi focusses on glaciological work such as core drilling and is part of PACES II ("Polar Regions And Coasts in a changing Earth System") of the Helmholtz Community. A sub-project of CoFi is AISAS (a DFG project) which profited from measurements of snow properties taken during the expedition. AISAS stands for "Coupling of Airborne and In situ ground based measurements of Surface albedo, BRDF and snow properties in Antarctica to improve prognostic Snow models" and is a cooperation between the University of Leipzig



(A) Location of Kohnen on the Antarctic continent. (Source: http://www.awi.de/fileadmin/user_upload/AWI/Expedition/Stationen/Bild/Kohnen/Antarctica_Kohnen.jpg)



(B) The ultrasonic anemometer-thermometer (*Sonic*) during the summer campaign 2013/2014 at Kohnen Station

FIGURE 2.1

and the AWI. A variety of ground-based meteorological measurements were performed for this project. These data are the basis of the study at hand. (Sources: Birnbaum (2013), Bremerhaven and personal communication with Dr. Birnbaum)

Kohnen Station is of exceptional importance since it is one of the very few research stations on the Antarctic ice sheet that can accommodate a research team (up to 20 people) over a longer period of time, but only during the Antarctic summer. It was established in 2001 and is run by the AWI (Bremerhaven). It is located at a height of 2892m above sea level on the plateau of Dronning Maud Land, East Antarctica (see Figure 2.1a). Being located close to an ice divide, it played a key role for the European deep ice-core drilling project EPICA (1996-2005) (Bremerhaven). The ice below the station is slowly drifting into south-west direction towards the Filchner Ice Shelf. The station is regularly supplied by a convoy of caterpillar-track vehicles that need roughly ten days to arrive from Neumayer III Station which is located about 760 kilometres northwest from Kohnen Station on the Ekström shelf ice (Bremerhaven).

The area around the remote inland station is very flat, fully snow covered, without any vegetation or animal life. The closest nunataks (exposed rock) or mountainous areas are located about 250 kilometres northward (Birnbaum, 2013) and the minimum distance to the shelf edge or the South Atlantic coast line is about 550 kilometres in summer. Figure 2.1b shows the sonic anemometer-thermometer in front of the flat horizon. The station's distance to the South Pole causes a marked daily cycle in the incoming short-wave radiation

in summer. Together with the small but significant surface slope of $1.3 \pm 0.3\text{m/km}$ (sloping up toward the east-northeast), this location is representative for a large part of the Antarctic plateau (van As et al., 2006). The vast flat and uniform landscape makes it a "natural laboratory" for stable boundary layer research (cf. Grachev et al., 2007).

2.2 Climatology

2.2.1 Near-surface variables

Radiative cooling in the polar regions is generally strong, creating a stably stratified lower atmosphere for most of the year (see e.g. King and Turner, 1997). At Kohnen Station the energy loss due to an imbalance of absorbed short-wave radiation and outgoing long-wave radiation amounts to 6.9W/m^2 (van den Broeke et al., 2005, average for 1998-2001) and is compensated by sensible, latent and subsurface conductive heat fluxes in order to maintain a surface energy balance.

Due to the sloping surface in combination with the prevailing stable stratification of the lower atmosphere, a large part of the Antarctic continent experiences cold and dry katabatic winds which are directionally steady at each location (see e.g. Ball, 1956, van den Broeke and van Lipzig, 2003). At Kohnen Station, they blow from a generally northeast direction since the large-scale topography rises towards east (the winds turn left under the influence of the Coriolis force), with a katabatic acceleration of up to $2.7\text{m s}^{-1}\text{h}^{-1}$ (van As and van den Broeke, 2006, modelling result). These downslope winds are weaker in the Kohnen plateau area (and above the coastal ice shelf) than they are in areas of strong surface slope at the edge of the ice sheet, the so-called katabatic wind zone. There, strong katabatic winds lead to a strong vertical mixing which brings warmer air from higher atmospheric levels towards the surface and therefore maintain higher near-surface temperatures than on the plateau and keep differences between summer and winter temperatures smaller (van den Broeke et al., 2005). The long-term mean of the 2m wind speed at Kohnen is 4.5m/s with a standard deviation of only 2.4m/s (van As et al., 2007, AWS measurements 1998-2004) and a mean direction of 57° (van As et al., 2006, 1998-2001), both without any significant seasonal cycle. The circumpolar pressure trough along the coast north of Antarctica supports this directional constancy of the near-surface wind on the synoptic scale by creating a westward geostrophic wind at the site (van As et al., 2005).

The temperature curve, in contrast to the wind speed, exhibits clear seasonality with daily mean 2m temperatures of -51°C in mid-winter and -26°C in mid-summer (van As et al., 2007). In mid-winter however, the temperature curve does not show the typical winter

minimum but the seasonal trend disappears. This behaviour is common for the Antarctic plateau and is referred to as "coreless winter" (Pietroni et al., 2014, observations at Dome C). The near-surface summertime temperature and wind speed (but not wind direction) show marked diurnal cycle which is a common feature at all plateau stations (Gallée et al. (2015) and Argentini et al. (2013) for Dome C; van As et al. (2005) for Kohnen Station). Due to the very low temperatures, relative humidities are high (on average 93 % with respect to ice, van den Broeke (2005)) and specific humidities are very low, typically ranging from 0.5 g/kg in summer to less than 0.1 g/kg in winter (van As et al., 2006). Saturation is reached easily under these temperature conditions in combination with radiative cooling, hence clear-sky precipitation (diamond dust) is a common precipitation type which causes very small and barely detectable snow accumulation (Reijmer and van den Broeke, 2003). Due to the low water content in the air, latent heat fluxes are very small as well ($<1 \text{ W/m}^2$, van As et al. 2006). Clear-sky conditions prevail since the general cloud cover is rather low with cloud fractions below 40 % to be present for about 70 % of the time (van den Broeke et al., 2006). The snow surface is rather firm due to the comparably low wind speeds and because the snow layer above the firm is thin. Ripples are a common surface type. Sastrugi (grooves in snow surface that are carved by wind) and snow dunes of different sizes do occur around Kohnen Station but they are shallower than the usual depths of those features in coastal areas. (Information on surface characteristics from Birnbaum et al., 2010, and personal communication, see also Van As et al. (2005)).

Generally, the elevated interior of the continent is only very seldom subject to transient cyclonic low-pressure systems as it is shielded by the escarpment zone of the ice shield (Carleton and Carpenter, 1990, Sinclair, 1994). Large systems or blocking highs located in front of the Antarctic coast can nevertheless create synoptic-scale disturbances that influence the plateau regions as well, but this happens only several times per year (e.g. Birnbaum et al., 2006, van As et al., 2006). Those events are connected to a significant warming of the lower atmosphere and the surface, increased cloud cover, stronger near-surface winds and precipitation (e.g. van den Broeke et al., 2006, van As et al., 2007). Overcast conditions have their largest impact on the near-surface temperature at night due to the increase of downwelling longwave radiation. Especially under the influence of high-pressure anomalies, significant warming events occur frequently during the winter season, with a usual duration of four to seven days and rapid temperature increases by up to 40°C (Argentini et al., 2001, Dome C). During summer days, clouds do not enforce a cooling of the lower atmosphere in contrast to most other regions on the globe because of the high shortwave reflectivity of the area (see radiation paradox, e.g. van As et al. (2005, 2007)). At Kohnen, they even lead to an increase in daytime temperatures and the diurnal cycle is maintained (although weaker) in contrast to locations in the katabatic wind zone where the diurnal

cycle almost vanishes (van den Broeke et al., 2006).

Precipitation generally decreases towards the Antarctic interior (Wacker et al., 2006, Reijmer and van den Broeke, 2003). The usual daily precipitation rate at Kohnen is very small with a water equivalent of the order of 0.1 mm for most days (Schlosser et al., 2010). Snowfall events exceeding 1 mm w.e. already are heavy precipitation events at Kohnen (Birnbaum et al., 2006, Schlosser et al., 2010). The long-term mean precipitation in the Kohnen area is about 62 mm water equivalent per year (Oerter et al., 2000). Reijmer and van den Broeke (2003) found the mean accumulation from 1998 to 2001 to be 81 mm w.e. per year (corresponding to less than 25 cm of snow) while more than half the annual accumulation is created during less than 10 high-precipitation events per year (see also Schlosser et al., 2010, Noone et al., 1999). Those events mainly originate from amplified upper-level wave patterns which cause relatively warm and moist air from the South Atlantic Ocean to arrive onto Dronning Maud Land by an unusual northerly flow (Noone et al., 1999, Birnbaum et al., 2006, Schlosser et al., 2010), e.g. due to a blocking high east of Kohnen or a strong cyclone over the ocean the frontal system of which still impacts the plateau. Another more exceptional origin of precipitation are large-scale lifting processes due to an upper air low in the vicinity of Kohnen (westerly flow from the Weddell Sea, Birnbaum et al. (see 2006), Schlosser et al. (see 2010)).

2.2.2 Boundary Layer

Atmospheric data directly measured at Kohnen Station are very limited. But the general behaviour of the ABL above the Antarctic plateau is known from studies conducted at other plateau stations and can, with some limitations, be transferred to the location of Kohnen. Dome C (the French-Italian Concordia Station, an EPICA site as well) located at 75.1°S, 123.3°E, 3233 m a.s.l. served for several research studies focussing on the lower atmosphere (e.g. Gallée et al., 2015) since a measurement tower of almost 50m height is constantly available.

A surface-based temperature inversion is the typical feature of polar ABLs. It is caused by the negative net radiation at the surface and is only seldom supported by the advection of warm air above the cold surface (Pietroni et al., 2014, van As et al., 2006). During the winter months, a long-lived stable boundary layer (*SBL*) exists with very large inversion strengths (temperature difference between inversion top and surface) of about 20°C at Dome C (Pietroni 2014) and at the South Pole (Phillpot and Zillman, 1970). At the same time, the surface-based inversion is about 200 m thick (deduced from monthly mean profiles) at Dome C (Pietroni et al., 2014) and 500-700 m thick at the South Pole (Phillpot

and Zillman, 1970). During polar night, the day-time temperature profile does not differ from the nocturnal profile since insolation is absent (Pietroni et al., 2014, investigations at Dome C). The strongest inversions occur under clear-sky conditions and low wind speeds since radiative cooling becomes especially strong under these conditions. Decreasing inversion strengths on the other hand are observed when wind speed increases (causing enhanced shear and vertical turbulent mixing) or when clouds are present (because the surface is warmed) (e.g. Pietroni et al., 2014). In general, vertical turbulent exchange in the Antarctic ABL is maintained by wind shear, i.e. it is mechanically induced, and thus strongly dependent on the katabatic forcing. For an only weakly sloping plateau, this implies comparably small turbulent fluxes (cf. van den Broeke et al., 2005). Due to negative buoyancy, turbulence under stable stratification is reduced and therefore boundary layer heights in winter are very low, commonly smaller than 50 m at Dome C and smaller than 20 m at Dome A where ABL thicknesses in June 2009 do not exceed 30 m (Bonner et al., 2010). In such very stable regimes with large vertical temperature and wind speed gradients, turbulence becomes too weak in a certain height to maintain the communication to the surface. This leads to the decoupling of the lower ABL from the free atmosphere (Argentini et al., 2013, Gallée et al., 2015).

In the summer months, the temperature profile and thus ABL structure and stability above the Antarctic interior vary with a marked diurnal cycle (e.g. Hudson and Brandt, 2005), similar to what we observe at mid-latitudes (Argentini et al., 2005). Under the influence of solar insolation, a weakly unstable surface layer develops daily, allowing the formation of a shallow mixing layer (also called convective layer) with a maximum height of 200-300 m (Dec/Jan) at Dome C (Mastrantonio et al., 1999, Argentini et al., 2005) and 70 m at Kohnen Station (van As et al., 2006, referring to a 4-day period in Feb 2002). At the time of the maximum depth of the mixing layer in the afternoon, relative humidity (with respect to ice) reaches its minimum value, for Kohnen this means 92%, as found by (van As et al., 2006) during the investigated four day period. Above the mixing layer, stratification remains moderately stable throughout the day and the amplitude of the diurnal cycle decreases with height (Pietroni et al., 2014, van As et al., 2006). Hence, stable conditions prevail within the summer as well, being most intense during night-time when the stable layer thickens and reaches saturation. Inversion strengths are 0 to 15 °C (Dec/Jan average: 3.2 °C) with inversion thicknesses of 5 to 105m (Dec/Jan average: 87m) (Pietroni et al., 2014) for Dome C and less than 50 m for Kohnen Station (van As et al., 2006, beginning of February). Large-scale subsidence is present at Kohnen due to the divergence of the katabatic wind field but it creates only neglectable heating rates (smaller than 0.4 K per day) compared to the large temperature changes in the ABL during summer days. Therefore it has no significant influence on the summertime ABL structure and dynamics (van As and

van den Broeke, 2006, model results).

A low-level jet is observed at Kohnen regularly during summer nights between 20 and 70 meters altitude. It is most likely katabatically driven due to an increasing surface based temperature inversion over night (see van As et al., 2006). A similar behaviour has been frequently observed at Dome C during a campaign from the beginning of November until the end of January (Gallée et al., 2015). Wind maxima in the ABL can potentially be created by inertial oscillations as well, as found by van As and van den Broeke (2006) using a high-resolution one-dimensional atmospheric model which has been validated and initiated by observations.

Van As et al. (2005) used one month of measured flux data gained during the ENABLE campaign at Kohnen Station in 2002 to validate a bulk MOST method to calculate surface sensible heat fluxes based on one-level AWS data. Using this method, van den Broeke et al. (2005) calculated year-round surface sensible heat fluxes at Kohnen using four years of 3 m height AWS measurements recorded about 2 km away from the station. They find an average downward sensible heat flux (*SHF*) in the ABL with an annual mean of 8 W/m^2 which contrasts the usually upwards direction of this flux in other regions of the globe. The reason for this is the predominantly stable stratification, causing negative buoyancy. The cooling surface layer gains some of the lost heat back from downward heat fluxes that transport heat down from the warmer atmosphere aloft. Due to stronger winds and a rougher surface, turbulent mixing in the katabatic wind zone is larger than on the plateau, causing the SHF to be $22\text{-}24 \text{ W/m}^2$ on average (van den Broeke et al., 2005). Increased katabatic winds due to the stronger near-surface temperature inversion in winter are also the reason for enhanced SHF at Kohnen in winter, when (van den Broeke et al., 2005) calculated monthly means slightly larger than 10 W/m^2 . Summertime SHF at Kohnen are smaller, with daily mean values between -10 and $+10 \text{ W/m}^2$ and even a net upward SHF for a short period during summer (van As et al., 2005). The strongest daytime convection occurs under enhanced wind conditions and in the presence of clouds which limit nocturnal cooling of the surface (see van den Broeke et al., 2006).

In conclusion, the summertime ABL (when defined by turbulence strength) is several hundred metres deep during the day and at maximum several tens of metres deep during the night. Near-surface turbulent fluxes increase with wind speed but remain small on the Antarctic plateau compared to the katabatic wind zone or mid-latitude climates and we expect a nocturnal LLJ. Overcast conditions are associated with enhanced precipitation and cause a surface warming which especially reduces the night-time vertical temperature difference. Turbulence measurements at Kohnen have so far only been performed by one

research group for the duration of one month which is why independent measurements are important.

CHAPTER 3

Instrumentation

3.1 Instrumentation and data sets

The station's containers are oriented in a line perpendicular to the steady katabatic winds which blow from a generally northeast direction since the large-scale topography rises towards east (the winds turn left under the influence of the Coriolis force). The same is true for the lineup of instruments in order to enable measurements to be solely influenced by the unperturbed upstream clean area (see bird's-eye view in Figure 3.1). This is especially important for the measurement of turbulent eddies which generally do not originate from the very location of measurement but rather from hundreds of meters away. All episodes during which the flow may be disturbed by other instruments or the station's containers will be excluded for the results of this study (by employing wind direction data from the AWS).

All data were accessed through Dr. Gerit Birnbaum. Table 3.1 summarises all available data sets and instruments used for this study.

All instruments have been serviced regularly during the campaign. In order to minimize the creation of rime onto the glass hemisphere of the pyrometers, they have been ventilated (but not heated). This method was effective. The main rack of the framework for radiation measurements (carrying other radiation instruments as well) is directed north. Since the sun rises along a northern path, shadows of the framework are cast southwards and not onto the surface area for the radiation measurements. The temperature and humidity sensor of the AWS are housed in a highly-reflective radiation shielding that has louvres for passive ventilation. An additional active ventilation would have been too energy expensive. Relative humidity is measured with respect to liquid water and will later be converted into

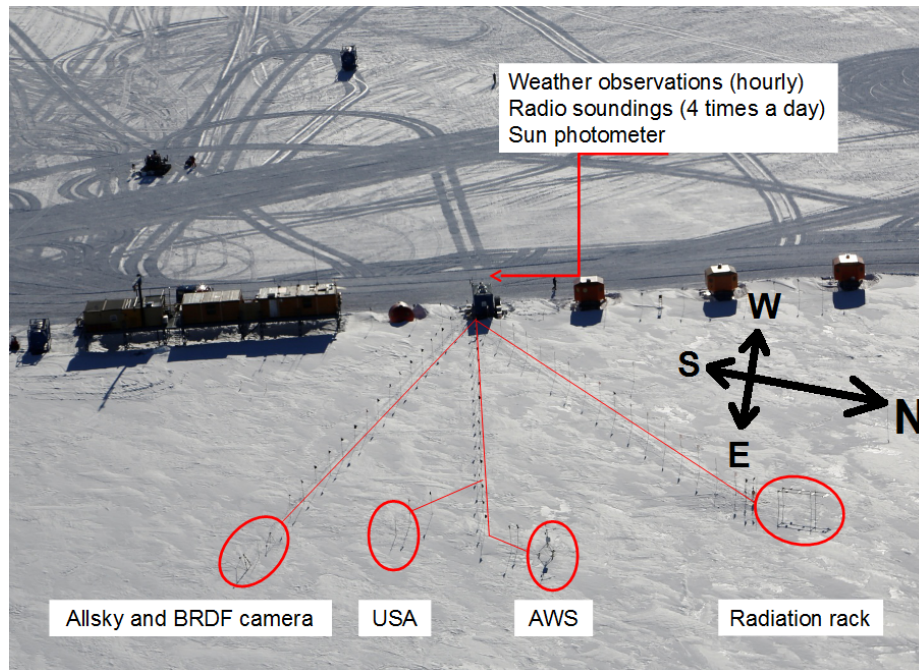


FIGURE 3.1: Bird's eye view of Kohnen Station with measurement area during the summer campaign 2013/2014. The main racks of the radiation framework are directed north. "USA" means ultrasonic anemometer, "AWS" automatic weather station. Allsky & BRDF camera and sun photometer data not used in this study. Photo by Dr. Gerit Birnbaum (AWI).

relative humidity with respect to ice because temperatures are far below zero. The Sonic was run in permanent heating mode to avoid icing of the transducers.

Since there are no manned or automatic weather stations throughout vast areas of the Antarctic interior, model predictions and reanalyses are often far off reality. Launching four radiosondes a day enables the investigation of errors in diurnal variations at Kohnen Station for the first time (not in this study). Last radiosondes at this place have been released during the 2005/06 summer season but not as often (Birnbaum, 2013).

Consequently, this study requires data quality investigations and the inclusion of a multitude of data sets. Data from the AWS, the Sonic and observations will be employed to describe the meteorological conditions during the measurement period. The Sonic serves for turbulence measurements and thus is the key instrument in this study. Together with the radiosoundings, the Sonic data will be used to describe the ABL at the site. The surface temperature, necessary for the determination of the vertical temperature difference, will be calculated from pyrgeometer data.

Instrument - sensor	measured quantities	height	temporal resolution
Automatic weather station (AWS) - Vaisala HMP 155 (contains PT100Ω and a thin layer polymer sensor), unventilated - barometer by Young BPA 61302V - vane anemometer by Young Wind Monitor MA	- temperature and rel. humidity, - pressure, - wind speed and direction (2D)	ca. 2m (T & RH ca. 1.4 m)	1 min (average from 60 measurements taken every second)
Observations	cloud fraction (l/m/h/t), precipitation type and strength	-	1 h
Ultrasonic anemometer-thermometer (<i>Sonic</i>) - USA-1 CHS (Scientific) by Metek GmbH	- wind vector (3D), temperature	1.91m	40Hz, continuous measurements from 10 Dec 2013 to 31 Jan 2014 (53 days)
Radiosoundings - RS92-SGPL sonde by VAISALA - GPS receiver	- vertical profiles of pressure, temperature and rel. humidity, - wind speed and direction (2D)	00 and 12 UTC: ≤35km; 06 and 18 UTC: ≤20km)	4 a day
Pygeometer - 2x PIR (Precision Infrared Radiometer) by Eppley Laboratory Inc. USA	Broadband upward and downward longwave radiation (radiant flux density in W/m ²), sensitive to 5 to about 50μm wavelength, ventilated	2m	1 min
Photos	Kohnen Station and environment, instrumentation, precipitation, etc.	-	-

TABLE 3.1: Summary of data sets relevant for the study (Sources: Belka Brea (2015), , Birnbaum (2013), personal communication with Bernd Loose and Dr. Gerit Birnbaum)

3.2 The Sonic

3.2.1 General comments

The measurement of turbulent wind components requires a technique that allows for a temporally dense measurement in order to gain a satisfactory temporal resolution of the fast

changing wind velocities. The same is true for the measurement of turbulent changes in temperature. Moreover, it must be a robust device and of high accuracy. Sonic anemometers-thermometers are a good choice to fulfil these requirements. The instrument used in the campaign has been checked and calibrated for the use at 3000 metres a.s.l. by the manufacturer in July 2013. It has a heating option which was used throughout the whole measurement period in order to prevent the sensor heads from being covered with ice or snow. A thin film of ice (or of any other material) on the ultrasonic transducers would corrupt the measurements. About every second day on-site, the instrument has been checked for rime additionally.

Only one Sonic has been deployed at Kohnen Station during the campaign. Multiple devices would have been desirable for a larger spatial coverage, especially vertically, but this was not possible due to logistic reasons. However, the available highly resolved data are very rare for the observed region, so there is reason to be indeed satisfied with this one data set.

The Sonic was fixed on a vertical rod which was mounted onto a square metal plate dug in snow. The rod was additionally anchored using three wire ropes. The ropes' ends were each wrapped around wooden blocks that were dug in snow. Visual vibrations of the rod during the campaign could not be observed. Using a spirit level, the device has been aligned as normal to the surface as possible. This has been checked again during dismantling showing no change to the initial alignment. Since winds at Kohnen Station are low compared to winds in other polar environments and the upper snow layer is firm without regular melting to be feared, the site fits very well for the deployment of a Sonic. (Sources: photos, manufacturer's certificate, Metek (2006), personal communication with Dr. G. Birnbaum and Dr. C. Lüpkes)

3.2.2 Measuring principle

The time needed for an ultrasound pulse to pass the space between two sensor heads depends not only on the speed of sound, but also on the wind velocity during that time (e.g. Munger et al., 2012) since the fluid containing the sound wave moves as well. The instrument consists of six sensor heads that work in three pairs, yielding three measurement paths of about 17 cm length each (cf. Fig. 3.2). Due to the distinct path alignment, the three-dimensional wind vector can be measured. The upper three sensor heads as well as the lower three are spaced by 120 degrees while the lower ones are shifted against the upper ones so that each connecting measurement path is tilted by 45 degrees from the vertical main rod.

The device comes with a software that calculates turbulent fluxes and turbulence parameters on its own but a fixed averaging interval needs to be set in advance which is a disadvantage for scientific evaluation of the data. In order to enable flexible averaging intervals,

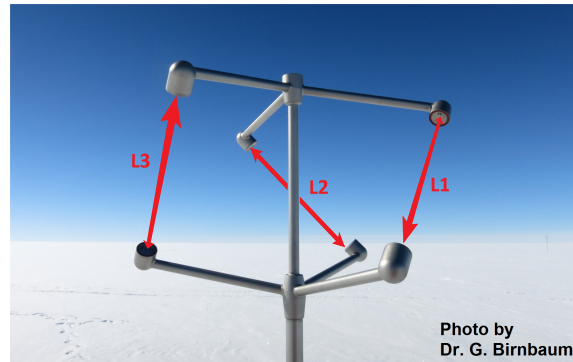


FIGURE 3.2: The six transducers of the sonic anemometer-thermometer make up three measurement paths as indicated. Each transducer alternately serves as emitter and receiver of the sonic signals (Metek, 2006). There is one sonic pulse emitted every 0.025 seconds by every transducer, accounting to a measurement frequency of 40Hz. The sonic travel times as received by the partner sensor head are reported to a remote PC where they are saved into hourly files with the same temporal resolution.

the measurements have been saved in a raw style, i.e. the travel times of the sound pulses are saved straight into hourly files with a temporal resolution of 40 Hz. This in turn requires information from the manufacturer when processing the raw data. You will find the processing procedure, illustrated with the help on an example, in chapter 5.

In the Kohnen campaign, the instrument's settings were chosen in such a way that one sound pulse per sensor was sent out every 0.025 seconds (40 Hz temporal resolution). There was no averaging of transit times from multiple measurements. If blowing snow or precipitation lead to a particle inside the measurement path, a wrong transit time will be measured. Other errors originate from electronic and physical noise. All errors show as spikes in the time series of the raw data of the six sensors and will be corrected.

All scalar dependencies of the sound velocity such as on density or temperature cancel through the pairwise use of the sensors, given that they are constant during one cycle of upward and downward measurement along one path. In contrast to wind as a vector quantity, all scalar quantities act in the same way to the upward and downward sonic travel time between a sensor pair (cf. Metek, 2006). Assuming a constant wind velocity over the course of one upward and downward measurement, the wind speed along one measurement path is calculated using the difference of the inverse sonic travel times $t_{i,up}$ and $t_{i,down}$ along the corresponding path L_i (see e.g. Munger et al. (2012) p. 35 or in Kaimal and Finnigan (1994)). The index i is the number of the path (1 to 3).

$$v_i = \frac{L_i}{2} \left(\frac{1}{t_{i,up}} - \frac{1}{t_{i,down}} \right) \quad (3.1)$$

From the travel times, a so-called sonic temperature T_S can be derived as well. The dependence of speed of sound c on air density ρ is known to be

$$c = \sqrt{\frac{c_p}{c_v} \frac{p}{\rho}} \quad (3.2)$$

where p is air pressure and c_p and c_v specific heat at constant pressure or volume respectively (Erbrecht et al., 1999, p. 79). The ratio c_p/c_v equals $1 + 2/f$ where f displays the degrees of freedom of the gas (5 for air due to N_2 and O_2 abundance) as proven in kinetic gas theory (e.g. Kraus, 2004, p. 53). Thus, $c_p/c_v = 1.40$ for dry air.

The speed of sound c in calm air, i.e. independent of wind velocity but dependent on temperature (via density and pressure), calculates as

$$c = \frac{L_i}{2} \left(\frac{1}{t_{i,up}} + \frac{1}{t_{i,down}} \right) \quad (3.3)$$

(see e.g. Munger et al. (2012) p. 35 or Kaimal and Finnigan (1994) as well). This is equivalent to averaging the upward and downward travel speeds along one path and thus takes away the opposing effects of the corresponding wind component on the travel time of the sonic signal. The full wind vector is eliminated by taking the average of all signal speeds, yielding

$$c = \frac{1}{6} \left[\frac{L_A}{t_{Au}} + \frac{L_A}{t_{Ad}} + \frac{L_B}{t_{Bu}} + \frac{L_B}{t_{Bd}} + \frac{L_C}{t_{Cu}} + \frac{L_C}{t_{Cd}} \right] \quad (3.4)$$

where L is the length of the measurement paths A, B and C, "u" denotes up for the time of the upward sound pulse to arrive at the partner sensor head, "d" for downward. The derivations of equ. 3.1 and 3.3 are shown in appendix A. When the assumption of an ideal gas is applied to equation 3.2, the sonic temperature T_S can be calculated using the measured speed of sound from equ. 3.4.

$$T_S = \frac{1}{c_p/c_v R_d} \cdot c^2 = \frac{5}{2009} c^2 \quad (3.5)$$

where R_d is the specific gas constant of dry air ($287 \text{ J kg}^{-1} \text{ K}^{-1}$) and c_p/c_v refers to dry air as well. However, the speed of sound c is measured in moist air. Therefore, T_S is not equal to the absolute air temperature but influenced by humidity. The relationship to the absolute temperature is

$$T_S = T \left(1 + 0.32 \frac{e}{p} \right) \quad (3.6)$$

where e is the vapour pressure (e.g. Rebmann et al. (2012, p. 66)). Therefore, it is very similar to the virtual temperature T_v which is defined as

$$T_v = T (1 + 0.61 q) = T \left(1 + 0.38 \frac{e}{p} \right) \quad (3.7)$$

where q is the specific humidity (e.g. Kraus (2004, p. 74 & 77) or Rebmann et al. (2012, p. 66)). The differences between T_S and T decrease with decreasing vapour pressure. For dry air, theory tells their are identical. The data processing unit usually available with a Sonic cannot correct for this humidity impact since humidity is not measured by the instrument. Therefore, T_S is generally not trusted as a measure of T . On the other hand, heat fluxes computed by a Sonic can be trusted because they are based on temperature fluctuations (temporally highly resolved deviations from the error-prone mean value). The absolute values of differences between T_S and T fluctuations are much smaller than for the mean values, even negligible. For the important use of the instrument the assumption of dry air is thus justified.

Using typical values from the Kohlen campaign we receive $T_S = T(1 + 1.7 \cdot 10^{-4})$ as the typical equation for the Sonic temperature deviation. Applying Reynolds decomposition to see how much of a deviation we must expect for the mean T_S and its fluctuating part T'_S , we get

$$T_S = \overline{T_S} + T'_S = 1.0002\overline{T} + 1.0002T' \quad (3.8)$$

Inserting the typical temperature -30°C (243.15K) for \overline{T} and the observed maximum fluctuations of T_S as T' (1 Kelvin), we get

$$\overline{T_S} \simeq \overline{T} + 0.05K \quad (3.9)$$

$$T'_S \simeq T' + 0.0002K \quad (3.10)$$

Therefore, $\overline{T_S}$ would differ from the absolute temperature by only 0.02%. The same percentage results for the error of T'_S in comparison to T' . As a result, due to the very low vapour content in the area of measurement, fluctuations of Sonic temperature, absolute temperature and virtual temperature will treated to be equal in this study: $T'_S = T' = T'_v$. The offset for the fluctuation in absolute numbers is much smaller than the one for the mean temperature. Moreover, the heat flux is calculated by the covariance of T' with the fluctuations of the vertical wind component w' over a specific time interval so that small deviations loose their impact even more. Fluxes are calculated using the eddy covariance method which will be described further in chapter 5. As a result, due to the very low vapour content in the area of measurement, fluctuations of Sonic temperature, absolute temperature and virtual temperature will treated to be equal in this study: $T'_S = T' = T'_v$.

CHAPTER 4

Theoretical background

4.1 Surface layer theory

Except for the radiosonde data, all measurements are conducted in about two meters above the ground or (in case of radiation measurements) directly at the ground, i.e. the data are taken within the surface layer. It is also called Prandtl layer or constant-flux layer. To a first approximation, fluxes in the surface layer are independent of height and can therefore be set equal to the (desired) fluxes at the level of roughness length z_0 (close to the surface, will be defined later) (e.g. Holton, 2004, Stull, 1988). The height up until this approximation is valid (typically some decameters) depends on thermal stability of the lowermost atmosphere (e.g. Stull, 1988). Since turbulence is the dominating transport mechanism, fluxes of momentum, sensible and latent heat to/from the underlying surface can be quantified by the vertical turbulent fluxes of these quantities (e.g. Foken et al., 2012, ch. 1).

The vertical turbulent momentum flux M is defined as

$$M = -\rho u_*^2 \quad (4.1)$$

with ρ as (mean) air density and u_* as friction velocity (e.g. Garratt, 1992, p. 10). It is negative since it is directed downwards. u_* is the most important velocity scale in the surface layer

$$u_*^2 = \left| \frac{\tau_0}{\rho} \right| = \sqrt{\overline{u'w'_0}^2 + \overline{v'w'_0}^2} \quad (4.2)$$

where u' and v' are the fluctuating horizontal wind components as transported by the fluctuation of the vertical wind component w' . τ_0 is the turbulent Reynolds stress vector at $z = z_0$, comprising the positively defined components $-\rho \overline{u'w'_0}$ and $-\rho \overline{v'w'_0}$ (e.g. Stull (1988) p. 67; Garratt (1992) p. 41). The vertical turbulent flux of sensible heat H is represented by

$$H = \rho c_p \overline{\theta'w'_0} = -\rho c_p u_* \theta_* \quad (4.3)$$

with c_p as specific heat capacity of dry air at constant pressure ($=1004.67 \text{ J kg}^{-1} \text{ K}^{-1}$) and θ' as the fluctuation of potential temperature (e.g. Garratt (1992) p. 10 or Stull (1988) p. 48ff.). The characteristic temperature θ_* is the temperature scale in the surface layer and is defined as

$$\theta_* = -\frac{\overline{\theta'w'_0}}{u_{*0}} \quad (4.4)$$

(e.g. Garratt, 1992, p. 10). The sensible heat flux must be discriminated from the buoyancy flux which is

$$H_v = \rho c_p \overline{\theta'_v w'_0} = -\rho c_p u_* \theta_{v*} \quad (4.5)$$

and uses fluctuations of virtual potential temperature θ_v (e.g. Stull (1988) p. 146f. or Garratt (1992) p. 10). H_v can be converted into H if the specific humidity (both the mean and fluctuating part) is known. Humidity has not been measured with the necessary temporal resolution in this campaign to enable this conversion and it was shown in the previous chapter that we can assume dry air for this study. Thus, the sensible heat flux can directly be calculated by the use of the measured θ'_S .

The surface roughness is represented by the aerodynamic roughness length z_0 which greatly varies with the physical characteristics of the surface (e.g. Holton, 2004). By definition, the wind speed vanishes at $z = z_0$. It is a surface characteristic and thus must not change with wind speed or stability unless the macroscopic surface structure itself is altered by some process (e.g. Stull, 1988). Typical values measured at various Antarctic locations as summarized by King and Turner (1997) are of the order of 10^{-4} metres or even smaller. However, local z_0 may be influenced by wind speed as indicated by Chamberlain (1983) because faster moving or raising snow particles may increase roughness.

With increasing thermal stability, turbulence is increasingly suppressed due to negative (downward) buoyancy forces that act as a restoring force to deflected air parcels. Eddy sizes can therefore become very small. The ABL will be increasingly shallow and so will be the surface layer (e.g. Stull, 1988). Such conditions have frequently been observed in polar regions, especially in the Antarctic. In unstable conditions, air parcels experience positive (upward) buoyancy. Large eddies can form and mixing is supported while boundary layer heights increase (e.g. Stull, 1988). Even without the development of large eddies,

turbulence is created by the positive buoyancy and thus, heat from lower layers is transported upwards. Bouyancy induced turbulence, however, can be reduced by a large shear (large wind speeds) which favours a downward transport of heat.

Above the surface layer is the Ekman layer that will not be considered in this study. Molecular viscosity is generally neglected throughout the ABL since mixing by turbulence dominates by several orders of magnitude (e.g. Stull, 1988). It is only important within the viscous sublayer which occupies the lowermost millimetres above the surface (or some centimetres over rougher surface) and which does not belong to the constant-flux layer (e.g. Stull, 1988).

When applying Reynolds decomposition and averaging to the system of governing equations, products of perturbations, so-called covariance terms, appear in three of the averaged equations, e.g. vertical turbulent momentum flux in the Navier-Stokes equation and vertical turbulent flux of sensible heat in the prognostic equation for temperature (e.g. Holton, 2004, Garratt, 1992, Stull, 1988, Handorf, 1996). Parametrizations for these terms must be found in order to close the equations (e.g. Garratt, 1992, Kraus, 2008). The traditional approach to this is a local closure scheme applying flux-gradient relations alias K-theory. It assumes that turbulent fluxes are proportional to the local gradient of the mean quantities because turbulence acts against these gradients (e.g. Holton, 2004, Garratt, 1992) so that

$$\overline{u'w'} = \overline{u'w'}_0 = -K_m \frac{\partial \bar{u}(z)}{\partial z} \quad \text{and} \quad \overline{\theta'w'} = \overline{\theta'w'}_0 = -K_h \frac{\partial \bar{\theta}(z)}{\partial z}. \quad (4.6)$$

with K_m as eddy viscosity (eddy diffusivity of momentum) of unit m^2/s ; $\frac{\partial \bar{u}}{\partial z}$ the local vertical gradient of the mean horizontal wind component \bar{u} (the x -axis is aligned with the mean horizontal wind), K_h as eddy diffusivity of heat and $\frac{\partial \bar{\theta}}{\partial z}$ the local vertical gradient of mean potential temperature θ . The eddy diffusivities depend on the flow, on the distance to the surface and on thermal stability of the atmosphere and are therefore not trivial to find.

4.2 Monin-Obukhov similarity theory

For the surface layer, the Monin-Obukhov similarity theory (*MOST*) as developed by Monin and Obukhov in 1954 offers a well-established closure scheme which is consistent with K-theory but does not make use of it for the determination of fluxes. MOST suggests the existence of universal functions ϕ that connect dimensionless gradients for mean wind and temperature to the dimensionless height z/L where L is the Obukhov length (e.g.

Garratt (1992) p. 49 or Stull (1988) p. 378 and p. 360ff.).

$$\frac{\kappa z}{u_*} \frac{\partial \bar{u}(z)}{\partial z} = \varphi_M \left(\frac{z}{L} \right) \quad \text{and} \quad \frac{\kappa z}{\theta_{v*}} \frac{\partial \bar{\theta}_v(z)}{\partial z} = \varphi_H \left(\frac{z}{L} \right) \quad (4.7)$$

ϕ_M and ϕ_H are the universal functions (or non-dimensional local stability functions), where M denotes momentum and H heat. κ is the von Kármán constant which is a universal constant independent of flow or surface characteristics and has been determined by many researchers throughout the last decades (e.g. Högström, 1988). Today, 0.40 is the widely accepted value for κ . The Obukhov length (characteristic height in the surface layer) L is given by

$$L = - \frac{u_*^3}{\kappa \frac{g}{\theta_v} \overline{\theta'_v w'_0}} \quad (4.8)$$

with g as gravitational acceleration (e.g. Garratt (1992) p. 10 or Stull (1988) p. 181). L is a measure of stability because it depends on the kinematic turbulent buoyancy flux $\overline{\theta'_v w'_0}$ with opposite sign. This means, $L > 0$ for stable stratification, $L \rightarrow \pm\infty$ for neutral stratification ($\overline{\theta'_v w'_0} \rightarrow 0$) and $L < 0$ for unstable stratification.

For neutral thermal stratification, both stability functions equal one by definition, creating a purely logarithmic wind profile in the surface layer that is gained by integration of the left-hand side equation 4.7 (e.g. Grachev et al. (2007), Garratt (1992) p. 53f., Stull (1988) p. 377f.).

$$\bar{u}(z) = \frac{u_*}{\kappa} \left[\ln \frac{z}{z_0} - \psi_M \left(\frac{z}{L} \right) + \psi_M \left(\frac{z_0}{L} \right) \right] \quad (4.9)$$

The wind velocity is constrained to vanish at the height of the roughness length z_0 due to frictional drag. Above z_0 , \bar{u} increases with height z . The term $\Psi_M \left(\frac{z_0}{L} \right)$ is usually neglected by scale analysis against $\psi_M \left(\frac{z}{L} \right)$. For neutral stratification, the integral stability function $\Psi_M \left(\frac{z}{L} \right)$ is zero. Under stable conditions, $\Psi_M \left(\frac{z}{L} \right) < 0$ which typically leads to smaller wind speeds in the lowermost 10 metres compared to the logarithmic profile. The opposite is true for unstable stratification with $\Psi_M \left(\frac{z}{L} \right) > 0$ (e.g. Kraus (2008) p. 81, Garratt (1992) p. 53). Integration of the right-hand side equation 4.7 yields an equation for the temperature profile (e.g. Grachev et al. (2007), Garratt (1992) p. 54).

$$\bar{\theta}_v(z) = \bar{\theta}_0 + \frac{\theta_{v*}}{\kappa} \left[\ln \frac{z}{z_{0t}} - \psi_H \left(\frac{z}{L} \right) + \psi_H \left(\frac{z_{0t}}{L} \right) \right] \quad (4.10)$$

Here, θ_0 is the surface potential temperature and z_{0t} is a surface scaling length for temperature. The air temperature T at $z = z_{0t}$ is assumed to equal the surface temperature T_0 . Usually, T_0 and thus θ_0 are determined by radiation measurements although this radiative surface temperature need not be the same as the actual (unknown) surface temperature

(Garratt, 1992, p. 54).

We now have a system of three equations (4.8, 4.9 and 4.10) available which can be solved iteratively for u_* , θ_{v*} and L . That means, if Ψ_M and Ψ_H are known together with the mean wind and temperature profiles $\bar{u}(z)$ and $\bar{\theta}_v(z)$ (from measurements or models), the vertical turbulent momentum and sensible heat fluxes can be calculated. By this method, the perturbation terms in the Navier-Stokes equation and prognostic temperature equation in models are successfully expressed by mean quantities.

MOST does not predict the exact forms of ϕ_M and ϕ_H . They must be determined experimentally which has been targeted by numerous studies in the past under various surface and stability regimes, making these *flux-profile relationships* available for the use in models (for some functions see Appendix B). The obtained functions were often similar, but not identical to each other. Especially under stable stratification, studies have shown much less agreement than under unstable stratification (cf. Foken, 2006, esp. Fig. 3). That is why even under ideal conditions, accuracy of (applied) MOST is estimated to about 10 to 20% (Foken, 2006) but uncertainties grow with increasing stability and can reach up to 300% in strongly stable conditions (personal communication with Dr. Lüpkes). Well known and established are the flux-profile relationships in the form of Dyer and Businger (Dyer, 1974 and Businger et al., 1971), with parameters according to Dyer and Hicks (1970). For the stable regime, the functions by Holtslag and de Bruin (1988) are often used and current research brought up new ones, e.g. by Grachev et al. (2007). The latter derived flux-profile relationships from 11 continuous months of turbulence measurements collected during the SHEBA campaign which was performed over a large fetch of uniform and flat Arctic pack ice.

The requirements of MOST in the above form demand vertical turbulent fluxes to be constant with height (which is approximately fulfilled in the surface layer) and horizontally homogeneous surfaces of not too large roughness lengths (Foken, 2006). A flat, homogeneous surface and steady state/stationary conditions are the requirements for fluxes to be constant with height and to justify the neglect of pressure gradient forces, molecular/viscous transport, gravity and Coriolis forces (Foken et al., 2012, p. 8) which altogether enable surface-atmosphere fluxes to be represented by vertical turbulent fluxes. Quasi-steady state conditions are assumed since diurnal variations in atmospheric stability inhibit true steady-state conditions (Foken et al., 2012, p. 8). Winds should not be too small since this is associated with very stable stratification and in this case, communication between surface and turbulence in the air is impaired, causing z to be no appropriate scaling variable anymore (Grachev et al., 2007, Stull, 1988). Typical magnitudes of MOST scales are ± 200 m for L , 10^{-6} m to 1 m for roughness length z_0 and 0.05 to 0.3 m/s for u_* (Stull,

1988).

Bulk Richardson number

Instead of using z/L as a stability parameter for the ϕ or Ψ functions, they can be expressed alternatively via the bulk Richardson number as a measure of stability. This yields a more independent estimate of the functions since they are gained via the employment of u_* and depicting them against z/L can lead to self-correlation effects because L contains u_* as well (see e.g. Grachev et al. (2007) sec. 4 for references). The bulk Richardson number Ri_B as an approximation of the Gradient Richardson number Ri_G is calculated as the ratio of the production of turbulent kinetic energy by buoyancy and the vertical wind shear.

$$Ri_B = \frac{g \Delta\bar{\theta}_v \Delta z}{\theta_v [(\Delta\bar{u})^2 + (\Delta\bar{v})^2]} \quad (4.11)$$

where $\Delta\bar{\theta}_v$ is the virtual potential temperature difference across a layer of thickness Δz ; $\Delta\bar{u}$ and $\Delta\bar{v}$ are the changes in horizontal wind components across the same layer (taken from http://glossary.ametsoc.org/wiki/Bulk_richardson_number, March 2016 and Stull (1988, p. 177)). With $\Delta z = z - z_0 = z$ using the measurement height z while $z_0 \cong 0$, Ri_B becomes

$$Ri_B = \frac{g |\bar{\theta}_v - \bar{\theta}_0| z}{\theta_v (\bar{u}^2 + \bar{v}^2)} \quad (4.12)$$

where $\bar{\theta}_v$ is the virtual potential temperature at measurement height z , $\bar{\theta}_0$ the surface potential temperature, \bar{u} and \bar{v} are the horizontal wind components at measurement height z (Garratt, 1992, p. 54). Low values of Ri_B indicate strong shear relative to buoyancy, large values suggest that in the production of turbulent kinetic energy, buoyancy dominates over shear. Gradient Richardson numbers smaller than the critical value 0.25 represent dynamically unstable conditions which are likely to become or remain turbulent (Stull, 1988 and the link above). A critical value is not well defined for the bulk Richardson number but since Ri_B approaches Ri_G with thinner layers (Δz is 2 metres in this study), the critical value is expected to be close to 0.25.

The gradient Richardson number Ri (and thus Ri_B) is uniquely linked to $\zeta = z/L$ in MOST via

$$Ri = \zeta \cdot \frac{\phi_H}{\phi_M^2} \quad (4.13)$$

(Garratt, 1992, p. 49).

4.3 Bulk transfer relations

The so-called bulk aerodynamic formula is another common closure scheme to account for turbulent fluxes in energy budget studies and atmospheric models (cf. Andreas et al. (2010) or Stull (1988) p. 262). It suggests that friction velocity as a measure of surface stress is proportional to the mean horizontal wind at level z (usually the lowest grid level at 10 metres).

$$u_{*0}^2 = C_D \bar{u}^2(z) \quad (4.14)$$

The factor C_D is the drag coefficient which depends on z and decreases with increasing stability (e.g. Etling, 2008, p. 310f.). Similarly, there is a bulk transfer coefficient C_H for heat. The bulk formulation for sensible heat flux (e.g. Garratt, 1992, p. 55) is written as

$$\frac{H_0}{\rho c_p} = (\overline{\theta' w'})_0 = -(u_* \theta_*)_0 = C_H \bar{u}(z) \cdot (\bar{\theta}_0 - \bar{\theta}(z)) . \quad (4.15)$$

The bulk transfer coefficients C_D and C_H can be presented as functions of $\zeta = z/L$ or Ri_B in accordance to MOST as will be demonstrated in the following for the example of C_D . Inserting equ. 4.9 into equ. 4.14 yields

$$C_D = \frac{\kappa^2}{[\ln(z/z_0) - \psi_M(\zeta)]^2} . \quad (4.16)$$

Therefore, the neutral drag coefficient directly relates to the aerodynamic roughness length z_0 :

$$C_{Dn} = \frac{\kappa^2}{[\ln(z/z_0)]^2} \quad (4.17)$$

Similarly, the neutral C_H can be written as

$$C_{Hn} = \frac{\kappa^2}{\ln(z/z_0) \cdot \ln(z/z_{0t})} \quad (4.18)$$

A non-dimensional function f_m can be defined as

$$f_m = \frac{C_D}{C_{Dn}} . \quad (4.19)$$

With the expressions from equ. 4.16 and 4.17, f_m becomes

$$f_m = \left[1 - \frac{\psi_M(\zeta)}{\ln(z/z_0)} \right]^{-2} \quad (4.20)$$

(see e.g. Garratt (1992, p. 54) and Gryanik and Lüpkes (2017, submitted)). It is therefore dependent on the roughness length z_0 and stability ζ . With a given stability function ψ_M

and known z_0 , f_m can be used for momentum flux parametrization in the surface layer by combining equ. 4.14 and 4.19:

$$u_{*0}^2 = C_{Dn} \cdot f_m(z/z_0, \zeta) \cdot \bar{u}^2(z) \quad (4.21)$$

(cf. Garratt, 1992, p. 243). By this method, if z_0 and ψ_M from MOST are known, surface momentum flux M can be parametrized iteratively. A direct computation is not possible because ζ incorporates the kinematic turbulent fluxes u_{*0} and $(\overline{\theta'w'})_0$ as well.

Louis (1979) derived f_m in dependence of Ri_B for stable stratification to be

$$f_m(z/z_0, Ri_B) = [1 + 4.7Ri_B]^{-2} \quad (4.22)$$

based on the stability functions by Businger et al. (1971). The equation above is only valid for momentum flux parametrization under stable stratification. The availability of parametrizations in dependence on Ri_B instead of ζ is of great advantage for modelling (the one above is just one example) because no iterative solution is necessary. Only z_0 must be assumed (for unstable stratification). Since Ri_B is a function of mean quantities between two levels, turbulent fluxes can directly be calculated from mean quantities and z_0 at comparably low computational expense.

CHAPTER 5

Data preparation

The previous chapters revealed a clear need for the evaluation of multiple data sets in order to compute the results of this study. The current chapter addresses the preprocessing of all necessary data sets (longwave radiation, AWS temperature and Sonic data) together with data quality considerations and corrections where necessary. This includes a step-by-step description of the rather complex way the turbulence data are gained from Sonic raw data based on the eddy covariance (or eddy correlation) method.

5.1 Derivation of surface temperature from longwave radiation

The surface temperature T_0 is determined according to the Stefan-Boltzmann law from minutewise radiation measurements:

$$-LW \uparrow = \varepsilon\sigma T_0^4 + (1 - \varepsilon)LW \downarrow \quad (5.1)$$

where $\sigma = 5.67 \cdot 10^{-8} \text{ Wm}^{-2}\text{K}^{-4}$ is the Stefan-Boltzmann constant (for equation see e.g. Oke (1987) p. 22). $LW \uparrow$ (in W/m^2 , defined negative) is the measured upward broadband longwave radiant flux. It is equal to the sum of longwave radiant flux emitted by the surface into the upper hemisphere ($\varepsilon\sigma T_0^4$ with unknown surface longwave emissivity ε) and the portion of downwelling broadband longwave radiant flux $LW \downarrow$ that is reflected by the snow surface into the upper hemisphere (reflectance $r = 1 - \varepsilon$).

Longwave emissivity ε of the snow surface is close to 1 like with most natural surfaces (cf. Oke (1987) p. 361) but the exact value is not known. The quantity differs for example with snow grain size and wavelength window (see e.g. Hori et al. (2006)) but the minimum value found in literature is 0.80 (e.g. Oke (1987) p. 12). In this study, we assume $\varepsilon = 0.97$ because it proved to be a reasonable value for local surface conditions (further explanations in section 6.2.2). An advantage of using $\varepsilon = 1$ (a popular value for snow surfaces in meteorological studies) is that the reflection term vanishes, making T_0 purely dependent on $LW \uparrow$ measurements, requiring only one sensor instead of two. This can decrease the influence of measurement errors onto T_0 .

It is easy to find from equ. 5.1 that for overcast conditions $\varepsilon = 1$ is a valid choice (assume $-LW \uparrow \approx LW \downarrow$). The largest impact from a variable ε is under clear sky conditions because then, differences between $-LW \uparrow$ and $LW \downarrow$ are largest. If we identify clear sky conditions as $LW \downarrow < 150 W/m^2$, clear sky median $|LW \uparrow|$ over the campaign period is $207 W/m^2$ and median $LW \downarrow$ is $134 W/m^2$. Inserting these values into equ. 5.1 we see that every -0.01 step in ε , starting from 1.0, typically increases T_0 by 0.22 K. If we used $\varepsilon = 1.0$ instead of 0.97, the typical difference in calculated surface temperature would be -0.67 K. The same value results if we discriminate December and January conditions.

From T_0 , the potential surface temperature θ_0 is calculated using pressure as measured by the AWS under the assumption of dry air. θ_0 is only used in combination with θ_{air} to receive the vertical temperature difference which enters Ri_B , C_H and ψ_H . The choice of ε therefore impacts these three quantities through the vertical temperature difference. Since T_{air} in this study is measured close to the surface (at 1.9 m height), a typical error of almost 1 Kelvin for θ_0 (depending on the size of ε) can have a significant impact.

The T_0 time series is corrected for spikes by the following method: The time series is detrended in blocks of 12 hours starting at midnight in order to erase the diurnal cycle. In every 12 hour block, T_0 values are eliminated which are outside of ± 3 times the standard deviation of the corresponding block. This method leads to an exclusion of 1% of minutewise T_0 data.

5.2 Quality control of AWS air temperature

In general, commonly measured temperatures (via a Platinum RTD or a thermocouple) are to be preferred over Sonic mean temperature readings because of the moisture influence on Sonic temperature and its high sensitivity to calibration (see e.g. Huwald et al., 2009).

The AWS temperature records are investigated in some detail in order to gain a reliable independent data set for comparison to Sonic temperature data.

In order to compare both temperature data sets, a Sonic temperature time series with one minute resolution is created and depicted together with the AWS temperature time series (Fig. 5.1). The Sonic temperature confirms that in some nights the strong periodicity of the daily temperature curve is interrupted by lacking the steep nighttime temperature decrease. These unusually warm nights therefore seem to be a real phenomenon. From theory we expect both temperatures to agree well because vapour pressure is very low at the site (see equ. 3.6).

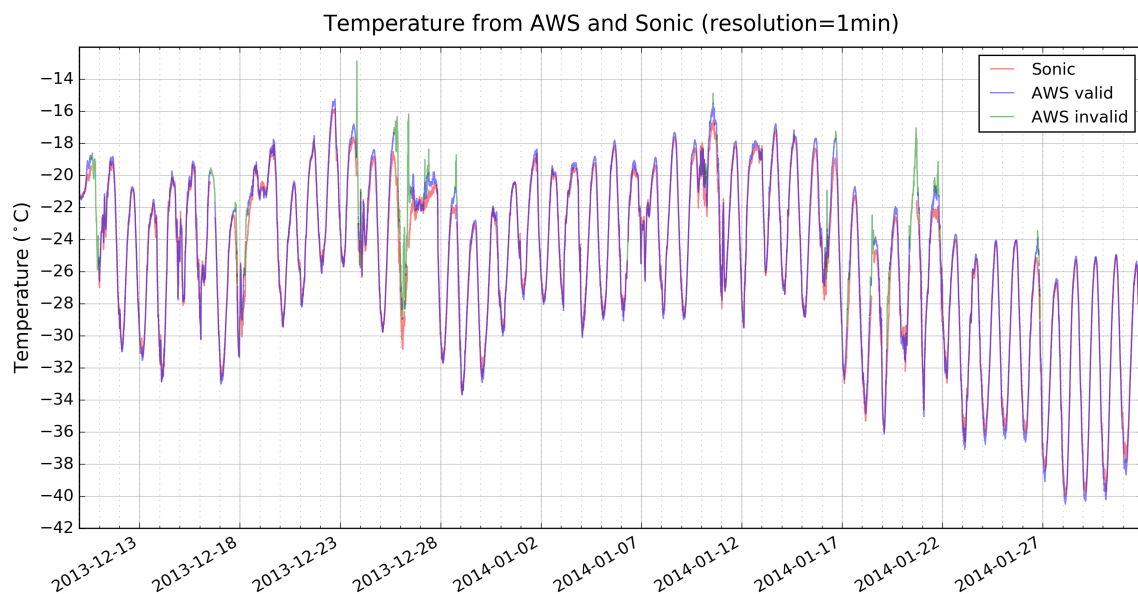


FIGURE 5.1: Time series of temperature as measured by the Sonic (approx. 1.9 m height) in red and AWS temperature measured by a Pt100 (approx. 1.4 m height) in blue, both with 1 min resolution to enable proper comparison. Colours are semi-transparent: overlying lines mix in colour. "AWS invalid" marks the data that will be neglected for further analysis after the data quality treatment explained in this section.

On strikingly many days, the daily maximum temperatures of the AWS are much larger than the Sonic temperatures, often even showing distinct short-time spikes shortly before declining steeply. When plotted together with wind speed, this behaviour can most likely be traced back to ventilation problems since the radiation shielding of the AWS temperature and humidity sensor is not ventilated. When winds are sufficiently small, the air volume inside the shielding heats up due to insolation, leading to a falsely large measured temperature. You find the time series of temperature difference ($T_{AWS} - T_{Sonic}$) together with the AWS wind speed in Figure 5.2 and a close-up of one event in Figure 5.3. The typical temperature difference is 0.5 K while the AWS temperature is mostly larger than the Sonic one during daytime and smaller at night. The scatter plot in Fig. 5.4 shows that

with increasing wind speed, differences between both temperatures decrease. Especially when wind speeds decrease towards 1 m/s, the AWS temperature can exceed the Sonic temperature by several degrees. These errors cannot be attributed to Sonic temperature uncertainties because the spikes would also show there. The Sonic temperature time series does not show such unreasonable spikes. Furthermore, the way it is calculated also works for low-wind conditions.

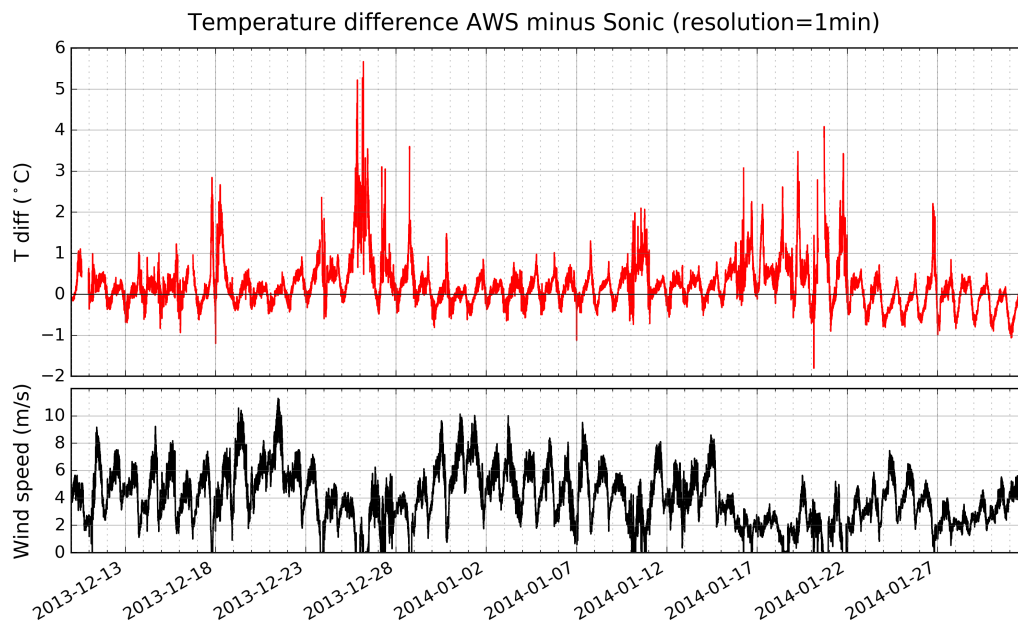


FIGURE 5.2: Time series of temperature differences between AWS and Sonic measurements. The largest differences occur when wind speeds become very small. This indicates ventilation problems of the AWS radiation shielding which houses the temperature sensor Pt100.

Differences at night remain smaller than during the day, probably due a much lower elevation angle of the sun (no sunset until February) and hence less incoming shortwave radiation. Nighttime AWS temperatures show no striking values that must be interpreted as outliers. The typical daytime and nighttime differences can partly be explained by the different measurement heights of the two systems (Pt100 at approx. 1.4m height, Sonic at approx. 1.9m). Night-time temperature inversion and day-time surface warming lead to strong vertical temperature gradients close to the surface of ± 0.2 K/m and more during the measurement period. This causes systematic differences between both temperature records during day and night which are not caused by a measurement error. Ultimately, this can be connected to atmospheric stability. Although usually the AWS air temperature is preferred over the Sonic temperature in atmospheric studies, this difference in height is highly problematic because for our study, we need temperature measurements from the same height as is used for turbulence measurements. Due to the stability dependence of the difference of both temperatures, simple "correction" by a daytime and nighttime offset is therefore not

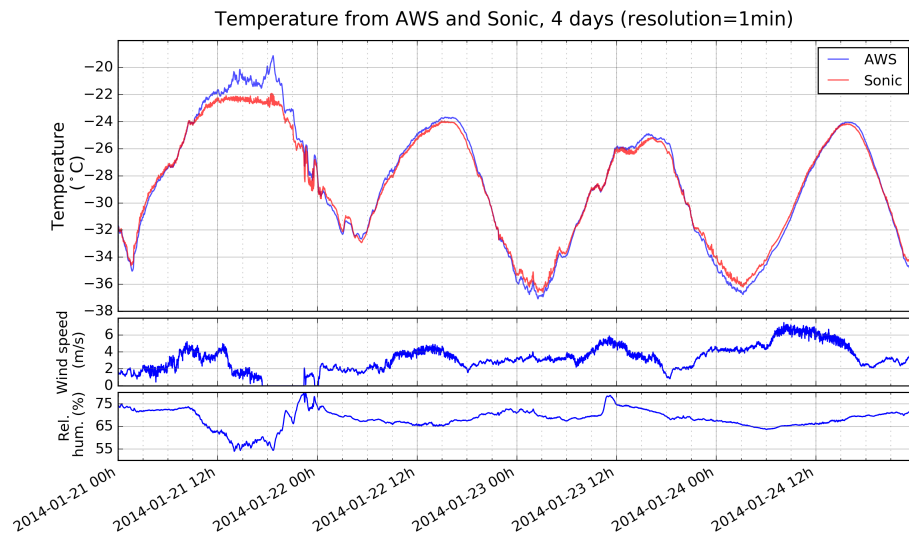


FIGURE 5.3: A close-up of both temperature data sets over a period of 4 days. The first day shows one of those events when differences are comparably large which must be connected to vanishing wind speed. The humidity sensor measures very low relative humidity (with respect to liquid water) during that time. It is housed in the same naturally ventilated shielding as the temperature sensor and would also be affected by the influence of insolation that heats up the little chamber when wind speeds are low. With rising temperatures at constant specific humidity, rel. humidity declines of course. The effect is not visible at night due to strongly reduced insolation at nighttime.

possible.

In conclusion, different measurement heights and the radiation problems in the daytime AWS temperature hence lead us to use the Sonic temperature for the calculation of results in this study. The maximum possible overestimation of Sonic temperature due to its humidity influence according to equ. 3.6 is computed to be 0.2 K for the measurement period. The typical deviation from the physical temperature however, calculated from the mean campaign temperature, vapour pressure and air pressure amounts to only 0.07 K. This systematic error and the comparison to the AWS temperature make it reasonable to assume a general error of 0.5 K for the (15 min mean) Sonic temperature in this study, assuming correct calibration for the present low temperature conditions. Note that the use of Sonic mean temperature as a measure of physical temperature is not recommended in climates of larger specific humidity and caution must be given for measurements above vegetated areas because of the close interaction of vegetation with air moisture. For an independent and correct measurement of mean physical temperature in those regions a common and ventilated system must be employed at the same height as the turbulence sensor.

For any further use of the AWS temperature, questionable daytime temperatures will be

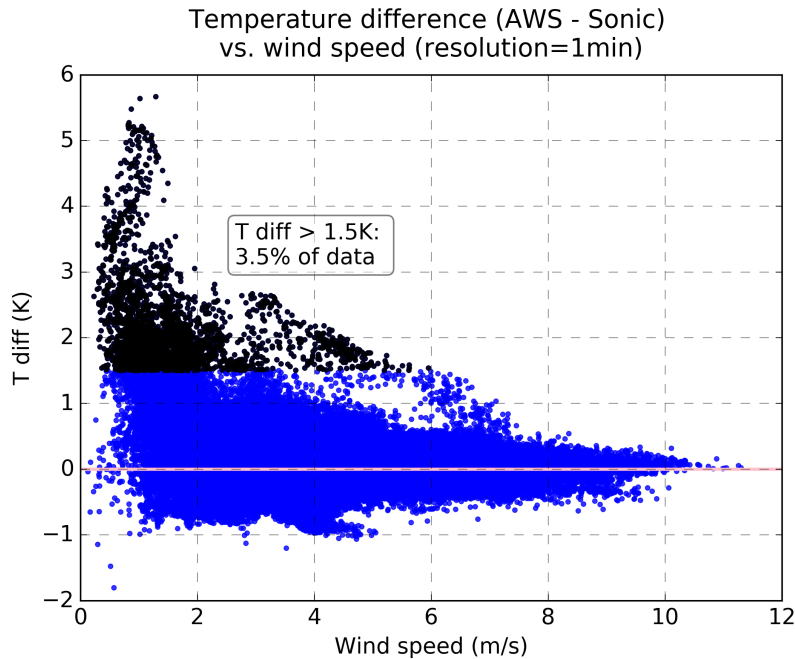


FIGURE 5.4: A scatter plot of temperature differences from both systems against wind speed. With increasing wind speed, the differences fall off. Positive differences have a larger spread than negative differences: the AWS temperature is unlikely to be more than 1 Kelvin below the Sonic temperature while it can be larger than the Sonic temperature by several Kelvin. Generally, the spread becomes larger with decreasing wind speed, especially below 4 m/s. 3.5% of the AWS data overshoot the Sonic temperature by 1.5 Kelvin and will be neglected for further investigations.

eliminated from the time series using the Sonic temperature as an indicator of ventilation problems. All cases when the AWS temperature exceeds the Sonic one by more than 1.5 Kelvin will be neglected. This method leads to a neglect of 3.5% of minutewise AWS temperature data. 33% of these cases correspond to Sonic wind speeds below 1 m/s for which no final results are computed anyway (due to other reasons of Sonic data quality, see description of Sonic data in next section). You find the corrected AWS temperature time series in Fig. 5.1 where the colour green indicates invalid data (which will be left out for further analysis).

Indeed, many studies have already investigated radiation errors on unventilated temperature measurements based on a variety of sensor and shielding combinations in different climates. Insolation and low wind speeds showed to increase measured temperatures in naturally ventilated shieldings during daytime by several Kelvin and records are erroneous even at night. Correction schemes are proposed but in case of snow or ice covered surfaces, reflected shortwave radiation causes even larger deviations that are very difficult to correct for (see e.g. Georges and Kaser, 2002, Arck and Scherer, 2001). Huwald et al. (2009) show that temperature errors grow faster for reflected than for incident solar radiation and

conclude that surface albedo is a key quantity for correction schemes above snow surfaces. Georges and Kaser (2002) found errors of up to 1 K over a snow covered area in Peru, Hock (1994) up to 6 K on a glacier in Sweden on calm clear-sky days with a daily mean temperature error of 1.2 K. In the study of Huwald et al. (2009) nighttime temperature differences over an alpine snow-covered surface are mostly within ± 1 K whereas daytime differences reach up to +10 K. They show a very similar connection between temperature difference and wind speed as depicted in Fig. 5.4, based on temperature records from a Sonic (carefully calibrated and corrected) and Pt100 in an unventilated shielding (their Fig. 3). Artificial ventilation is consequently highly recommended for AWS temperature measurements over snow surfaces.

5.3 From raw Sonic data to turbulent fluxes using the eddy covariance method

In this paragraph, the data processing from raw Sonic data to turbulent fluxes and other quantities will be explained together with helpful graphics. Although this may seem irrelevant for the final results of this work, this data processing is essential for gaining trustworthy results since it starts with raw sonic travel times between the sensor pairs of the Sonic. Compiling a reliable processing script for turbulent fluxes, drag coefficient, Obukhov length, friction velocity and turbulent kinetic energy has also been the most time-consuming part of this thesis, before any roughness lengths or values for stability functions could be computed.

5.3.1 The eddy covariance method

The data processing steps follow the common workflow of the eddy covariance method. Yet, there was no description in the literature available that fit the detailed workflow of the available code from the group because every application of the eddy covariance method is special to its system - that means to the employed instrument, measured quantities, experimental layout and the measurement environment. Moreover, different approaches exist inside the method. The Fluxnet initiative for example puts a lot of effort in unifying them. For these reasons, the order and the content of the processing steps as implemented in the given code remain unchanged but were tested and checked for potential flaws.

The eddy covariance method is the commonly used and approved method for the calculation of a variety of (vertical turbulent) fluxes of different quantities, such as momentum and heat. Its name originates from the use of the covariance between two highly resolved time series (e.g. w and T) in order to gain the turbulent flux in its kinematic form (e.g.

$\overline{w'T'}$). For a quantity $A = \bar{A} + a'$ (where a' describes the fluctuations against the mean \bar{A}), it can be shown that the variance σ_A^2 is equal to the mean squared perturbation $\overline{a'^2}$ of the quantity as e.g. described in Stull (1988, p. 42ff.). The averaged non-linear turbulence product $\overline{a'b'}$ is just the covariance σ_{AB} of quantities A and B . The mixed terms $\overline{a'b'}$ as they appear in the definitions of turbulent fluxes have non-negligible magnitudes if a' and b' are correlated. You find an illustrative example in Fig. 5.5. The data time series must be pre-processed (high-pass filtered) to make this method applicable for a representative flux calculation.

Its most common application is the estimation of CO₂, heat, water (and other trace gas) exchange between plant canopies and the atmosphere, although eddy covariance systems are also used in benthic environments and over any kind of surface type in the ABL (e.g. heat exchange between different types of sea ice and atmosphere). The eddy covariance method relies on temporally dense measurements of the quantities of interest since small-scale fluctuations must be measured in order to measure the turbulent fluxes. The Sonic anemometer-thermometer is only one example of a typical instrument in use. It is usually employed in turbulence studies using several Sonics mounted to masts or tower constructions. Gas analysers are needed apart from it for the calculation of gas exchange but remote sensing methods exist as well.

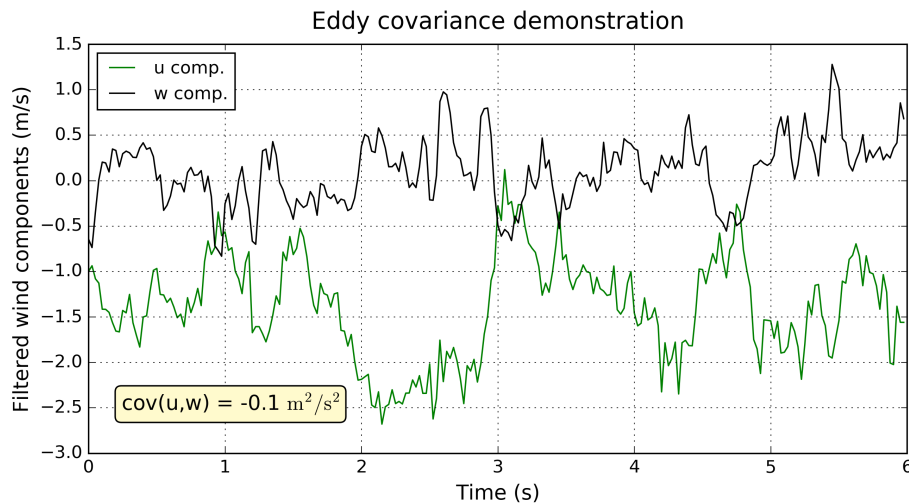


FIGURE 5.5: The high-pass filtered wind components u and w are depicted with a measurement resolution of 40Hz over a time interval of six seconds. Their anticorrelation can be seen by eye on this short interval. However, the common interval for flux calculation, so-called averaging interval, is 30 minutes long in order to capture enough eddy cycles to gain a representative value for the turbulent flux. According to the established eddy covariance method, we see that (for these six seconds of data) $\text{cov}(u,w) = \overline{u'w'} = -0.1 \text{ m}^2/\text{s}^2$.

5.3.2 Data processing of Sonic raw data

A processing script consisting of four parts was available but it needed a change of certain parameters and a check of certain routines because it was written for an older instrument type with different dimensions and other data properties than the new Sonic used in the Kohnen campaign. It was written by Dr. Stephan Mai (no more at AWI) in 1996 and later modified by Dr. Thomas Garbrecht and Dr. Christof Lüpkes. It is written in KYSS which is a scripting language based on C. This language has been developed by Dr. Jörg Hartmann (all named scientists worked/work in the section Polar Meteorology, AWI Bremerhaven) for the evaluation of data gained during the flight campaigns of the group conducted in the ABL. Dr. Hartmann helped with questions about the KYSS syntax although for the processing script of the Sonic data, the only help were handbooks of several Sonic instruments, literature that only covered single processing steps at a time and the manufacturer of the instrument (Metek GmbH, consultant Mr. Kirtzel). Due to copyright reasons, not all functions from Metek GmbH can be presented here in detail. The new script has been rewritten in Python (amounting to about 1000 lines of code) for easier handling and flexibility, also for the ease of future researchers working with data collected by the instrument. The analysis procedure is the same as in the original KYSS code whereas detailed comments facilitate code understanding, all user settings are to be set at the beginning of the script and all processing steps have been checked for correctness or have been changed (where necessary or where output quality could be increased). The outlier elimination scheme has been replaced completely because in contrast to former use of the script, the code runs for several continuous days of data. Before, e.g. in the Polarstern campaign in 1996, only several hours of data were available at once and therefore could be viewed by the researcher while for the Kohnen campaign, this is not possible due to the large amount of data. Thus, the outlier removal scheme must be automatized.

The data is available in the shape of hourly files with 40Hz temporal resolution. After analysis of the individual files using a loop, the results are concatenated to achieve a 53 days data stream. A time array is created on the fly, lacking the following hours:

- missing hours (21 hours in total)
- hourly files that contain too little data (6 hours in total, must be discarded since there is no time stamp saved inside the raw data file)
- hours that exceed the allowed amount of outliers (threshold set to 3% which results in 12 discarded hours)

1. Pre-processing

1.1. Correct length

On average, the hourly files have 26 entries (0.65 seconds) too much data which are cut in order to achieve the correct temporal duration of one hour. They emerge due to the file creation by the connected PC the clock of which is not as exact as the quartz crystal that controls the frequency of the sonic pulses. Therefore, the continuous data stream is interrupted once per hour by about 0.65 seconds which amounts to negligible 0.02% of the hourly data. Due to the high temporal resolution, not all files can be read and processed at once and need to be cut in blocks anyway.

1.2. Calibration

The raw travel times for each of the six sensors are saved in units of 25 nanoseconds. They are calibrated by offsets taken from the manufacturer's certificate created shortly before the campaign. The offsets originate from the conversion of electronic to sonic pulses inside the sensors. An example for calibrated upward and downward sonic travel times along path A is depicted in Fig. 5.6a. These data are taken from 20 to 21 UTC at 13 Dec 2013 when light snowfall occurred.

1.3. Outlier elimination

The outlier detection is based on the advantage that three measurement paths for deducing the speed of sound are available. By averaging the upward and downward travel times for each path, three values for the speed of sound and thus, three sonic (air) temperatures are computed in 40 Hz temporal resolution (see Sonic working principle). One can now compare these temperatures that are expected to be fairly equal (they deviate due to the influence of the wind vector onto the path of the sonic pulse). Values that deviate more than 2 Kelvin from the mean temperature difference between two paths are marked as outliers. This is a very reliable method for detection because it makes use of all available sensors at once. Outliers are replaced by linear interpolation using the closest valid neighbours. If located at the beginning or end of the hourly data stream, they are directly substituted by the closest valid neighbour. Replacements always take place for all six data columns (six sensors). At maximum, 3% of the data within one hour is replaced, otherwise the full hour is marked as invalid. In the example hour, nine outliers (0.006% of data) are found and replaced as depicted in Fig. 5.6b.

2. Computation of wind and temperature data

From the despiked sonic travel times, wind speeds along the three paths are calculated. By geometric considerations, these wind data are transformed to a left-handed coordinate system where the z-axis is along the vertical axis of the instrument. Due to the flow resistance of the instrument itself, the now 3D wind components are increased by a certain percentage. Additionally, the flow distortion created by the instrument geometry is compensated for. The sonic (air) temperature is calculated using the speed of sound "in calm air" (a mean speed of sound from the three individual values). With increasing wind speed, the

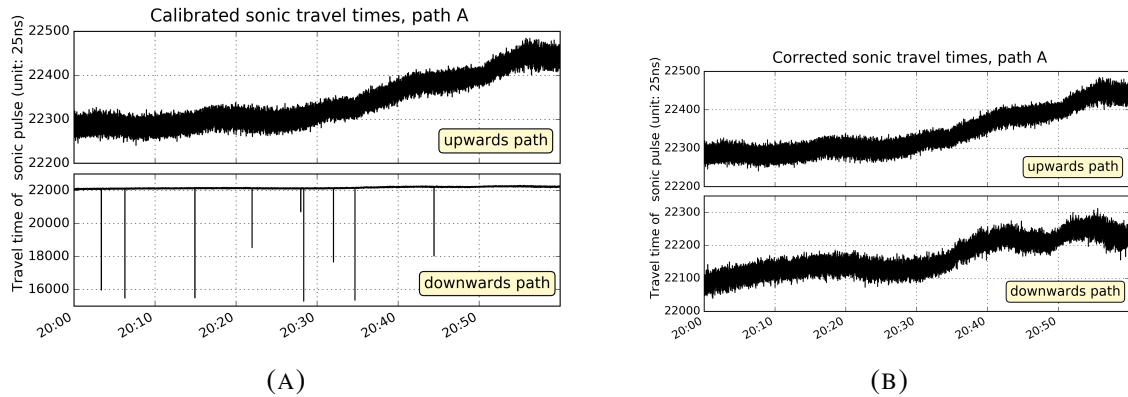


FIGURE 5.6: Sonic travel times along measurement path A (upwards and downwards) in units of 25ns with 40Hz temporal resolution from 13 Dec 2013 20-21 UTC. Due to light snowfall (particle in measurement path) or other electronic or physical error sources, spikes in the downwards path are detected (a) and corrected (b) using an outlier elimination scheme based on a comparison of path-individual sonic temperatures.

sonic temperature value gets an extra increase. This is because the travel path of the sound pulse enlarges with increasing horizontal wind speed and the calculated temperature thus needs to be corrected (so-called cross-wind correction). This effect is irrelevant for wind speed calculation along the paths because there, differences of the travel times are used instead of averages. The results of this processing step for the example hour are shown in Fig. 5.7.

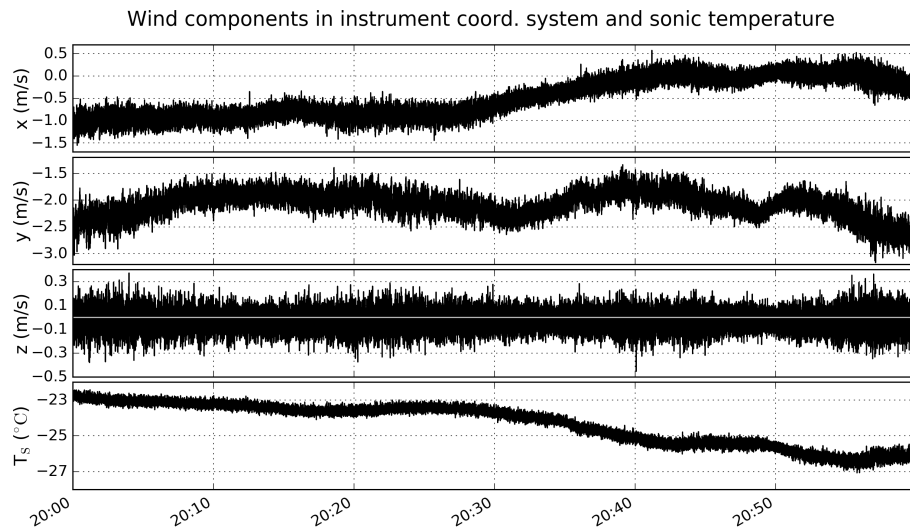
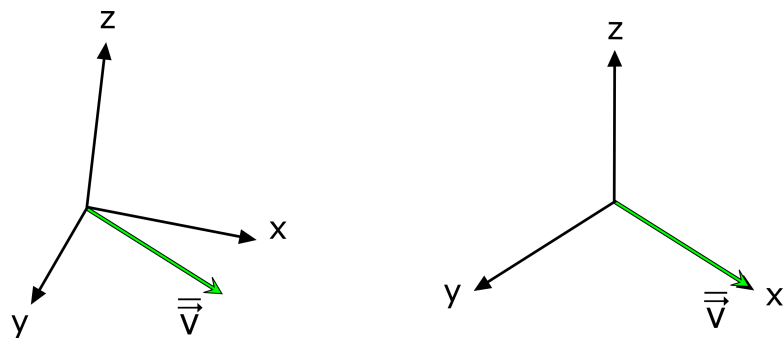


FIGURE 5.7: Highly resolved wind and temperature data gained from the Sonic for one example hour (same as above), left-handed orthogonal system in the instrument's reference frame.

3. Rotation into local streamline coordinates

The coordinate system in the instrument reference frame is rotated so that the new x-axis

is directed into the local mean wind vector. This method is especially of avail if multiple instruments are used to cover a larger fetch but it is very helpful in this study as well because even slight tilts of the instrument's setup can be corrected this way. This is important for flux calculation. The new wind vector becomes (u,v,w) where u is the component into the direction of the new x -axis that points along the local mean wind vector, v is the cross-wind component of the new y -axis (to the right of the mean wind vector since we input a left-handed system) and w is the wind component orthogonal to the x - y -plane, the new z -axis pointing upwards away from the Earth's surface (see sketch 5.8). The mean v and w components become zero while they still contain fluctuations on the smaller temporal scale. In order to avoid over-rotation, an averaging interval of 30 minutes is used to determine the direction of the mean wind vector. Thus, the mean u component value is the 30 minutes mean wind speed.



instrument coord. system \rightarrow coord. system after rotation

FIGURE 5.8

Three rotations are necessary in order to gain local streamline coordinates (see chapter 6.6. in Kaimal and Finnigan (1994)): The first one rotates the system about the y -axis, forcing the mean v component to become zero. The second one is a rotation about the newly gained y -axis to force the mean w component to vanish. In more complex or steep topography with separating flow, one should leave it at these two rotations. In low topography such as the one in the Kohnen Station area, a third rotation is done to fix the direction of the new z -axis in order to gain correct streamline coordinates. The system is rotated about the new x -axis which should nullify $\overline{v'w'}$. In fact, $\overline{v'w'}$ is usually only one order of magnitude smaller than $\overline{w'w'}$. However, it is neglected for the calculation of final results (u_* etc.) because whether or not to include it into the final results causes a negligible change in values. Compared to performing only the first two rotations, the third rotation decreases the $\overline{v'w'}$ value, often even the order of magnitude is decreased by one order. The rotated wind components for the example hour are depicted in Fig. 5.9, a typical daily course of the u and w component as well as sonic temperature in Fig. 5.10.

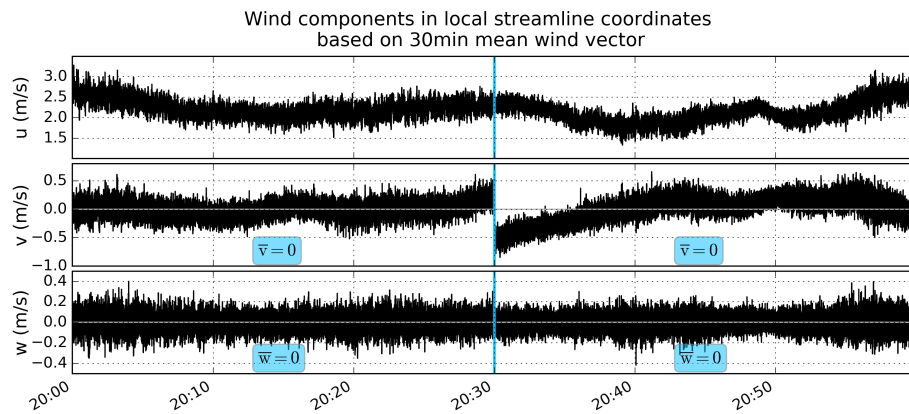


FIGURE 5.9: Wind components in streamline coordinates for one hour (i.e. after rotation).

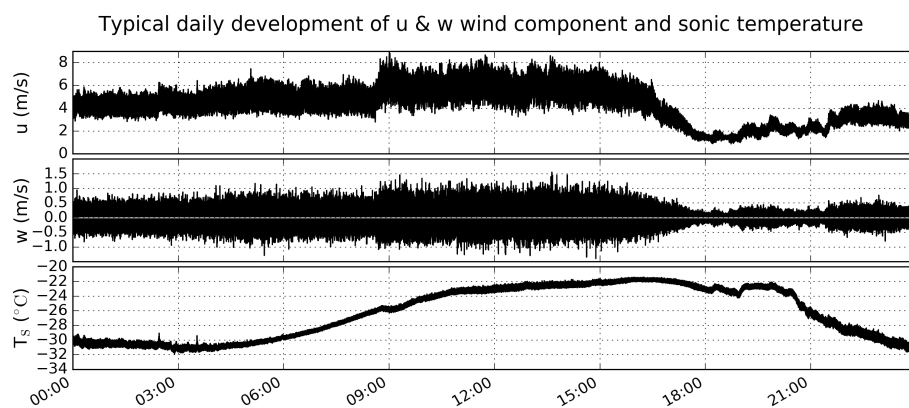


FIGURE 5.10: Wind components in streamline coordinates for 13 Dec 2013 (i.e. after rotation).

4. High-pass filter

Since we aim at receiving representative fluctuations as deviations from the mean, waves of small frequencies are eliminated from the hourly wind components and temperature. Using a Fast Fourier Transform (FFT), waves of equal or smaller frequencies than the set filter frequency are filtered from the data. Due to the continuous frequency spectrum, the value of the filter frequency is somewhat arbitrary. It shall be small enough to filter out all unwanted large-scale phenomena such as gravity waves or changes due to advection. A little study about the impact of threshold frequencies is shown in appendix C. Also, trends are filtered out in order to receive correct fluctuations that are valid to describe turbulence. On the other hand, the filter frequency should not be too small which would cut away frequencies that still belong to the turbulence spectrum. A rectangular filter is used, i.e. in the FFT power spectrum, values are set to zero for frequencies equal and smaller than the filter frequency, before performing the backtransform.

Usually, a non-linear filter is not recommended because it can erase low-frequency contributions (large eddy contributions) to the turbulent fluxes. There will no FFT applied in the

final flux calculation for this study but the possibility of using it shall be mentioned here. Some sort of high-pass filtering automatically occurs by cutting the hourly data stream into intervals and linear detrending will be performed on these data intervals after rotation into streamline coordinates.

This high-pass filter is applied on 30 minute intervals like the rotation before. The resulting wind components and sonic temperatures are distributed around zero (see Fig. 5.11), leaving only the deviations from the mean after correction for large-scale influences. The filtered time series from the two intervals are concatenated again to gain a full hour of data as shown in Fig. 5.11.

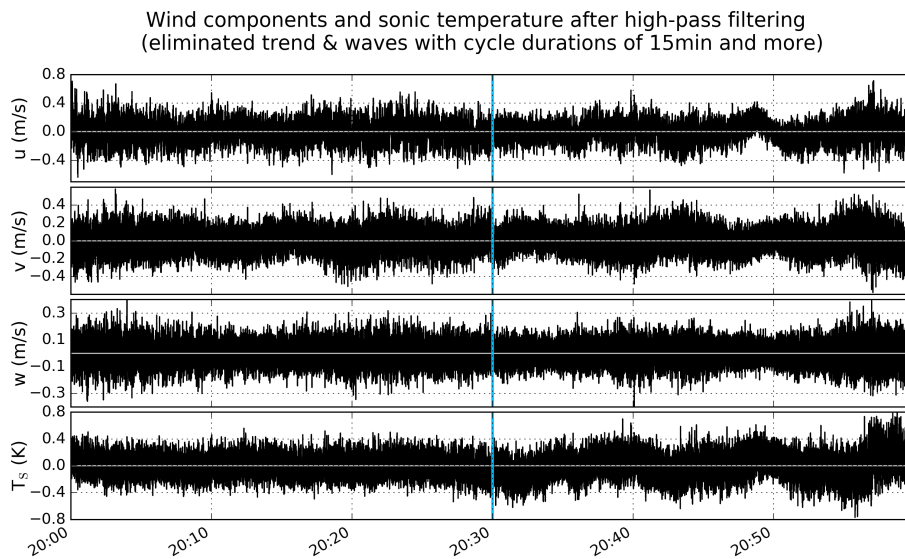


FIGURE 5.11: Filtered wind components in streamline coordinates for one hour.

5. Calculation of results

u is mean V from u, v, w (must be mean wind on interval)

The hour of high-pass filtered data is divided into intervals again which will serve as the averaging intervals for flux calculation. The interval length can be set by the user. A common value used for mid-latitudes studies is 30 minutes as well, so for the environment at hand it should be shorter. The interval length should be chosen to maximize the turbulent fluxes. If too short, not enough fluctuations are included into calculation, the calculated flux would not be representative for the real one. As a rule of thumb, the averaging interval should span the duration of several eddy cycles in order to gain a good statistical representation. This means in general, that under very stable conditions in the SL, smaller averaging times would be needed than for unstable conditions. The averaging interval should not be too long on the other hand in order to decrease the risk of influences from effects on a

larger time scale. An averaging interval of 15min duration showed to be appropriate for the location of Kohlen Station, see subsection 5.3.5.

For flux calculation, variances and covariances of the wind components and (sonic) temperature are employed as described before. Besides the variances of high-pass filtered u , v , w , only the covariances containing the vertical wind component w are calculated since we are only interested in vertical turbulent fluxes, not horizontal ones. This is $\text{cov}(u, w)$, $\text{cov}(v, w)$ and $\text{cov}(T, w)$, representing the kinematic fluxes $\overline{u'w'}$, $\overline{v'w'}$ and $\overline{T'w'}$ respectively. The following quantities are computed according to equations in the Theory chapter on the basis of the chosen averaging interval:

- Friction velocity u_* (only positive values allowed)
- (Vertical turbulent) momentum flux M (expected to be negative, but positive values allowed)
- Bulk transfer coefficient for momentum (drag coefficient) C_D (only positive values allowed)
- (Vertical turbulent) buoyancy flux H (assumed equal to sensible heat flux)
- Obukhov length L
- Turbulent kinetic energy TKE

Other output time series of the script are:

- horizontal wind speed (30 min mean)
- sonic temperature (30 min mean)
- variances and covariances

In version 1 of the processing script, the output solely relies on Sonic data. For flux calculation, this requires the extra input of a density value which the mean density for the measurement period has been used for (taken from AWS data). The temperature shall be converted to potential temperature before entering calculations. But this needs pressure data which are not available from the Sonic. In the second version of the script, the minutewise density and pressure data from the AWS will thus enter the calculations to increase output quality.

Figure 5.12 shows the results for all output quantities over the course of the test day, computed using a 15 minutes interval for variance and covariance calculation.

For the computation of the results of this study, the used time intervals in the outlined processing steps have been changed: (I) rotation is performed on time intervals of one

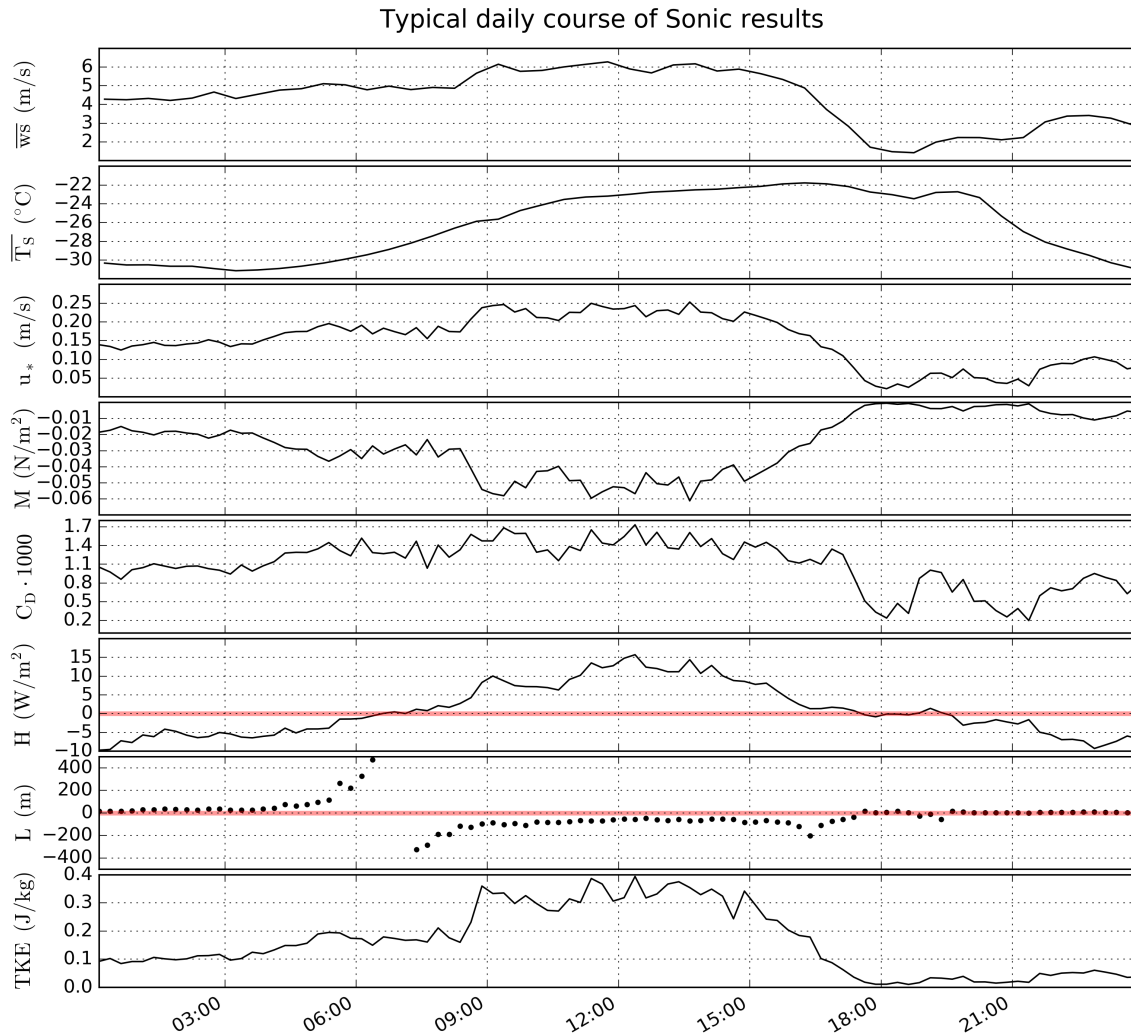


FIGURE 5.12: Results from Sonic data, based on a fixed density (0.956 kg/m^3 as the mean density during the measurement period, calculated using AWS data).

hour, (II) no FFT is performed for high-pass filtering the data, but the data are detrended on the duration of an flux averaging interval which is set to 15 min. This interval length showed to be a reasonable choice to receive fluxes of good quality, see section 5.3.5 below.

5.3.3 Quality control of Sonic data

Comparison to the AWS air temperature showed that Sonic temperature is reliable and will be used to compute the results in this study. For data quality reasons, no turbulence data will be computed if horizontal wind speeds on the averaging interval are below 1 m/s because with lower wind speed, electric and physical errors gain more influence on the measurement due to the way wind speed values are generated. The uncertainty of very low wind speed values therefore becomes too large to further enable the use of mean horizontal wind speed in the results (needed e.g. for the calculation of drag coefficient). Furthermore,

with vanishing wind speed and the heating of the instrument switched on continuously, the heat flux may be influenced artificially. It is recommended by the manufacturer to turn on the sensor head heating only occasionally when icing of the sensors must be expected. In the study by (Grachev et al., 2007), results for wind speeds below 1 m/s have been neglected, too in order to reduce errors in the final results. Together with missing data and outliers, 4.7% of Sonic data are nan on the scale of 1 minute resolution after this pre-processing scheme that has been outlined.

Additionally, data from wind directions episodes from a potentially disturbed fetch are excluded as well (dir is only allowed to be in $20 < \text{dir} < 140$ degrees). Overall, 15.7% of data are either excluded due to these two quality constraints of too low wind speed or disturbed fetch, are missing or are excluded as outliers in Sonic raw processing over the full measurement period 10 Dec 2013 to 31 Jan 2014.

5.3.4 On the use of Theta instead of T

It must be noted that on the plateau $\overline{\theta'w'}$ is significantly larger than $\overline{T'w'}$. As we can tell from the definition of potential temperature, the difference between Theta and T increases with topographic height (due to decreasing pressure), leaving Theta to be about 30 K larger than T at the Kohnen site. In addition, Theta increases with temperature at constant pressure. This causes the fluctuations in Theta to increase with temperature as well causing $w'\text{Theta}$ quer to be generally larger than $w'T'$ (for $p < 1000\text{hPa}$). From theoretical considerations we can find the relation

$$\overline{\theta'w'} \approx \frac{\bar{\theta}}{\bar{T}} \cdot \overline{T'w'}. \quad (5.2)$$

Inserting $\bar{\theta}$ and $\overline{T'w'}$ from the Kohnen campaign this relation yields that $\overline{\theta'w'}$ is on average 11.6% larger than $\overline{T'w'}$. This number compares very well to the mean difference between the measured fluxes $\overline{\theta'w'}$ and $\overline{T'w'}$ (employing minutewise pressure data) which amounts to 11.3%.

5.3.5 Sonic parameter test: Averaging interval

As described before, the hourly time series of u, v, w and Theta, i.e. 60 minutes of data, are divided into blocks of equal length. The duration of such a block of data is called averaging interval or averaging length since the covariance (i.e. the flux) is computed on this interval and we take $\text{cov}(x, y)$ as $\overline{x'y'}$. Detrending is performed on the block prior to the covariance computation. The choice of averaging length will therefore influence the flux results.

We shall choose an averaging length that maximizes the flux because the covariance will be underestimated if not enough turbulent eddies are captured or if high-pass filtering (by

applying the detrending) erases too many small frequencies, cutting away the turbulent transport from larger eddies. We can use maximization as a criterion for the choice of an appropriate averaging interval because Sonics are known to generally underestimate the fluxes as a consequence of e.g. physical limitations in sensor size and response. Furthermore, the influence of phenomena from larger scales than the desired turbulent eddies are already outruled by linear detrending on the data interval.

In the convective regime, eddies are larger in size than in the stable regime. We therefore expect differences in an appropriate averaging length depending on thermal stratification. In ecology studies (e.g. investigating CO₂ fluxes) and in mid-latitudes in general, a length of 30 minutes has become the standard choice. In the Antarctic boundary layer however stratification is more stable in general and we expect a shorter averaging length to yield better flux estimations.

To investigate this issue we randomly choose nine days within the campaign time, covering a wide range of daily mean wind speeds from 2.1 to 6.2 m/s. Flux calculation is performed for these days with the use of five different averaging lengths: 5 min, 10 min, 15 min, 30 min and 60 min. The 5 min interval will yield 12 flux values per hour, the 60 min interval only one. To enable comparison, hourly flux means are calculated. The flux data base for comparison of the averaging lengths will therefore offer 24 values for each of the nine chosen days. On this hourly basis, no preferred interval length can be found to generally maximize the flux. We therefore distinguish the maximum of the convective period from 0900 to 1500 from the maximum of the stable period from 2100 to 0300 and compare the mean fluxes over these periods. Figure 5.13 shows the results for heat and momentum flux separately in the form of deviations in percent toward the values gained from the 10 min averaging length. The picture is surprisingly symmetric: During the convective period fluxes become saturated for a 30 min averaging interval and decrease with shorter intervals whereas during the stable period an averaging length as small as 5 min appears to be the optimal choice and flux values decrease with longer intervals. However, the flux calculation routine cannot distinguish between different stratification regimes and needs a fixed averaging length for a straight-forward working procedure. We therefore decide for a compromise of 15 minutes which returns four flux values per hour and assume the flux error to be $\pm 10\%$ according to Fig. 5.13. This compromise is backed by the comparison of daily flux means and the nine day overall flux mean which both show a maximum flux for the 10-15 minutes averaging length.

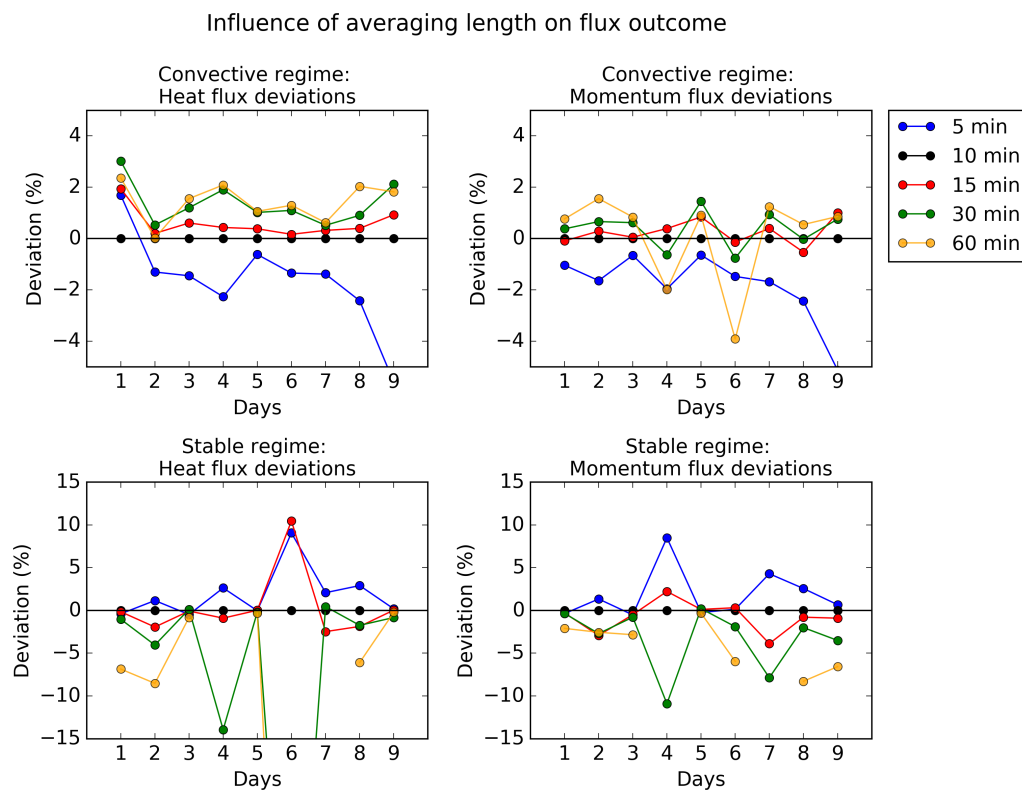


FIGURE 5.13: Comparison of five different averaging lengths used for dividing the fluctuating Sonic data time series into blocks of equal length for flux calculation. Detrending (high-pass filtering) and covariance calculation are performed on these data intervals which impact the heat and momentum flux outcome. Data points show deviations from the fluxes gained using an interval of 10 min duration.

CHAPTER 6

Results

6.1 Meteorological conditions

6.1.1 Near-surface variables

During the campaign from 10 Dec 2013 to 31 Jan 2014 temperature, wind speed and relative humidity in the lowermost 2 m show a distinct diurnal cycle (Fig. 6.1 and D.1 in appendix D). The large variability in temperature over the day suggests occurrences of unstable stratification during daytime and stable stratification during the night as would be expected for a land station in lower latitudes (compare daily cycle of $\Delta\theta$ in the lower left panel of Fig. 6.1). This points out the existence of a diurnal cycle in the turbulent fluxes as well. Temperatures are generally between -18 and -32°C and decrease significantly towards the end of January to range down to -40°C at night (see Fig. D.1 in the appendix D). This is due to the lower elevation angle of the sun towards the end of the short summer season. The sun was about to set soon again on 11 Feb 2014 for the first time since October (calculated for the location using this tool: <https://www.esrl.noaa.gov/gmd/grad/solcalc/sunrise.html>). Table 6.1 summarizes all mean values of interest for December and January separately. The mean temperature is in accordance with the long-term Dec/Jan mean of about -27°C (van den Broeke et al., 2005, AWS measurements from 1998-2001, Fig. 6).

Winds in January (mean wind speed 3.8 m/s) were calm compared to the long-term Dec/Jan mean wind speed of 4.5-5 m/s (van den Broeke et al., 2005, Fig. 6) whereas during December, mean wind speed was about equal to the long-term mean of 4.8 m/s. Daily mean

wind speeds did not exceed 7 m/s and have usually been larger than 2 m/s (Fig. D.1 in appendix D). In general, wind speeds are larger during daytime than nighttime with a fast decrease after 1500 UTC. They reach their minimum before 2100 UTC and rise again during the night. The mean wind direction is 49 degrees, i.e. from Northeast with a large directional constancy of 0.92 (Dec) and 0.88 (Jan). Directional constancy is defined as the ratio of the vector mean wind speed to the scalar mean wind speed. A value of unity designates that the wind direction has not changed over the averaging period and a value of zero suggests a completely symmetrical distribution. This large value, combined with the mean wind direction being down-slope strongly suggest that the surface-flow is katabatically influenced which is according to expectation as explained in chapter 2 before. However, the wind direction exhibits a daily cycle as well with slightly more easterly nighttime winds. This may be due to the interplay between synoptic and katabatic pressure gradient forces between day and night.

Relative humidity with respect to ice saturation oscillates around 90% with a few episodes below 70% and a few episodes above saturation. The mean value (see Table 6.1) is slightly below the long-term mean of 93% (van den Broeke et al., 2005) which makes sense because the winter period is much longer (and much colder) than the summer season at the site (assuming nearly constant specific humidity throughout the year because the atmosphere is generally dry on the inland ice plateau).

From the records of meteorological observations, we see that in total, nine precipitation events have been observed during the 53 days of Sonic measurements that exceed the description of light snow fall and one (comparably) heavy precipitation event is listed. However, none of them was a heavy precipitation event in its strict sense as none exceeded the threshold of 1 mm water equivalent (source: Dr. Birnbaum). The most common precipitation types were ice crystal precipitation and light snow fall with at least moderate ice crystal precipitation for 17 times during the campaign. Wind speeds have always been below 10 m/s except for December 21st (see Fig. D.1). No major low-pressure system took its path over the station during the two months (see pressure curve). Blowing snow has been observed only on January 3rd and heavy drifting snow was recorded on five days. Ground fog occurred on ten days, hoar frost on eleven days (e.g. every day from 16 Jan to 21 Jan). On 19 Jan, there was surface hoar observed (hoar crystals on the snow). High clouds were the most common cloud type, while Belke Brea (2015, Master's thesis) computed 18% of the days to be overcast (defined by at least 75% cloud fraction in the low layer). She also found 18% of the days to be clear sky days (no clouds at any layer or if high clouds do not remain longer than two hours). Periods of low cloud cover appear to coincide with periods of lower temperatures (Fig. D.1) while an increased cloud cover tends to coincide with larger temperatures.

Except for the weak January winds, mean temperatures and wind speeds are according

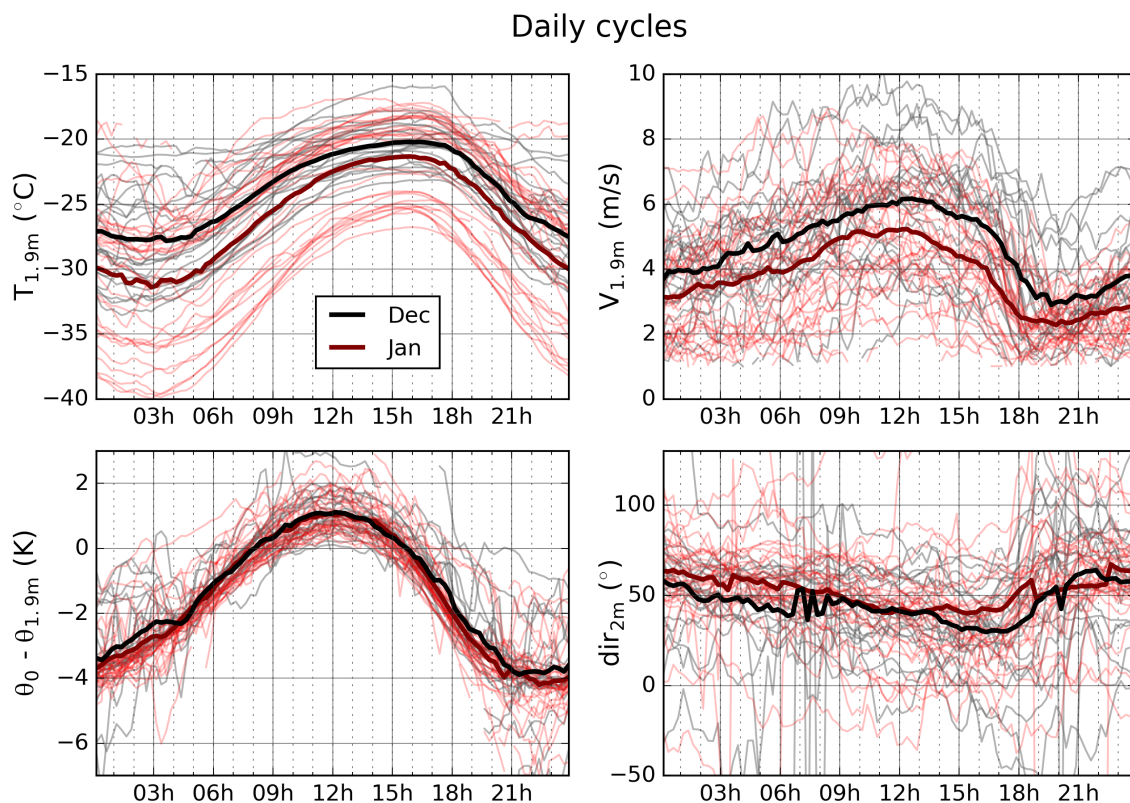


FIGURE 6.1: Daily cycles of near-surface variables from 10 Dec 2013 to 31 Jan 2014 for temperature, wind speed (both from Sonic at 1.9 m height), vertical difference in potential temperature (where surface temperature is determined via longwave radiation), and wind direction in 2 m height from AWS measurements (0° corresponding to southward, 90° westward and 180° southward wind). Individual days depicted as thin lines, monthly means as thick lines.

to the long-term mean (van den Broeke et al., 2005). The daily mean temperatures and wind speeds behave very similar to the conditions that van As et al. (2005) encountered at Kohnen during the ENABLE campaign from 7 Jan to 11 Feb 2002 (later in this study, turbulent fluxes from their campaign will be compared to our results). The difference, however, is that they observed above-average 2 m wind speeds of 5-11 m/s in the first half of January whereas we observed below-average winds in the same period. The pronounced diurnal cycle in near-surface temperature and wind speed is primarily observed during the summer season, it is much weaker during winter (cf. Figure in Birnbaum et al., 2010). Compared to data measured at Neumayer III Station (on shelf ice, -70.65° lat/ -8.25° lon) during the same period as the Kohnen campaign, climatological differences to Kohnen Station are obvious (see Fig. D.2 in appendix D). Due to the proximity to the sea and small height above sea level, temperatures at Neumayer (generally about -5°C) are much higher than at Kohnen with a weaker or vanishing diurnal cycle, especially when wind speeds are large. The common daily temperature range of 10 K from Kohnen occurs rarely

here. Wind speeds are generally of comparable strength while the daily cycle is less regular. Wind speeds at Neumayer rise well above 10 m/s under the impact of low pressure systems. The pressure range is 5 hPa larger than at Kohnen. Relative humidity values with respect to water are usually about 80% with episodes above 90% especially when winds are large. Moisture is brought onto the ice shelf from the ocean from a predominantly eastern wind direction. Drier episodes occur when winds come from a southern direction, bringing across dry air from the continent. The wind direction is not as steady as at Kohnen.

6.1.2 Summer warming event

During the campaign period several nights do not show a clearly shaped night-time temperature minimum. This behaviour can be attributed to the presence of (low-level) clouds. There are three nights which completely lack the usually strong night-time cooling. The case of 26th/27th December 2013 is particularly strong and it is the only event among those three when the wind direction has a western component, see Fig. 6.2. Its character is similar to the summer warming event demonstrated by Argentini et al. (2013) for Dome C for mid of January 2011 but much shorter. Argentini et al. (2013) observed a temperature rise suppressing the typical diurnal cycle for a period of six days due to the advection of moist and warm air from the coast which led to increased cloud formation and consequently increased downward long-wave radiation. Convective activity was comparably intense for the site and mixing heights were large even during night-time. Such conditions are of particular importance in winter when occasional winter warming events can increase near-surface temperature up to summertime levels and cause significant amounts of precipitation.

From Fig. 6.2 we find that from 25 to 27 December, the wind at Kohnen Station blows from north-western direction instead of the typical north-eastern direction, i.e. moist air from the coast could have reached the plateau station. In the evening of Dec 25th the sky is almost fully covered by high-level clouds, one day later low-level clouds fully overcast the sky. During that time, the backscattered longwave radiation almost reaches the strength of the upward longwave radiation, causing night-time temperatures at the surface and in 2m height to be as high as day-time temperatures. The difference between both temperature is unusually small during that night. The interruption of the diurnal cycle persists until clouds vanish at the end of Dec 27th and in the following, conditions quickly return to normal. Due to the duration of only one night, this event does not lead to a general increase in temperature in contrast to the six day event from Argentini et al. (2013) but the night-time warming effect itself is very much comparable between Kohnen Station and Dome C. Although wind speed was not larger than during the preceding days the surface heat flux was particularly large owing to the high nighttime temperatures. Nevertheless, the heat flux measurements on that day may suffer from inaccuracies because the wind blows from

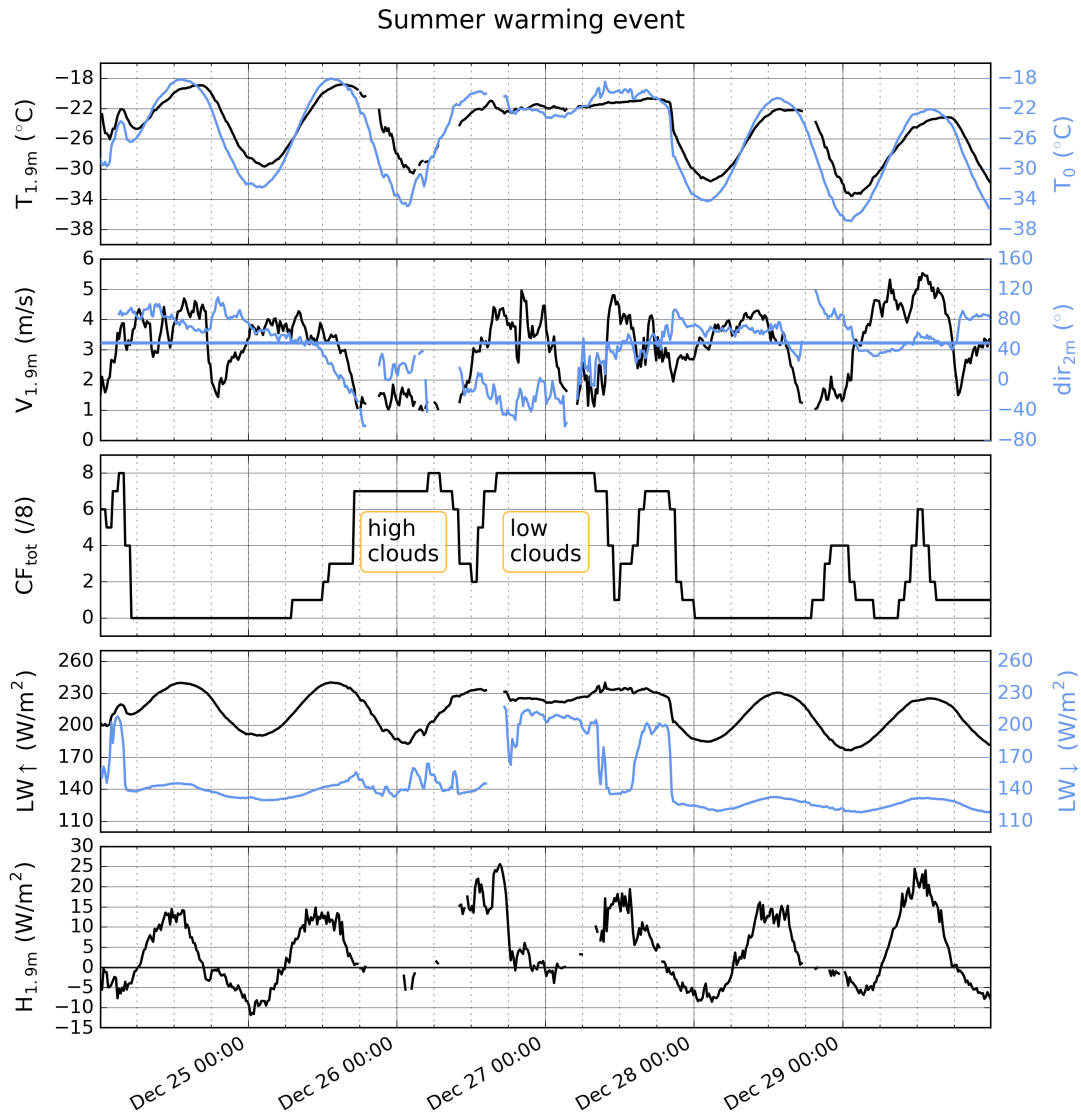


FIGURE 6.2: Determining quantities (15min averages) for the summer warming event from 26/27 Dec 2013. Mean wind direction indicated as blue horizontal line in second panel.

the direction of the station's containers. These cases of perturbed flow cannot give a true picture of turbulence at the site and will therefore be neglected for further analysis later.

6.1.3 Boundary layer evolution

The mean profiles of potential temperature and wind speed (Fig. 6.3) picture the typical diurnal cycle of the ABL at Kohnen in the period from 10 Dec 2013 to 31 Jan 2014. Solar insolation during day-time induces a surface warming which leads to the development of a shallow unstable layer in the lowermost 10 to 20 metres (considering daily profiles; examples from six days shown in Fig. 6.4). Above, the air is neutrally stratified up to 50

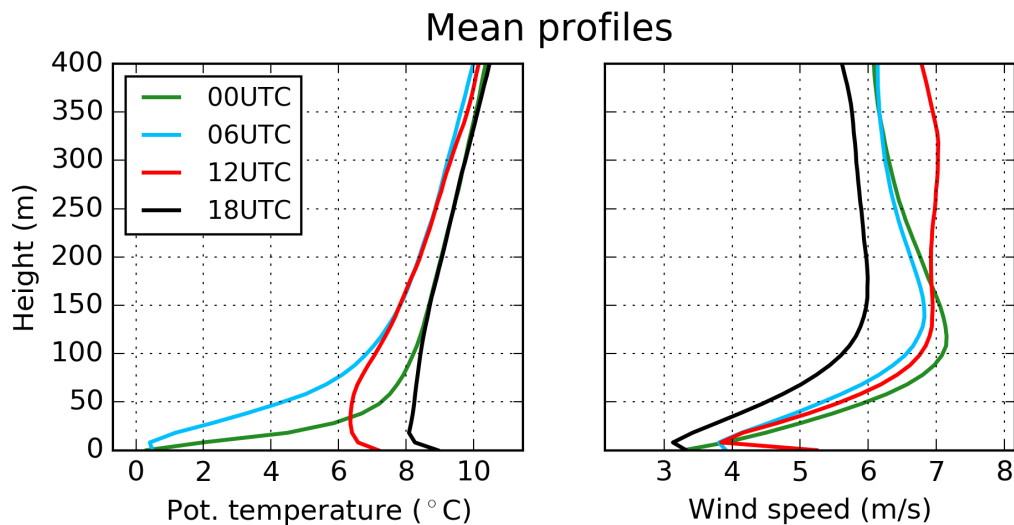


FIGURE 6.3: Mean radiosounding profiles of potential temperature and wind speed at Kohnen Station from 07 Dec 2013 through 31 Jan 2014. Initialization via AWS data.

metres in the mean profile while in the daily profiles this varies significantly: the near-isothermal conditions typically reach up to heights between 50 and 200 metres, sometimes even 400 m. Buoyancy-driven turbulence within this convective layer transports heat upwards, warming the lower few hundred metres of the air mass. Temperatures therefore rise until the late afternoon, typically causing the 1800 UTC profile to be neutrally stratified over a large depth, which is also visible in the weaker stability of the mean 1800 UTC profile. Sometimes, neutral conditions then reach down to the surface. Typically, the lowest metres above the surface are less unstable in the afternoon than at noon, sometimes already stable. After the breakdown of midday convection, significant over-night cooling sets in due to the absence of solar insolation. Radiative cooling of the snow surface causes a fully stably stratified ABL. A strong surface-based temperature inversion develops until midnight, leaving the surface temperature on average at least 8 K colder than in the afternoon. At midnight, the surface-based inversion in the mean profile is about 50 metres deep with a vertical temperature difference of about 6.5 K. In the daily profiles, its thickness varies between 30 m and 80 m. Radiative cooling leads to a further cool down of the lower 400 metres during the following hours, especially of the lower 100 metres, suggesting that the surface-based temperature inversion further increases and deepens after midnight. At 0600 UTC however, surface warming has already set in after sunrise, leaving the lower 10 metres typically neutrally stratified. On some days, stratification is already unstable at that time. On average during the campaign, the ABL remains stably stratified throughout the whole day above a height of 100 metres with a potential temperature gradient of approx. $+0.75 \text{ K}/100 \text{ m}$. However, conditions in a few hundred metres above the ground clearly shift from near-neutral in December to moderately stable by the end of January when the

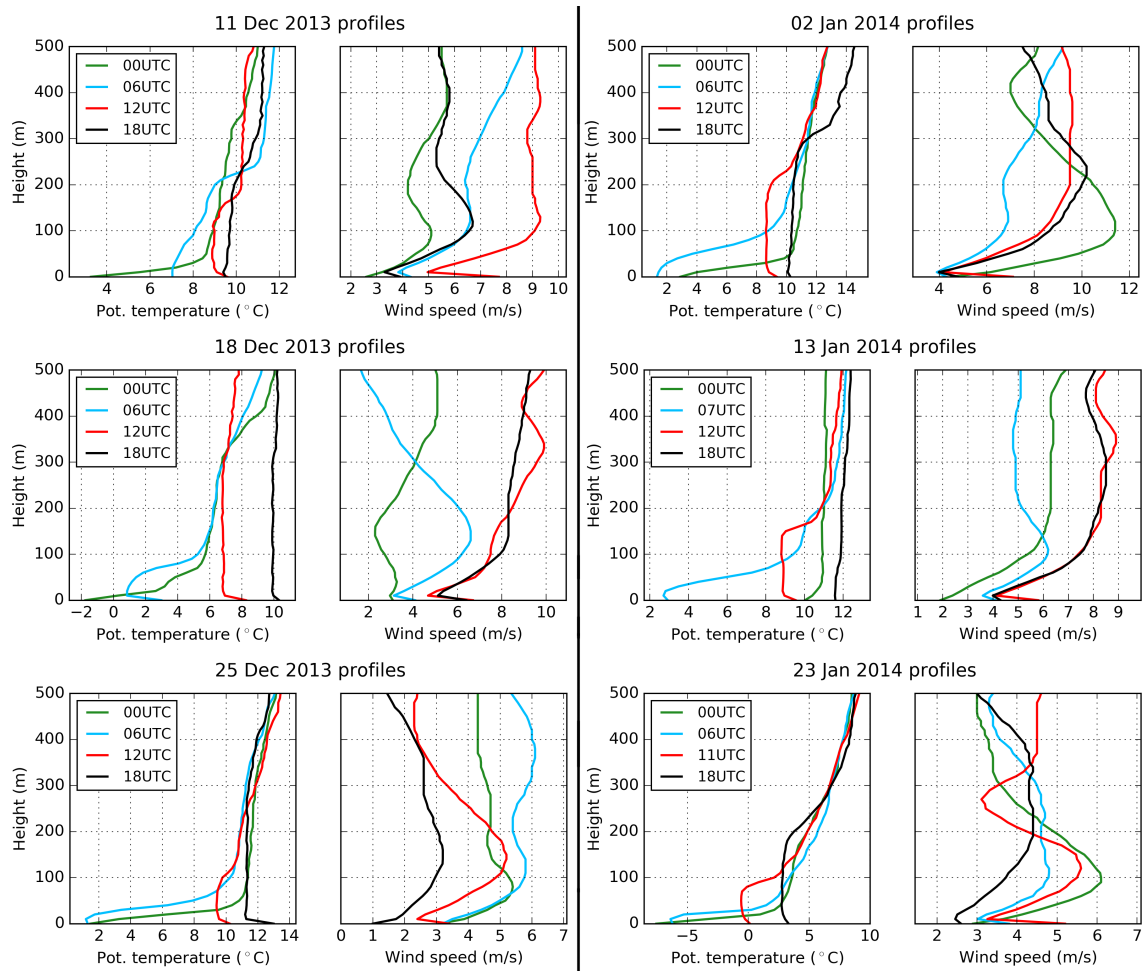


FIGURE 6.4: Examples of profiles of potential temperature and wind speed from radiosounding for six individual days. Initialization via AWS data.

short summer season is already coming to an end.

At night, the wind speed mean profile exhibits a well-developed maximum in 100-130 metres height. This low-level jet (*LLJ*) is most likely katabatically driven due to the large temperature inversion at night over the slightly-sloping surface of the Kohnen area. In the daily profiles, the height of its maximum speed varies between 30 and 200 metres. After the start of day-time convection, the *LLJ* vanishes until noon in the mean profile due to destruction of the temperature inversion but wind speed values remain similarly strong as during the night until the breakdown of convection. Until 1800 UTC, mean wind speed above 30 metres is at least 1 m/s weaker than at noon and also below that height, it is significantly weaker.

The findings concerning ABL evolution compare well to the tetheredsonde measurements performed during the ENABLE campaign at Kohnen Station from Jan 7 to Feb 11 2002 (see van As et al., 2006). However, they found a larger temperature deficit in the nighttime stable layer and on average, the *LLJ* to be at a lower height. This is most likely

because their measurement period excludes the high-summer month of December but is closer to the winter season when insolation angles are already smaller than during the analysed campaign. The ABL diurnal cycle itself is very much comparable to continental mid-latitude regions although the Antarctic ABL is much shallower with larger nighttime inversion strengths and weaker daytime convection of course. Above the flat Cabauw site (Netherlands) for example, a LLJ develops in many summer nights at the same height like the mean LLJ at Kohnen Station, there created by decoupling and inertial oscillation (see Holtslag et al., 2013).

Note that the initialization of wind speed at 2 m height is performed via AWS measurements but radiosonde wind speed measurements with a typical first measurement level at 10 m are done using the onboard GPS sensor. This can lead to uncertainties in the lower metres of the profile. Nevertheless, sharp wind speed minima at about 10 m height for all launching times except for the midnight profile are strikingly frequent. Almost every noon profile of the individual days shows this behaviour while for the other launching times, it does not appear on a daily basis. Generally, a decrease of wind speed with height would be highly problematic in the application of MOST because the theory assumes the opposite. Upward momentum fluxes due to an inversed wind shear would be the consequence and could not be displayed by MOST. No doubt the wind speed must vanish at the surface nevertheless. We will see that the direct flux measurements by the Sonic in 1.9 m height show no such problematic behaviour of regular daytime upward momentum fluxes but they may be corrupted by this phenomenon.

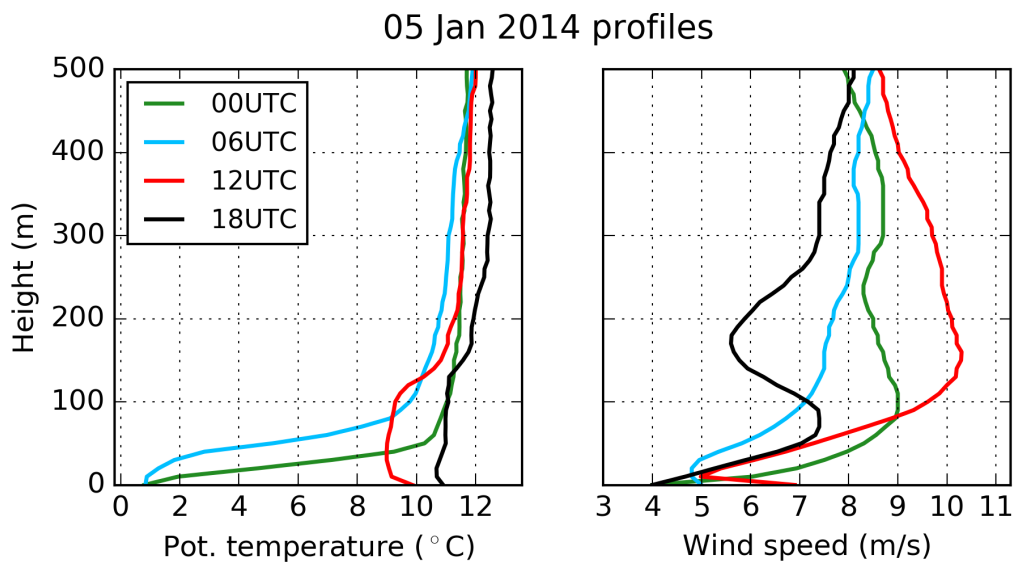


FIGURE 6.5: Profiles of potential temperature and wind speed at Kohnen Station from four radiosoundings on 05 Jan 2014. Initialization via AWS data.

The wind speed profile from Jan 05 in Fig. 6.5 may have captured an inertial oscillation.

These oscillations can occur when triggered by the sudden reduction of friction in the mixed layer before 1800 UTC when wind speeds decrease rapidly during the collapse of the convective system (see also van As and van den Broeke (2006)). The wind speed minimum at 180 m height seems like a negative overshoot of the sudden decrease in wind speed that generally occurs from 1500 UTC onwards during the campaign (see Fig. 6.1). When this wave that we see in the wind profile swings back towards larger wind speeds after midnight, the oscillation could support the LLJ wind speed maximum or at least interfere with katabatic effects as shown by van As and van den Broeke (2006). They showed that katabatic-like wind profiles can be produced by an inertial oscillation. The daily course of their modelled wind speed profile over a non-sloping surface exhibited wind speed maxima in the same heights as where we expect the katabatically-driven LLJ to be.

6.2 Near-surface turbulent fluxes

6.2.1 Daily cycle

The turbulent quantities at 1.9 m height follow the distinct diurnal cycle of the near-surface wind speed and temperature. They are shown in Fig. 6.6 which demonstrates their mean daily course in December and January. The purely wind-determined quantities momentum flux M , friction velocity u_* (which determines M), as well as the drag coefficient C_D grow until the afternoon. When the wind speed after 1500 UTC steeply decreases, its turbulent counterparts significantly reduce as well. Momentum flux was overall smaller in January when winds have been weaker than in December. u_* ranges up to 0.4 m/s with monthly means of 0.18 m/s (Dec) and 0.15 m/s (Jan). The latter is close to the long-term mean of 0.14 m/s calculated by turbulence parametrization for AWS measurements from 1998 to 2001 by van den Broeke et al. (2005)). The range of C_D differs during the convective and stable regime, ranging between 1 and $2.5 \cdot 10^{-3}$ in the convective period from 0600 to 1500 and from 0 to $2 \cdot 10^{-3}$ during the rest of the day.

The sensible heat flux H ranges between -15 and +25 W/m² with typical values of -10 W/m² at night under stable stratification and +15 W/m² at noon during the convective period (see also turbulence time series in Fig. D.3 in appendix D). The SHF (and its kinematic counterpart $\overline{\theta w'}$) are directed upward at daytime on each of the 53 days of the campaign owing to the comparably large solar elevation angle at noon during the summer months that causes the surface to warm. When angles at nighttime are lower (the sun will not set until February), the surface temperature falls below the air temperature causing sensible heat fluxes to be directed downward generally between 1800 and 0600. This diurnal cycle of stable stratification at night and slightly unstable stratification during the day is also

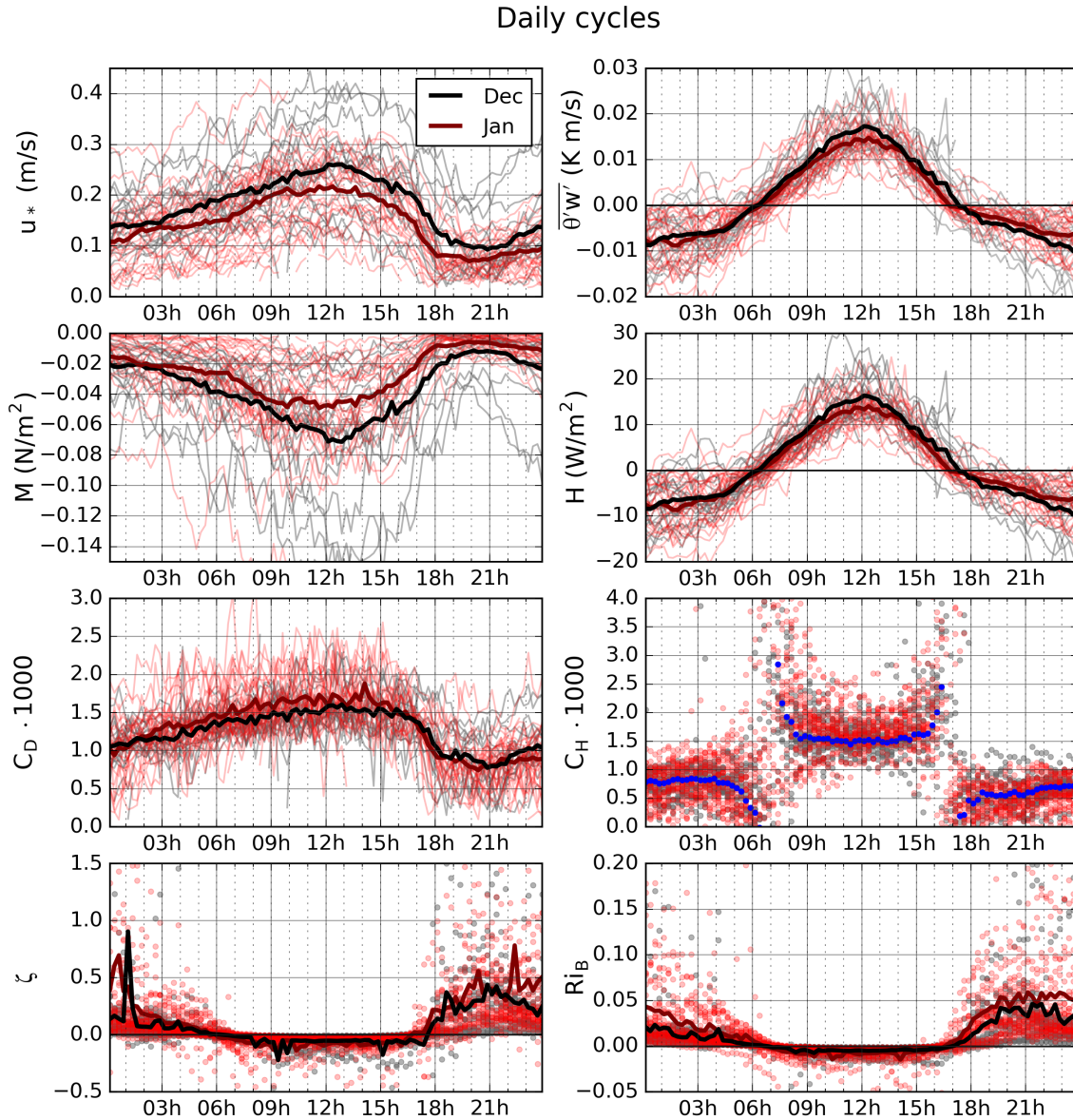


FIGURE 6.6: Daily cycle of turbulence related quantities in the surface layer from 10 Dec 2013 to 31 Jan 2014 for friction velocity u_* , vertical turbulent momentum flux M , drag coefficient C_D , stability parameters $\zeta = z/L$ and bulk Richardson number Ri_B ; kinematic sensible heat flux $\overline{\theta'w'}$, vertical turbulent sensible heat flux H , bulk transfer coefficient for heat C_H . Individual days depicted as thin lines, monthly means as thick lines.

visible in the daily cycle of the two stability parameters $\zeta = z/L$ and Ri_B in Fig. 6.6. From the nighttime mean values of these parameters (see Table 6.1 for summary) we calculate the surface layer to be about 60% more stable in January nights compared to December nights because the winter season is approaching. Despite the mean SHF being directed upward during the measurement period, the lowermost atmosphere is on average stably stratified. This is no contradiction because SHF depends not only on vertical temperature difference but also on wind speed. Since wind speeds are larger during the day, turbulent

mixing can be stronger than at night, causing the heat from the surface to be transported upwards more efficiently than the downward transport of heat during the night. Daily mean SHF as measured by an eddy-covariance system during the ENABLE campaign (see van As et al., 2005, January measurements only) range from -10 to $+8$ W/m^2 which are larger values than we observed during the campaign (cf. Table 6.1). This is probably due to the weaker wind that we encountered in January in contrast to the above-average winds during ENABLE for the same month. Climatologically, the net radiation changes from positive to negative between mid-January to mid-February, causing the daily mean SHF to become negative (downward) as well in February (van As et al., 2005). Long-term means (and therefore wintertime values) of θ_* are larger than during our campaign (cf. Fig. D.3 in appendix D) whereas the long-term SHF mean from 1998-2001 as calculated from AWS measurements is -8 W/m^2 (van den Broeke et al., 2005) because radiative cooling in the rest of the year is much stronger than in December and January. The seemingly asymptotic behaviour during neutral conditions in the bulk transfer coefficient for heat C_H is due to measurement uncertainties and will be explained in the next section. Note that values above $2 \cdot 10^{-3}$ and below $0.5 \cdot 10^{-3}$ are most likely unphysical.

6.2.2 Negative C_H values and thermal emissivity of the snow surface

The time series of the bulk transfer coefficient for heat C_H and even its mean daily cycle (see Fig. 6.7) generally show negative values twice a day during the transition between both stability regimes i.e. in the late morning and in the afternoon. C_H is calculated by

$$C_H = \frac{\overline{\theta'w'}}{\overline{u}(z) \cdot (\overline{\theta}_0 - \overline{\theta}(z))} \quad (6.1)$$

(see also equ. 4.15) where the overbar denotes 15 min mean values according to the length of the Sonic averaging interval. C_H depends on height z , here calculated for $z=1.9$ m. As obvious from the equation above, negative values originate from a different sign of the kinematic SHF $\overline{\theta'w'}$ and the vertical temperature difference $\Delta\theta = \overline{\theta}_0 - \overline{\theta}(z)$ between the surface and measurement height.

Generally speaking, negative C_H values indicate the existence of counter-gradient fluxes: During the time of different sign of the two determining terms the direction of the measured SHF at 1.9 m height is opposite to what we would expect from the measured vertical temperature gradient. These cases cannot be depicted or explained by MOST and thus must be excluded in the calculation of any parametrizing ψ function. Additionally, we would not expect such counter-gradient fluxes just above the surface, they may be observed in some decameters height. A thought experiment can offer a potential explanation without violating theoretical expectations: Since the cooling and warming of the surface is driven

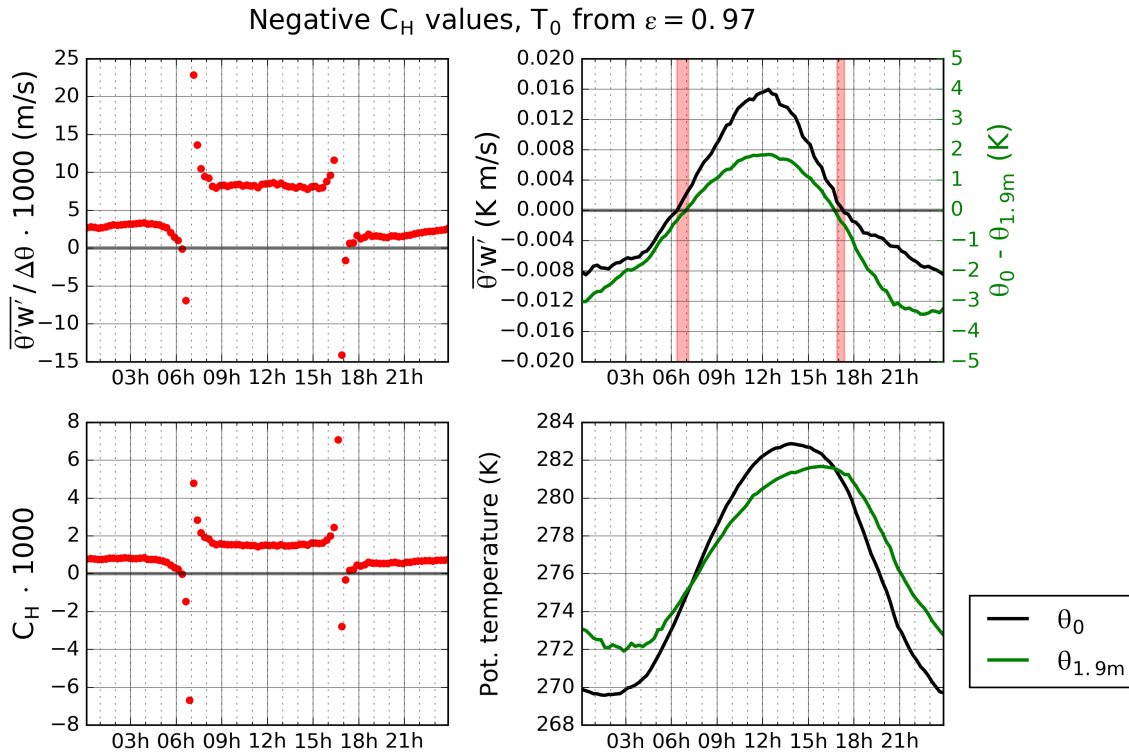


FIGURE 6.7: **Right upper panel:** Mean daily cycle of the terms that determine the sign of C_H : kinematic sensible heat flux $\overline{\theta'w'}$ and vertical temperature difference $\Delta\theta$, episodes of different sign resulting in negative C_H values are indicated in light red. **Left upper panel:** Consequence of these two episodes for the mean ratio of both terms, also displayed in values for C_H (**left lower panel**). For a clearer demonstration of the effect, values for both left panels are calculated using the mean daily cycles of the determining quantities. **Right lower panel:** Lagging of air temperature as measured by the Sonic in 1.9 m height behind the surface potential temperature θ_0 (mean daily cycle over the full campaign period).

by insolation, the temperature may not be steadily increasing/decreasing with height in the layer between measurement height and the surface. Instead, the profile may be bent during the time of near-neutral conditions in the late morning and afternoon. That means after sunrise, a shallow unstable layer would quickly develop above the surface, creating upward net transport of heat by turbulence before the surface temperature is overall larger than the temperature at sensor height. In the afternoon when solar elevation is low, a shallow unstable residual layer would remain just below sensor height, causing the Sonic to measure small upward heat fluxes while the surface temperature has already dropped below the temperature at 1.9 m height. This thought experiment would generally explain the temporal shift between $\overline{\theta'w'}$ and $\Delta\theta$ as depicted in Fig. 6.7.

The problem with this reasoning is that the profile bending could not last longer than a few minutes because it would be quickly destroyed by turbulent mixing in such a shallow layer of only 1.9 m depth. A simple reason for SHF and $\Delta\theta$ to be out of phase would be an

error in $\Delta\theta$. The error of that quantity is inevitably large because values from two different measurement systems are contained: air temperature is measured by a conventional sensor or, in our case by the Sonic whereas the surface temperature calculates from broadband upward (and downward) longwave radiation. Using the air temperature from the PT100 sensor in the AWS at approx. 1.4 m height did not improve the situation for C_H as is to be expected. From the calculation of T_0 (equ. 5.1) it is obvious that the choice of thermal emissivity of the snow surface impacts the strength of the vertical temperature difference and hence the duration of negative C_H episodes. We saw that for an emissivity of 1.0, not only C_H values are too large in general at noon and too low during the rest of the day (see Fig. 6.8) but negative C_H episodes last more than one hour on average. Both of these facts led us to conclude that an (often assumed) emissivity of 1.0 is not an appropriate choice for local surface conditions at Kohnen. When trying different emissivities smaller than 1.0 we saw that with decreasing emissivity, values of C_H improve in general toward typically expected values and also the duration of the negative episodes decreases significantly.

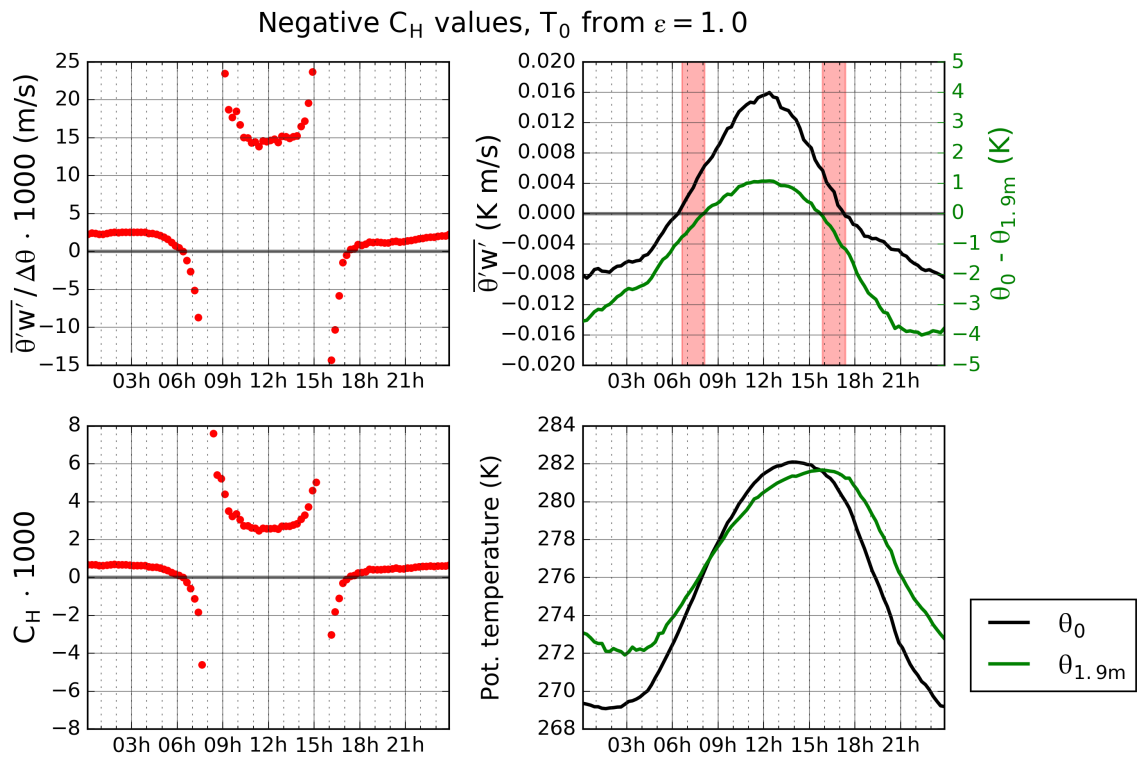


FIGURE 6.8: Like Figure 6.7 (also the same scaling) but using a thermal emissivity of 1.0 for the calculation of surface temperature. The choice of ε clearly alters the calculated values for surface temperature, therefore $\Delta\theta$ and C_H .

To go one step further, we can minimize the duration of negative C_H episodes by nullifying $\Delta\theta$ for $\overline{\theta'w'} = 0$, i.e. for neutral stratification (see right upper panel in Figs. 6.7 and 6.8). Choosing only situations for which $|\overline{\theta'w'}| < 0.001$, we can calculate an optimal emissivity

value that enables $\Delta\theta = 0$. Assuming constant pressure, R_d and C_p for the lowermost 2 metre layer, the condition $\Delta\theta = 0$ becomes $\Delta T = 0$ and thus $T_0 = T_{\text{air}}$. Consequently, we insert T_{air} for T_0 into equ. 5.1 during situations of $|\overline{\theta'w'}| < 0.001$ and solve for ε :

$$\varepsilon = \frac{LW \uparrow + LW \downarrow}{LW \downarrow - \sigma T_{\text{air}}^4} \quad (6.2)$$

For T_{air} we choose the 1.4 m temperature as measured by the AWS at wind speeds above 3 m/s to enable sufficient ventilation. Emissivity values larger than 1.0 and smaller than 0.80 are excluded as outliers. Figure 6.9 shows the resulting values for ε from all 177 cases that fit the mentioned constraints. For error calculation, an uncertainty of 0.5 K is used for T_{air} and an uncertainty of 5 W/m² for the radiation measurements (according to instrument specifications). Both the mean and median value for ε yield 0.94 (the same if Sonic temperature is used in the calculation), with an error of +0.06/-0.07. Popular ε values for natural snow surfaces are 0.97 to 0.99 but in general the range is very large since even values as low as 0.80 can be found in literature. Our result of 0.94 (+0.06/-0.07) as an average value during the campaign is therefore a little lower than expected but still plausible.

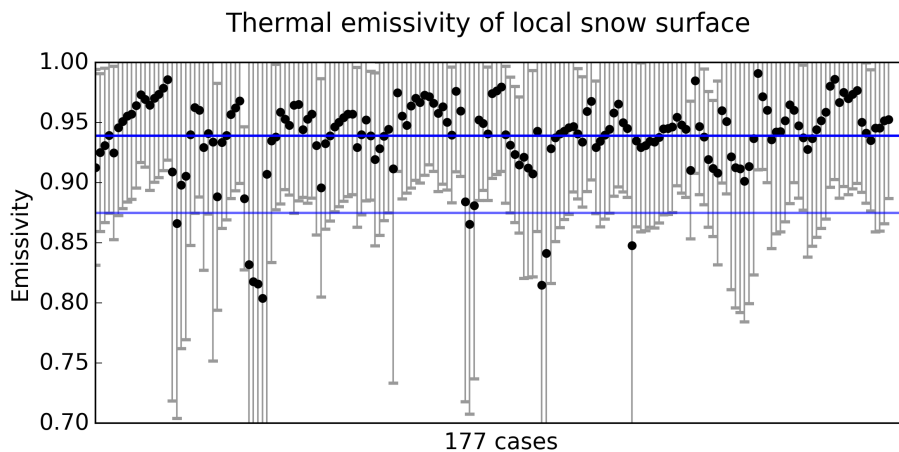


FIGURE 6.9: Calculated values for longwave surface emissivity ε at the site that minimize the duration of negative C_H episodes in the individual cases. For method and constraints see text. Mean $\varepsilon = 0.94$, indicated as blue horizontal line. Individual error bars according to Gaussian error propagation (estimate of maximum error). The lower border at $\varepsilon = 0.87$ (light blue horizontal line) corresponds to the median value of all minimum ε values according to individual error bars.

Since we cannot explain the occurrence of counter-gradient fluxes at such low heights, we tested 0.94 as emissivity for our considerations. First of all, negative C_H values still occur frequently because a constant ε value cannot optimize the situation on a daily basis but only minimize the effect on average. $C_{H1.9m}$ values themselves appear to be generally too

small (mostly lower than $1 \cdot 10^{-3}$) and the maximum daytime vertical temperature difference within the lower 1.9 m layer is almost as strong as the nighttime inversion which is unlikely to be true. Furthermore, θ_0 enters Ri_B but not ζ which leads to a change in the connection of Ri_B and ζ for a changing ε . Comparison to the results from Grachev et al. (2007) shows that Ri_B would be too small against ζ for $\varepsilon = 0.94$. From all these considerations (figures not shown here), we conclude that 0.94 is probably too low for a proper general representation of surface thermal emissivity at the site. Choosing 0.97 as a value at the lower end of the popular range therefore seems to be a reasonable compromise while generally, a large error must be assumed for $\Delta\theta$: C_H values appear to be reasonable and the dependence of Ri_B on ζ fits expectation. The resulting value of neutral C_H (at 1.9 m) is also more reasonable than the one from $\varepsilon = 0.94$. Nevertheless, when using $\varepsilon = 0.97$ the negative phase of C_H still lasts for about 30 minutes on average which is still longer than can be explained.

In conclusion, C_H and its negative phases highly depend on the choice of thermal emissivity of the snow surface. The latter is probably too variable over time to justify the assumption of a constant value. The use of $\varepsilon = 0.97$ showed to be a good compromise although negative C_H values still occur twice per day in general and a large error must be assumed for $\Delta\theta$ if constant ε is assumed. The occurrence of counter-gradient fluxes is unlikely to be the reason for this very frequent effect but non-stationary conditions in the late morning and afternoon are likely to play a role. Episodes of negative C_H will be excluded for ψ calculation later and not be depicted in time series graphs of C_H .

6.2.3 Data selection criteria

For the upcoming analysis, different sets of data selection criteria are necessary additionally to the previous data quality restrictions (see section 5.3.3 in chapter 5) in order to receive meaningful results. For applications related to MOST, there are two data selection criteria that will be used in each of the following sections. They will be described here and in the following be referenced as (a) and (b).

Criterion (a): Non-stationary episodes shall be excluded because MOST is only valid in (quasi-) stationarity. This is done by excluding data where differences in successive 15 min temperatures exceed 0.24 K (calculated by equ. 17 in Vignon et al. (2016), see also Smeets (2008)). This alone leads to a data loss of 42%.

Criterion (b): As concluded in the previous section, episodes of negative C_H will be excluded from analysis and depiction. Physically, they could only be created by counter-gradient fluxes which do not go along with MOST. However, these episodes are most probably artificially created by the uncertainty in longwave surface emissivity which enters

C_H through surface temperature. Therefore, these episodes are excluded to improve data quality which amounts to an additional data loss of 12%.

Taken together, these two data selection criteria lead to a data loss of 54%.

6.2.4 Stability parameters

In numerical climate and weather prediction models, flux parametrizations are often expressed in terms of Ri_B instead of ζ because it is computationally favourable. The use of ζ as stability parameter requires an iterative solution since it comprises u_* itself whereas Ri_B can be calculated by the common output quantities of the model at each timestep. Therefore, expressing flux parametrizations in terms of Ri_B instead of ζ is desirable. With given stability functions ϕ_M and ϕ_H the functional dependence of the gradient Richardson number and ζ is known according to equ. 4.13. However, the dependence of Ri_B on ζ is more complicated and depends on the local roughness lengths z_0 and z_{0t} (Gryanik and Lüpkes, 2017, under review). By the use of our measurements though, the dependence of ζ on Ri_B can be graphically depicted without the assumption of stability functions or roughness lengths, see Fig. 6.10 (left panel, stable regime and data selection criterion b only). The scatter of data points and the shape of the resulting dependence is very similar to the results from the SHEBA data which are depicted in Grachev et al. (2007) (11 months of in-situ turbulence measurements over drifting Arctic sea ice). For comparison, some values from their study are included into Fig. 6.10. They found a larger number of extremely stable stratification cases with $\zeta > 1$ (not shown here) because their data base covers winter months as well. Another difference is that in the present study, almost no data exceed the so-called critical Richardson number ($Ri_B \approx 0.2$). Nevertheless, the good agreement between both data sets suggests a good data quality of the Kohnen data and comparable environmental conditions to the wide flat sea ice area of the SHEBA site. Furthermore, looking at the definitions of Ri_B and ζ , the determining measured quantities u_* , θ_* , $u_{1.9m}$, $\theta_{1.9m}$ and the vertical temperature difference $|\theta_{1.9m} - \theta_0|$ probably have a similar general functional dependence as the SHEBA data which Grachev et al. (2007) derived the SHEBA parametrizations from. This suggests the applicability of the SHEBA ψ functions to our data.

The histograms of both Ri_B and ζ in Fig. 6.10 tell that stratification within the lowest 2 m of the atmosphere is mostly weakly stable and weakly unstable during the two months of the campaign. In the stable regime though, the histogram decline is smoother which means stability reaches a strength that is not as frequently reached by the convective regime. At larger wind speeds this implies a significant downward SHF. The cumulated frequencies of Ri_B and ζ amount to 56% for the stable regime and 44% for the unstable regime. That

means even during the two investigated summer months, the lowest 2 m of the atmosphere at Kohnen Station are most frequently stably stratified.

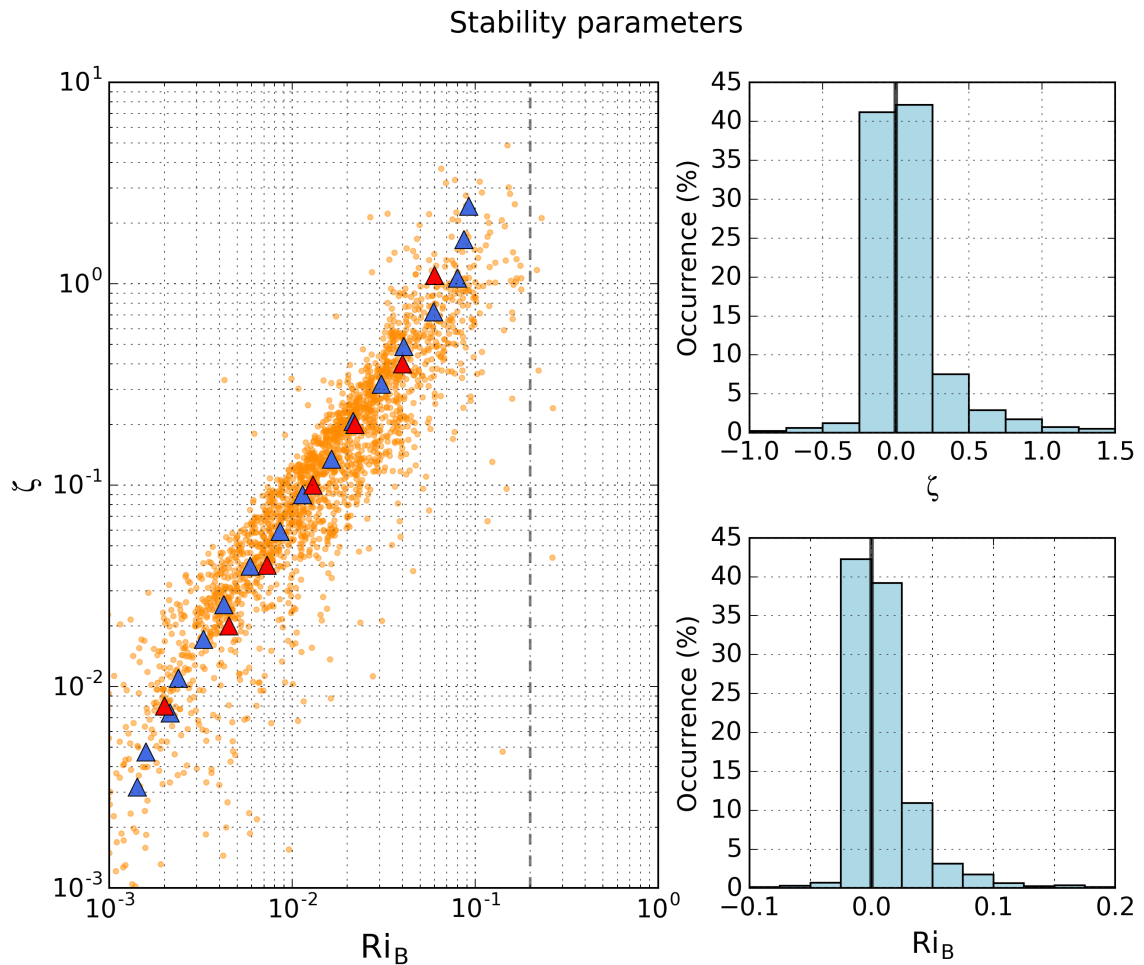


FIGURE 6.10: **Left panel:** Dependence of the stability parameter $\zeta = z/L$ on the bulk Richardson number Ri_B for measurement height $z=1.9$ m in stable conditions ($\zeta > 0$). The vertical dashed line corresponds to the critical Richardson number $Ri_B = 0.2$. Blue triangles represent Ri_B median values in bins of ζ . Red triangles correspond to values read from the graph in Grachev et al. (2007, Fig. 3, SHEBA data). **Right panels:** Histograms of both parameters.

6.2.5 Roughness lengths and neutral bulk transfer coefficients

The local surface roughness lengths for momentum and heat, z_0 and z_{0t} respectively, must be known to calculate the turbulent scales u_* and θ_{v*} (and hence the corresponding turbulent fluxes) from the parametrizations given in equ. 4.9 and 4.10, respectively. Considering the present study, they must be determined in order to receive values for ψ_M and ψ_H (equ. 4.9 and 4.10) in dependence of $\zeta = z/L$ from the measured turbulent scales and mean

quantities. z_0 and z_{0t} are closely related to the bulk transfer coefficients of momentum C_D and heat C_H under neutral stratification.

Aerodynamic roughness length z_0

The aerodynamic roughness length depends on local surface roughness. It is several orders of magnitude larger over vegetation than it is over snow surfaces. Values for local z_0 for snow and ice surfaces range from 10^{-3} to 10^{-6} m (summary by Brock et al. (2006) and study by Bintanja et al. (1995)). At Kohnen, van As et al. (2005) found a roughness length of $2 \cdot 10^{-5}$ m from eddy covariance measurements (derivation in van den Broeke et al. (2005)).

In the present work, z_0 will be determined based on equ. 4.9. The term $\psi_M\left(\frac{z_0}{L}\right)$ is one to two orders of magnitude smaller than $\psi_M\left(\frac{z}{L}\right)$ for a z_0 of $9 \cdot 10^{-3}$ m and even five to six orders of magnitude smaller for a z_0 of $1 \cdot 10^{-5}$ m. This scale analysis uses the stability function by Dyer and Hicks (1970) for the unstable regime and the one by Holstlag and De Bruin (1988) for the stable regime, covering $-1 < \zeta < 2$ which is the ζ range from the present campaign. The term $\psi_M\left(\frac{z_0}{L}\right)$ will therefore be neglected throughout the study which also is the common way of dealing with this term in other studies. Similarly, this can be shown for $\psi_H\left(\frac{z_{0t}}{L}\right)$ in equ. 4.10.

Under neutral conditions, equ. 4.9 reduces to the equation of the logarithmic wind profile for the surface layer

$$U(z) = \frac{u_*}{\kappa} \ln \frac{z}{z_0}. \quad (6.3)$$

which can be solved for z_0 :

$$z_0 = z \cdot \exp\left(-\frac{\kappa U(z)}{u_*}\right) \quad (6.4)$$

We approximate neutral conditions to near-neutral conditions of $|\zeta| < 0.02$ and only consider cases with u_* smaller than 0.3 m/s which is the typical threshold for the onset of snow drift (Dery et al., 2002). Furthermore, data selection criteria a and b as defined before are applied. All constraints taken together, 425 data points remain for the determination of z_0 . When calculated by the equation 6.4 above, z_0 ranges from 10^{-6} to 10^{-4} m with a mean and median value of $8 \cdot 10^{-5}$ m and $6 \cdot 10^{-5}$ m respectively. Due to the large spread that does not offer a preferred value for z_0 this method seems not appropriate for the determination of a representative value for z_0 . One common way as used e.g. by van As et al. (2005) is to perform a linear fit of u_* against $U(z)$ according to equ. 6.3 under the mentioned data

selection criteria (e.g. van den Broeke et al., 2005):

$$u_* = a \cdot U(z) + b \quad (6.5)$$

The slope a from linear regression then defines as

$$a = \frac{\kappa}{\ln(z/z_0)} \quad (6.6)$$

which yields z_0 as

$$z_0 = z \cdot \exp\left(-\frac{\kappa}{a}\right). \quad (6.7)$$

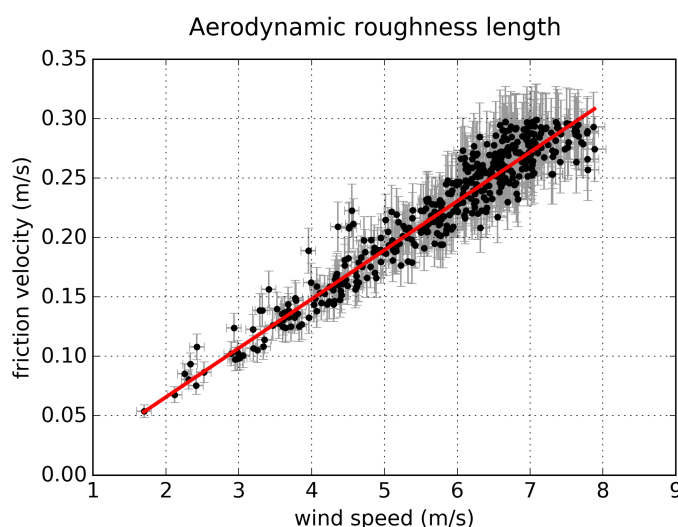


FIGURE 6.11: Aerodynamic roughness length z_0 is determined under near-neutral conditions via the slope of the linear regression of u_* against U at 1.9 m from Sonic data on a 15 min grid. For further constraints on data, see text.

We use a least-squares regression for the determination of the slope a which respects the errors of both U and u_* ("Orthogonal distance regression" in Python's Scipy module). As shown in section 5.3.5, the error of u_* is taken as $\pm 10\%$. The error of U is 2% but at least 0.1 m/s according to Sonic instrument specifications. By this method (see Fig. 6.11), we find z_0 to be $1.2 \cdot 10^{-4}$ m. If non-stationary conditions are not excluded much more data points enter the calculation, yielding a very similar z_0 of $1.2 \cdot 10^{-4}$ m. If the 2 m AWS wind speed is used for regression, the result is $1.0 \cdot 10^{-4}$ m. However, error considerations show that an error of 100% is easily reached which is confirmed by the previously mentioned large spread in magnitude of z_0 from equ. 6.4 (10^{-6} to 10^{-4} m for our data). The roughness length found by van As et al. (2005) is therefore plausible as well, especially considering our median z_0 value of $8 \cdot 10^{-5}$ m according to z_0 from equ. 6.4. From these considerations,

we define our local aerodynamic roughness length z_0 to be $1.2 \cdot 10^{-4} \text{ m} \pm 0.3 \cdot 10^{-4} \text{ m}$.

Over firm snow surfaces like at Kohnen where sastrugi are present, a clear dependence of z_0 on wind direction was found e.g. by Vignon et al. (2016) at Dome C. Sastrugi are carved by wind along the mean wind direction. For unusual wind directions the wind does not flow parallel but at an angle to the sastrugi, increasing the apparent surface roughness. Due to the large directional consistency of the wind this effect must be suspected for Kohnen too but cannot be investigated here because there is too little data left from other directions than the main wind direction under the constraint of an undisturbed fetch. Due to the proximity of the Sonic to the containers and disturbed fetch in the background, most of the data that could demonstrate a dependence on wind direction have been excluded for data quality reasons.

Well-known is the dependence of z_0 on wind speed (or on u_* analogously) for flat desert and snow areas (Garratt, 1992, sec. 4.1.2.). Snow crystals raise from the surface with increasing wind speed or friction velocity, which leads to an increase in surface roughness. Different u_* thresholds have been reported for the onset of snow drift but 0.3 m/s is a common value (as used here to exclude snow drift episodes for the determination of a constant z_0). Based on our data, we found z_0 to increase significantly with u_* (not shown here). Finding a functional dependence of z_0 on u_* though is subject to self-correlation, given a z_0 calculation according to equ. 6.4. Therefore, we will not attempt to find an explicit functional dependence. Additionally, we see from Fig. 6.11 that the ratio of $U(1.9\text{m})$ and u_* is approximately constant even with increasing wind speed. This behaviour justifies the assumption of z_0 to be a constant surface property, at least in neutral conditions and for u_* up to 0.3 m/s (due to data selection criteria here). Friction velocity u_* rarely exceeds this threshold during the campaign.

Neutral drag coefficient

From the definition of the drag coefficient C_D in equation 4.14 we see that

$$\sqrt{C_D} = \frac{u_*}{U} \quad (6.8)$$

Therefore, we determine the neutral drag coefficient C_{Dn} at measurement height under the same constraints as z_0 from the resulting slope a that was used to calculate z_0 :

$$C_{Dn} = a^2. \quad (6.9)$$

C_{Dn} is frequently needed in models for turbulent flux parametrization (see equ. 4.21). For this purpose, 10 m is the common reference height for C_{Dn} . This value is gained using

equ. 4.17 based on z_0 only. Table 6.2 summarizes the results.

Neutral bulk transfer coefficient for heat

Because the temperature roughness length z_{0t} is unknown, the bulk transfer coefficient for heat under neutral stratification C_{Hn} cannot be determined by equ. 4.18 but is estimated from the daily course of C_H . Each day, the lower atmosphere passes the state of neutral stratification twice. The lower panel in Fig. 6.12 shows the mean daily cycle of C_H during the measurement period as blue dots. Note that the steep decline and ascent in the morning and afternoon are due to measurement uncertainties in near-neutral conditions as explained in section 6.2.2. C_H values smaller than $0.5 \cdot 10^{-3}$ and larger than $2.0 \cdot 10^{-3}$ are unphysical. We estimate C_{Hn} as the mean of the mean C_H between 2100 and 0400 (stable period) and 0900 and 1500 (convective period). This $C_{Hn} = 1.1 \cdot 10^{-3}$ is indicated as a green horizontal line in both panels of Fig. 6.12. This number will serve for the determination of z_{0t} in the next paragraph. The corresponding C_{Hn} for the 10 m level is calculated by equ. 4.18, results are summarized in table 6.2.

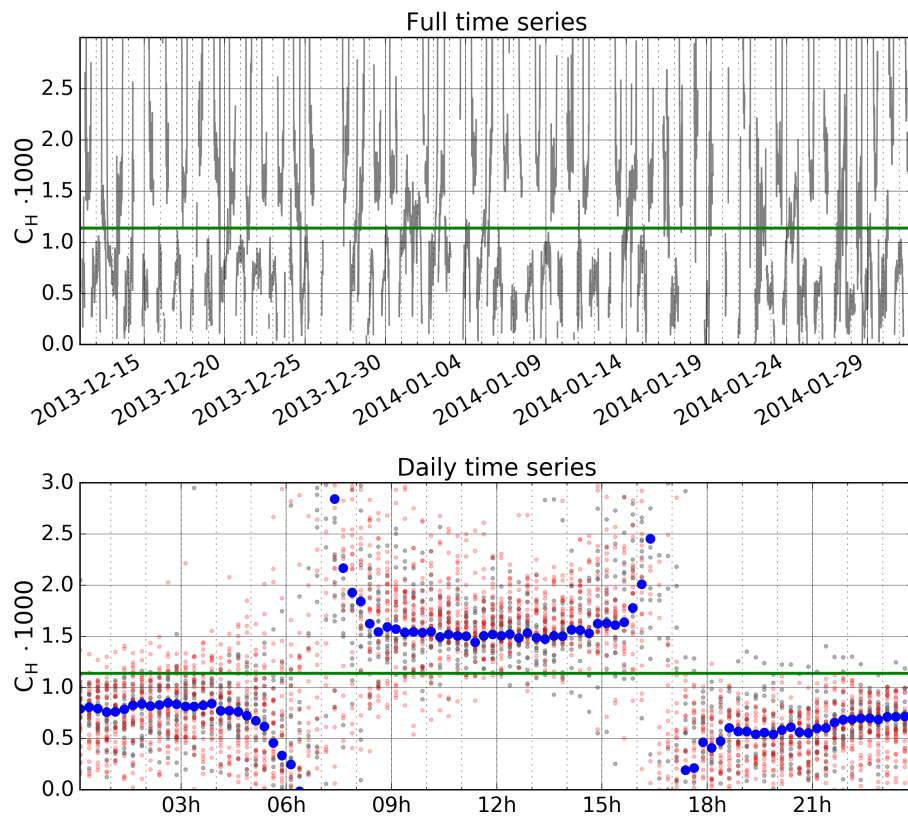


FIGURE 6.12: Full time series of measured bulk transfer coefficient for heat C_H (upper panel) and daily time series (lower panel) where blue dots signify mean C_H values on a 15 min grid, grey dots depict December days and red dots depict January days. C_H values $< 0.5 \cdot 10^{-3}$ and $> 2 \cdot 10^{-3}$ are most likely unphysical and due to uncertainty in longwave surface emissivity ε . The green horizontal line indicates the neutral C_H value, for method see text.

Temperature roughness length

The temperature roughness length z_{0t} cannot be determined by linear regression based on equ. 4.9 accordingly to z_0 derivation because $\theta_v(z) - \theta_0$ and θ_* are zero under neutral stratification. It is therefore calculated based on C_{Dn} and C_{Hn} by combining equ. 4.14, 4.15 and 4.10:

$$z_{0t} = z \cdot \exp \left[-\frac{\kappa \sqrt{C_{Dn}}}{C_{Hn}} \right] \quad (6.10)$$

which yields $z_{0t}=9.6 \cdot 10^{-7}$ m. This value will be considered the main z_{0t} in this study. Although it is so small, it is within the expected range because z_{0t} can be up to 4 orders of magnitude smaller than z_0 (Beljaars and Holstlag, 1991). There exist different models which derive z_{0t} based on z_0 . The frequently used one by Andreas (1987) yields $z_{0t}=1.35 \cdot 10^{-4}$ m. That model classifies the flow into three roughness regimes: smooth, transitional and rough. Our data are mainly in the transitional regime (98%) whereas in the study by van As et al. (2005), they lie half in the smooth, half in the transitional regime for Kohnen Station (ENABLE campaign, 7 Jan-11 Feb 2002). Again different values for z_{0t} are found if we consider errors in the estimated C_{Hn} value that is employed in equ. 6.10 or if we use the z_0 based on van As et al. (2005). Combining all these possibilities for z_{0t} calculation, we get a minimum z_{0t} of $1.3 \cdot 10^{-7}$ m (from $C_{Hn}=1.0 \cdot 10^{-3}$ and our C_{Dn}) and a maximum of $1.35 \cdot 10^{-4}$ m (from Andreas (1987) model using our z_0).

6.2.6 Parametrization of turbulent surface fluxes

For testing existing parametrizations in the form of ψ_M according to MOST we calculate ψ_M values based on our data by

$$\psi_M(\zeta) = \ln \left(\frac{z}{z_0} \right) - \frac{\kappa U(z)}{u_*} \quad (6.11)$$

(cf. equ. 4.9) which is a very simple and straight-forward method and which, to our knowledge, has not been used by others before. Commonly, MOST parametrizations are tested by using the dimensionless gradient form (see equ.4.7). But this method needs temperature and wind measurements from at least two levels and turbulence measurements from at least one level. The campaign data, however, only offer one measurement height for all these quantities, forcing us to employ the integrated form shown by equ. 6.11. For analysis, data selection criteria a and b are employed.

Figure 6.13 shows ψ_M values depicted against ζ at equal timestamps. This yields the visualization of the functional dependence $\psi_M(\zeta)$ at the location of Kohnen Station from our data. Since ζ is close to zero for most of the time, a logarithmic depiction has been chosen here in order to improve the representation of the majority of data points. In order to include all gained ψ_M values into one graph for a full interpretation of results, the scaling

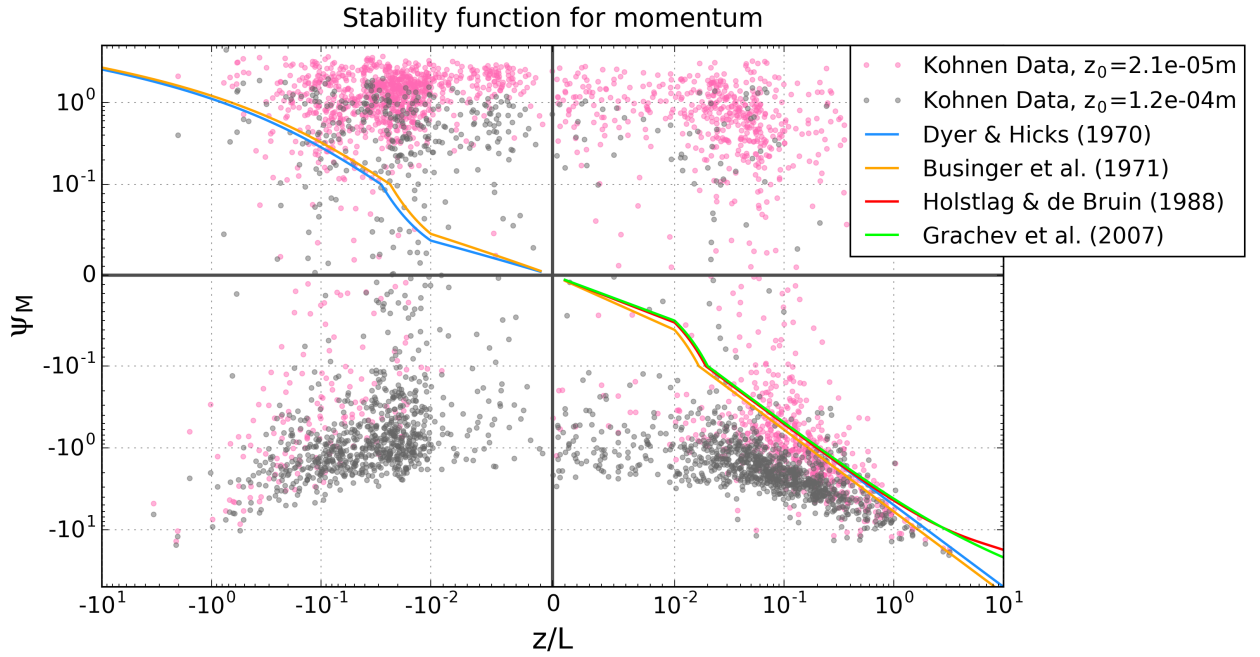


FIGURE 6.13: Values of ψ_M based on data, depicted against measured $\zeta = z/L$ for two different roughness lengths (our roughness length in grey, the one by van As et al. (2005) in pink). Please note that the scaling is logarithmic; but linear for $-10^{-2} < \zeta < 10^{-2}$ and $-10^{-1} < \psi_M < 10^{-1}$. Literature parametrizations according to MOST as named in the legend are explicitly given in appendix B.

for $-10^{-2} < \zeta < 10^{-2}$ and $-10^{-1} < \psi_M < 10^{-1}$ is linear though. This cannot be realized differently for an otherwise logarithmic diagram which shall switch sign at the axes. Due to this change in scale, the literature functions obtain an unusual appearance but on the other hand, the results are overall better depictable. For reference, the reader can find a fully linear plot for ψ_M vs. ζ in Fig. E.1 of the appendix.

What we find from Fig. 6.13 is that our measured ψ_M generally show a large scatter, causing many data points to be far off expectation from any of the available parametrizations, with ψ_M from both our determined z_0 (grey) and the value found by van As et al. (2005) (pink) for a location about 2 km away from the location of the present study. The slope of ψ_M in the stable regime ($z/L > 0$) agrees with expectation but this is not the case for the unstable regime ($z/L < 0$). The results for ψ_H (see Fig. 6.14) which is determined by

$$\psi_H(\zeta) = \ln\left(\frac{z}{z_{0t}}\right) - \frac{\kappa(\theta_v(z) - \theta_0)}{\theta_{v*}} \quad (6.12)$$

(cf. equ. 4.10) show a bad agreement with MOST prediction despite the careful data selection but on the other hand, they also scatter heavily. It was surprising that our ψ values apparently fit MOST so badly at first sight since the method for comparison is straightforward and van As et al. (2005) and van den Broeke et al. (2005) could demonstrate

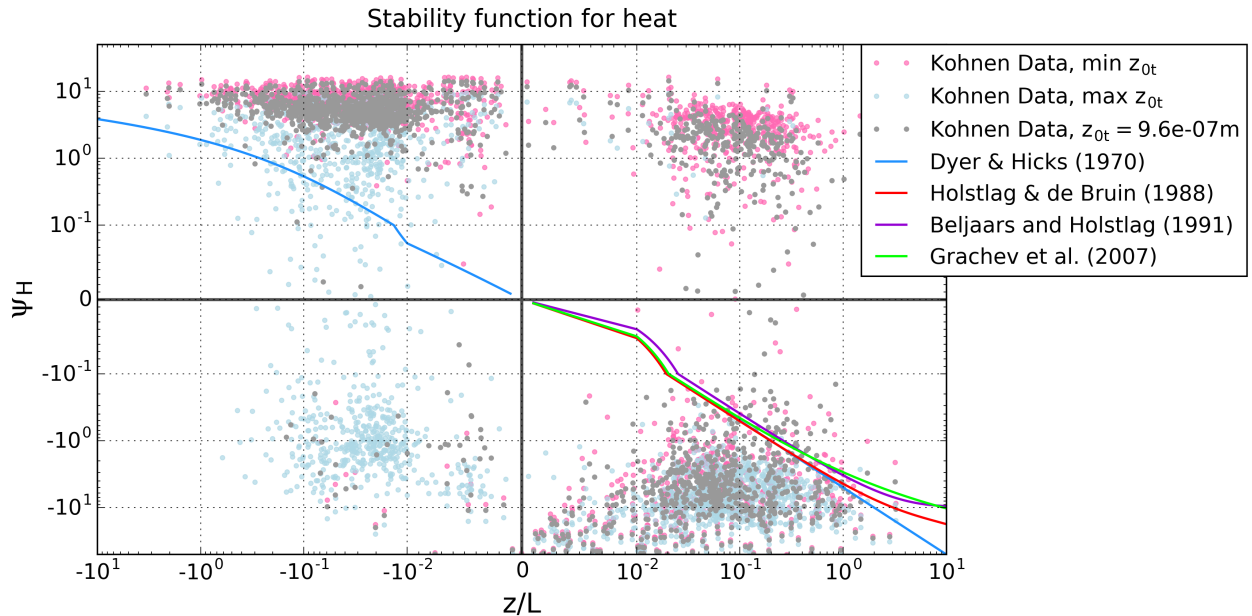


FIGURE 6.14: Values of ψ_H based on data, depicted against measured $\zeta = z/L$ for three different temperature roughness lengths (the main $z_{0t}=9.6\cdot 10^{-7}$ m in grey, minimum $z_{0t}=1.3\cdot 10^{-7}$ m (from $C_{Hn}=1.0\cdot 10^{-3}$ and our C_{Dn}) and maximum $z_{0t}=1.35\cdot 10^{-4}$ m (from Andreas (1987) model using our z_0). Please note that the scaling is logarithmic; but linear for $-10^{-2} < \zeta < 10^{-2}$ and $-10^{-1} < \psi_M < 10^{-1}$. Literature parametrizations according to MOST as named in the legend are explicitly given in appendix B.

an acceptable agreement between measured and calculated SHF at Kohnen based on the parametrizations by Holstlag and de Bruin (1988) (stable regime) and Dyer (1974) (unstable regime). Therefore, many tests have been performed to investigate the robustness of the resulting ψ values and the shape of their distribution. As a result, major changes appear as a vertical shift of the ψ values or as an increased scatter. The general behaviour, however, showed to be very robust. The following paragraphs summarize all tested influencing measures:

1) Changes in Sonic data processing:

- Use of a 30 min interval for rotation into streamline coordinates instead of 60 min, i.e. the wind components \bar{v} and \bar{w} are zero on 30 min intervals instead of 60 min (see section for Sonic data processing).
- Use of a Fast Fourier Transform additionally to linear detrending as a high-pass filter of the high-resolution Sonic data before flux computation. Applied after rotation into streamline coordinates on data intervals of 30 min duration. Two different frequency thresholds have been tested for this (see appendix C).

- Simplification of the processing routine: rotation into streamline coordinates, linear detrending and covariance (flux) calculation are performed on the same data block of 10 min duration (averaging length = 10 min) instead of using different interval lengths for these steps.

2) Variation of ζ :

- Use of $z=2$ m instead of 1.9 m.
- Use of Sonic temperature T and $\overline{T'w'}$ instead of the potential temperature θ and $\overline{\theta'w'}$ in the calculation of Obukhov length L that enters ψ_M via ζ .
- Computation of L using θ_* (equ. 4.4) instead of the more direct way as stated in the definition of L in equ. 4.8 (by simply inserting the definition of θ_*).

3) Variation of z_0 and z_{0t} :

- Increase and decrease z_0 by one order of magnitude.
- Use of a non-constant z_0 as a function of u_* (polynomial dependence from fitting z_0 to u_*). The resulting ψ_M looks even worse, it's barely dependent on ζ anymore.

4) Manipulation of u_* :

- Since the friction velocity u_* is larger than computed by van den Broeke et al. (2005), it is reduced by multiplication with 0.8. Roughness length z_0 then becomes of the order of 10^{-6} .
- Keeping the original z_0 while reducing u_* was tried as well.

5) Use of AWS data:

- Use the corrected temperature time series from the AWS at $z \approx 1.4$ m and the AWS wind speed ($z \approx 2$ m) for the calculation of ψ while setting $z=1.4$ m. Surface fluxes are considered to be approximately constant with height, so all turbulence quantities needed for ψ calculation can be assumed to equal those at AWS temperature height.

6) Post-calibration:

- In case the Sonic mean temperatures are erroneous, a simple calibration attempt (linear function) of fitting the Sonic temperature to AWS temperature is performed.

7) Second ψ term:

- Include the originally neglected $\psi_M(z_0/L)$ term into the depiction ($\psi_H(z_{0t}/L)$ accordingly). There is no noticeable difference in the results, again confirming the rightful neglect of this term.

After all these tests and considering the previously shown good agreement between Ri_B and ζ towards Grachev et al. (2007), the data in Figures 6.13 and 6.14 must be considered generally trustworthy under the assumption of correct measurements and constant roughness lengths and will now be discussed. First of all, data points are only expected to be located in the right lower and left upper quadrant in both graphs, otherwise they cannot be explained by MOST (if measurement uncertainties are neglected in this thought). From equ. 6.11 and 6.12 we see that ψ values only vary in dependence of ζ with changing U/u_* and $\Delta\theta/\theta_*$ respectively because the terms $\ln(z/z_0)$ (≈ 10) and $\ln(z/z_{0t})$ (≈ 15) are constant for constant surface properties z_0 and z_{0t} . Altering these surface properties can therefore only lead to a simple vertical shift of all measured ψ data points. This can be seen when comparing the location of data points calculated from our $z_0 = 1.2 \cdot 10^{-4}$ m (grey) to those based on $z_0 = 2.1 \cdot 10^{-5}$ m (pink) as found by van As et al. (2005) (easier to see in the linear depiction of ψ_M in Fig. E.1). The same is true for values of ψ_H depending on the choice of z_{0t} . Hence, the spread and slope cannot be influenced by the choice of (constant) z_0 and z_{0t} but only by the ratios of mean quantities and turbulent scales U/u_* and $\Delta\theta/\theta_*$. The latter also determine whether data points are located in the expected quadrants of the graph.

The following two paragraphs contain a description of the graphs under the assumption of correct measurements and constant roughness lengths.

Stable regime: From this analysis of the equations, we can reason that under stable stratification ($\zeta > 0$), there are cases where U/u_* and $\Delta\theta/\theta_*$ are too small against $\ln(z/z_0)$ and $\ln(z/z_{0t})$, respectively, causing data points to lie in the upper right quadrant of the graphs. A possible explanation is that the turbulent scales become too large against the mean quantities in these cases, caused by increased wind shear from above due to the occurrence of a very low night-time LLJ. Turbulence may also be increased by by-passing gravity waves while mean wind speeds and temperatures remain unaffected. Both phenomena do not go along with MOST. Values of ψ_H can also be influenced by possibly large measurement uncertainties in the vertical temperature difference due to uncertainty in longwave emissivity ε . In the lower right quadrant we see that turbulence parametrization by any stability function according to MOST would generally overestimate the turbulent scales u_* and θ_* (and thus the fluxes) when compared to our measurements. This contradicts the findings from van As et al. (2005) and van den Broeke et al. (2005) who found that the SHF would

be slightly underestimated in both the stable and unstable regime. However, it is consistent with the findings from Vignon et al. (2016) who come to the same conclusion after comparing measured dimensionless gradients ϕ_M and ϕ_H to four different MOST stability functions in the stable regime at Dome C. Comparing the ψ_M values from the two different roughness lengths, the smaller z_0 by van As et al. (2005) seems to yield a better agreement with MOST expectation (lower right quadrant) but many data points are shifted into the questionable upper right quadrant of the graph that does not obey MOST laws.

Unstable regime: Under unstable stratification ($\zeta < 0$), flux parametrization agrees worse with MOST than in the stable regime. Most of the data points for ψ_M as calculated by our z_0 are located in the lower quadrant, meaning that measured u_* (momentum flux) is too small against mean wind speed to be parametrized correctly by MOST. For the smaller number of data points in the upper quadrant, the opposite is the case and momentum flux parametrization by MOST would underestimate u_* . Interestingly, based on the roughness length from van As et al. (2005), the data distribute just oppositely, meaning that MOST would mainly underestimate the momentum flux. Concerning ψ_H , the SHF would mainly be underestimated since the majority of the measured ψ_H is in the upper quadrant for the full uncertainty range of z_{0t} . This is in accordance with van As et al. (2005). It should be mentioned here that especially in weakly stratified (both stable and unstable) air the uncertainty of θ_0 through ε can have a huge impact on ψ_H . Summarizing these findings for the unstable regime, momentum flux over- or underestimation by MOST highly depends on the choice of z_0 whereas the SHF would predominantly be underestimated in comparison to our measurements. Our turbulence measurements during the convective period may not obey MOST laws because radiosoundings showed that wind speed decreases with height in the lowest 8 metres almost every day during the campaign. On many days, this phenomenon also appears in the 0600 and 1800 profiles. We don't know how much this affects our measurements at 1.9 m height but measurements taken during an inversed or corrupted wind profile do not follow the assumptions of ABL theory and are thus no good choice to compare turbulent fluxes with flux parametrizations. Maybe this is why the results for ψ_M are inconclusive.

It should be mentioned that the overall scatter of ψ_M and ψ_H for small ζ can be particularly large because of increased measurement uncertainties of $\overline{\theta'w'}$ in near-neutral conditions (when $\overline{\theta'w'}$ becomes very small). Additionally, the assumption of a constant z_0 despite the large range of individually determined z_0 (10^{-4} to 10^{-6}) in near-neutral conditions probably leads to an increased scatter as well. ψ_M and ψ_H data points in questionable quadrants of the graphs can also be created by this increased scatter. The method itself may add an additional uncertainty.

Direct comparison of measured and parametrized friction velocity

For an easier comparison of measured and parametrized fluxes according to MOST, the bulk method as outlined in chapter 4 (equ. 4.21) is employed. As an example, we only choose momentum flux parametrization under stable stratification here. In order to visualize differences between two stability functions for the stable regime, friction velocity u_* (and thus momentum flux) is parametrized based on ψ_M by Grachev et al. (2007) (Fig. 6.15, left panel) and based on the one by Holstlag and R. (1988) (right panel) which is a very popular function for the stable regime. Additionally, we use two different roughness lengths z_0 : the one from our study (grey) and the one determined by van As et al. (2005) for the Kohnen area (pink). Apparently, the results do not differ with the choice of stability function. This is because the lowermost 2 m of the atmosphere do not become strongly stable during the measurement period. For winter measurements when ζ becomes larger, a difference between the two stability functions would become clearer (cf. Fig. E.1).

As described before from Fig. 6.13, the use of the smaller roughness length yields a seemingly better agreement between measured u_* and MOST. Just like before, the flux is overestimated by MOST for most of the u_* range if our larger z_0 is used for calculation. On the other hand, we see that an underestimation sets in under $z_0 = 2.1 \cdot 10^{-5}$ m for much smaller u_* than it is the case for our z_0 (for $u_* > 0.16$ m/s already instead of $u_* > 0.28$ m/s). When translated to percentages, the flux based on $z_0 = 2.1 \cdot 10^{-5}$ m is underestimated for 35% of the time compared to the measured data while under the use of $z_0 = 1.2 \cdot 10^{-4}$ m from our study, this is the case for 5% of the time. When calculating the percentages for the occurrence of $\psi_M > 0$ (right upper quadrant in Fig. E.1), the numbers are exactly the same. This confirms the previous interpretation that $\psi_M > 0$ occurs if u_* becomes too large against mean wind speed U in our data. Hence, the use of $z_0 = 2.1 \cdot 10^{-5}$ m yields a satisfying flux parametrization in contrast to $z_0 = 1.2 \cdot 10^{-4}$ m but only up to $u_* > 0.16$ m/s which is just slightly above the mean u_* for the measurement period. The more consistent behaviour under our $z_0 = 1.2 \cdot 10^{-4}$ m may hint at additional local effects that are not represented in MOST (such as the influence of radiation flux divergence). The use of $z_0 = 2.1 \cdot 10^{-5}$ m may therefore lead to an unsystematic error when used in models for Kohnen where these effects are included. Generally, the curvature of the scatter plot towards a flux underestimation for larger friction velocities may be due to an increase in z_0 for increasing wind speeds over the snow surface so that the assumption of a constant z_0 may not be justified anymore.

The picture under the use of the parametrization according to Louis (1979) (see Fig. 6.16) is very much similar to the graphs from the previous parametrizations. The difference of the Louis method does not only lie in the stability dependence of the drag coefficient. The particular difference lies in the use of Ri_B as stability parameter instead of ζ (which incorporates the measured u_* itself in the above figures). Consequently, the advantage against

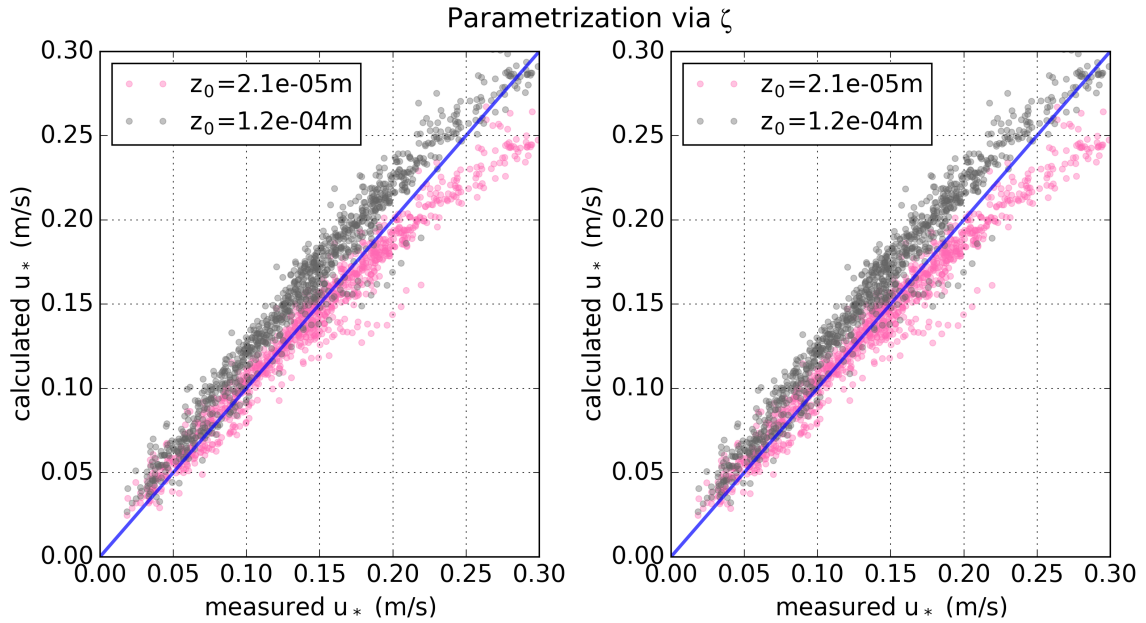


FIGURE 6.15: Friction velocity parametrization (momentum flux parametrization) in the stable regime based on the stability functions ψ_M by Grachev et al. (2007) (**left panel**) and Holstlag and R. (1988) (**right panel**).

the method above is that no turbulent quantities enter the parametrization calculation, eliminating the influence of self-correlation. For models, this is an advantage as well since no iterative solution is necessary if u_* is unknown. Instead, by the use of Ri_B , the turbulent fluxes can directly be determined based on the mean quantities. Except for z_0 , the result depicted in Fig. 6.16 is therefore analytically independent from the one in Fig. 6.15.

To summarize the influence of z_0 and z_{0t} on the results it should be underlined that a constant z_0 can only shift ψ_M and ψ_H vertically in the graphs 6.13 and 6.14. We can fathom that z_0 might change with time due to slightly altered surface conditions. A daily changing z_0 would most likely decrease the scatter for small $|\zeta|$ in Fig. 6.13 and 6.14 but it is not able to change the slope of the measured ψ_M (and ψ_H) curves in general. In order to do so, z_0 and z_{0t} would need to depend on ζ which has not been shown to be true yet and which would also contradict the idea of z_0 and z_{0t} to be surface properties that depend on physical surface roughness. Another result is that since z_0 of the order of 10^{-5} m seems to yield a better agreement of the fluxes with MOST predictions, our median and mean values for z_0 as determined by equ. 6.4 would lead to better results than the commonly determined z_0 from linear regression.

In conclusion, our initial straight-forward method for testing different MOST flux parametrizations (Figures 6.13 and 6.14) could give us some insight into potential difficulties for MOST application at Kohnen Station but it is not suitable for the comparison of different stability functions because the scatter due to uncertainties in roughness lengths and

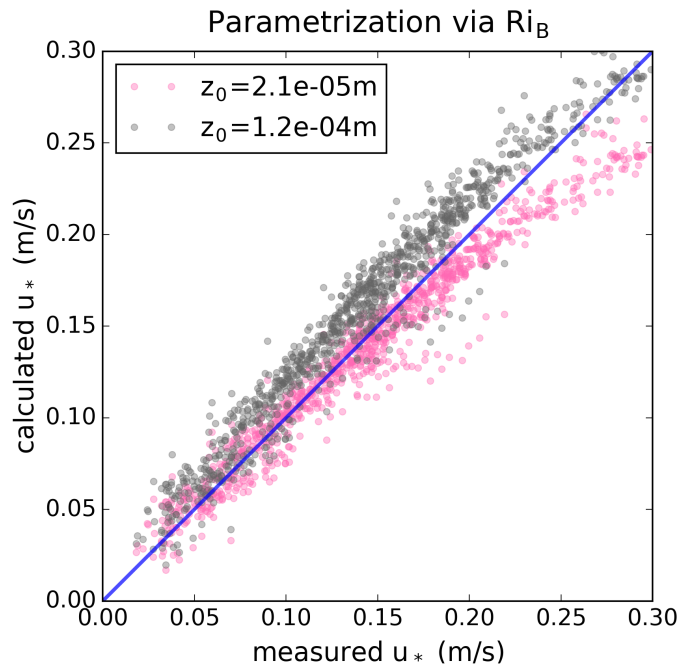


FIGURE 6.16: Friction velocity parametrization (momentum flux parametrization) in the stable regime based on Louis (1979) under the use of Ri_B instead of ζ as stability parameter.

surface temperature is too large. Other methods of directly comparing measured and calculated fluxes according to MOST are probably more suitable for this aim. Furthermore, stratification during the two summer months of the campaign did not become stable enough to reach ζ values where stability functions differ significantly. This generally complicates a comparison of different functions in this study. The method even seems to be only little useful for a general comparison with MOST predictions because measurement uncertainties impact this method a lot and uncertainties due to the method itself may increase the scatter of data points further. By using a direct comparison of measured and calculated fluxes as shown in the second part of the analysis, conclusions can be drawn easier.

Since MOST demands stationary conditions, episodes of too fast temperature change have been excluded from analysis. The results are therefore most likely unaffected by the diurnal cycle of temperature and wind speed at the site. Episodes of potentially counter-gradient fluxes have also been removed. This data selection excluded 54% of the available data from interpretation in order to meet MOST demands as best as possible. The agreement with MOST for momentum flux parametrization under stable stratification is finally not as bad as it seemed in the first part of the analysis but it is still not overall satisfying. For heat flux parametrization and for momentum flux parametrization in the unstable regime, the agreement between measured and parametrized fluxes according to MOST can probably be improved by altering surface roughness lengths, but it probably remains unsatisfying

in general. An overestimation of the fluxes by MOST parametrization would be in accordance with the study by Vignon et al. (2016) for Dome C. Under the assumption of correct measurements, the consequence of the analysis may be that the Kohnen area does not fulfill MOST requirements well, at least not generally. On the other hand, measurement uncertainties can distort this impression.

Possible explanations for a limited agreement with MOST predictions include that our measurement height may be already above the depth of the surface layer which must be considered to be very shallow at the site during stable stratification. Additionally, during stable stratification, the temperature profile in the lowest metres of the ABL may be influenced heavily by the divergence of radiative fluxes instead of being determined by turbulence only (cf. Garratt and Brost, 1981, Steeneveld et al., 2010). This would lead to smaller measured turbulent scales than predicted by MOST which is in accordance to our observations. During the convective period at each day, MOST laws may not be obeyed due to an inversed wind profile which occurs on a daily basis in the lowest metres but the radiosoundings only offer the initial surface value and a measurement at approx. 10 m height to judge this. Independent measurements with a larger vertical resolution are necessary to validate this phenomenon. Furthermore, the assumption of a constant roughness length z_0 and surface longwave emissivity ε may introduce an error.

TABLE 6.1: Monthly means of data from the Kohlen campaign from 10 Dec 2013 to 31 Jan 2014. Temperature at 1.4 m is measured by AWS (unventilated) and has been corrected by comparison to the Sonic temperature at 1.9 m height. Surface temperature T_0 is calculated by broadband longwave radiation based on a surface emissivity of 0.97. Wind speed U is measured by the Sonic, pressure p and relative humidity RH (unventilated) by the AWS (converted to values with respect to ice and corrected for doubtful values). Upward and downward longwave radiation LW_{\uparrow} and LW_{\downarrow} by ventilated broadband pyrgeometers, cloud fraction CF by human observations and turbulence measurements performed by sonic anemometer-thermometer by Metek GmbH based on self-written processing software of the raw data.

Quantity (unit)	Dec 2013 mean (std) [daytime mean; nighttime mean]	Jan 2014 mean (std) [daytime mean; nighttime mean]
$T_{1.4m}$ ($^{\circ}\text{C}$)	-23.8 (4.1)	-25.9 (5.8)
$T_{1.9m}$ ($^{\circ}\text{C}$)	-24.0 (3.9)	-26.1 (5.6)
T_0 ($^{\circ}\text{C}$)	-24.7 (5.0)	-26.8 (6.5)
$U_{1.9m}$ (m/s)	4.69 (1.88)	3.78 (1.75)
p (hPa)	679 (3)	682 (4)
RH (%)	88.4 (6.7)	90.8 (6.4)
LW_{\uparrow} (W/m^2)	-215 (17)	-208 (22)
LW_{\downarrow} (W/m^2)	149 (26)	145 (27)
CF (1/8)	3.7 (3.1)	3.8 (3.2)
u_* (m/s)	0.18 (0.0085)	0.15 (0.077)
M (N/m^2)	-0.037 (0.033)	-0.026 (0.025)
C_D	0.0013 (0.00037)	0.0013 (0.00048)
ζ	0.06 (0.27) [-0.053; 0.17]	0.11 (0.37) [-0.057; 0.27]
Ri_B	0.01 (0.03) [-0.003; 0.02]	0.02 (0.04) [-0.004; 0.04]
$\theta_{1.4m} - \theta_0$ (K)	0.9 (2.0) [-0.6; 2.4]	1.1 (2.0) [-0.5; 2.6]
θ_* (K)	0.001 (0.056) [-0.044; 0.046]	0.005 (0.055) [-0.040; 0.048]
$\overline{\theta'w'}$ ($\text{K}\cdot\text{m}/\text{s}$)	0.0016 (0.0098) [0.0093; -0.0060]	0.0009 (0.0086) [0.0074; -0.0054]
H (W/m^2)	1.5 (9.4) [8.8; -5.8]	0.8 (8.4) [7.1; -5.3]
C_H	0.0012 (0.00072)	0.0012 (0.00080)
TKE (J/kg)	0.25 (0.22)	0.17 (0.16)

TABLE 6.2: Neutral bulk transfer coefficients for momentum C_{Dn} and heat C_{Hn} at measurement height $z=1.9$ m and at $z=10$ m (transformed via equ. 4.17 and 4.18); ⁽¹⁾: value based on previously determined $z_0 = 1.2 \cdot 10^{-4}$ m; ⁽²⁾: value based on $z_0 = 2.1 \cdot 10^{-5}$ m from van As et al. (2005).

	$z=1.9$ m	$z=10$ m
C_{Dn}	$1.7 \cdot 10^{-3}$ ⁽¹⁾ ; $1.2 \cdot 10^{-3}$ ⁽²⁾	$1.2 \cdot 10^{-3}$ ⁽¹⁾ ; $0.9 \cdot 10^{-3}$ ⁽²⁾
C_{Hn}	$1.1 \cdot 10^{-3}$ ⁽¹⁾ (estimated from C_H time series); $1.1 \cdot 10^{-3}$ ⁽²⁾ (calculated)	$0.9 \cdot 10^{-3}$ ⁽¹⁾ ($0.8 \cdot 10^{-3}$ to $1.2 \cdot 10^{-3}$ for z_{0t} error margin) $0.9 \cdot 10^{-3}$ ⁽²⁾ ($0.8 \cdot 10^{-3}$ to $0.9 \cdot 10^{-3}$ for z_{0t} error margin)
$\frac{C_{Dn}}{C_{Hn}}$	1.5 ⁽¹⁾ ; 1.0 ⁽²⁾	1.4 ⁽¹⁾ ; 1.1 ⁽²⁾

CHAPTER 7

Conclusion

In the present study, continuous turbulence measurements over the slightly sloping undisturbed and flat terrain of Kohnen Station (Dronning Maud Land), on the high inland Antarctic ice plateau have been analysed. It is the second ever available in-situ turbulence data set from this location. The study followed two main ideas: (I) a description of the meteorological situation at the site for the period from 10 Dec 2013 to 31 Jan 2014, including boundary layer evolution and (II) testing different flux parametrizations according to Monin-Obukhov similarity theory (*MOST*) for the surface layer, based on eddy-covariance measurements of turbulent momentum and sensible heat flux (*SHF*) performed by a sonic anemometer-thermometer (*Sonic*) in 1.9 m height. This has never been done before in such detail for the location of Kohnen Station.

We observe a strong diurnal cycle in near-surface temperature, wind speed and relative humidity as is typical for plateau stations during summer time. The mean wind direction was downslope from 49° with a large directional constancy of 0.90 although nighttime winds in general were slightly more easterly than during daytime. Wind and temperature conditions within the lower 2 m of the atmosphere were typical compared to long-term observations at the site except for relatively low wind speeds in January. The mean temperature was -25°C with a common day-night amplitude of about 10 K. Towards the end of January temperatures decreased significantly (down to nighttime values of -40°C) because of the approaching winter season which starts in February. The mean wind speed was 4.2 m/s while daytime wind speeds are generally larger than at night. The 10 min wind speed barely exceeded a value of 10 m/s since pressure systems on the synoptic scale penetrate the highly-elevated plateau very seldomly. Precipitation was mainly in the form

of ice crystal precipitation with no noteworthy snow accumulation during the measurement period. Cloud cover is generally low at the site. The typical nighttime temperature decrease showed to be heavily disturbed under the presence of low level clouds. We observed a so-called summer warming event in the night from 26th to 27th December 2013 when near-surface winds blew from an unusual north-western direction, bringing along relatively moist air from the coast and consequently leading to an completely overcast sky by low level clouds that suppress the nighttime temperature minimum completely. Ground fog and light snowfall were also observed during that event.

Due to the radiative forcing from the ground, the lower boundary layer is subject to a strong diurnal cycle as is typical to continental areas with stable stratification and downward SHF during the night and unstable stratification with upward SHF during the day. However, the boundary layer at Kohnen (and on the plateau in general) is very shallow with daytime mixing heights of typically 50-200 m and a surface-based temperature inversion of typically 30-80 m depth at midnight during the period of the campaign. Within the lowest 1.4 m, the mean nighttime temperature difference was 2.5 K. In many nights, a low level jet (*LLJ*) was observed while the level of the maximum wind speed typically varied between 30 and 200 m. Due to the strong radiative cooling at nighttime, the LLJ is most likely katabatically driven but it may be supported by inertial oscillations some cases of which may have been captured in the daily radiosounding profiles. Stable stratification in the lowermost 2 m dominated even during the summer campaign with mean bulk Richardson numbers of 0.01 in December and 0.02 in January (and nighttime means of 0.02 and 0.04 respectively). Mean SHF, however, was directed upwards, decreasing from +1.5 W/m² in December to +0.8 W/m² in January with a mean daily cycle between +15 and -10 W/m². This behaviour is typical for the surface layer at the site during summer. Friction velocity is 0.16 m/s on average with typical values of up to 0.3 m/s while the daily cycle follows the one of the near-surface wind speed, meaning it is largest during the day with a steep decrease after 1500 UTC.

For the second main focus of this study, i.e. the application of MOST, a careful data selection has been employed which lead to a data loss of more than 50%. This included e.g. the elimination of strongly non-stationary conditions in order to choose only those data that fulfill the conditions assumed in MOST in the best possible way in order to reduce the scatter of results as much as possible and draw trustworthy conclusions. The comparison of the dependence of measured stability parameters ζ on Ri_B to the study by Grachev et al. (2007) was very good. They developed stability functions for flux parametrization for stable stratification over uniform Arctic pack ice based on 11 months of data (the SHEBA dataset). The good agreement of ζ vs. Ri_B to their study suggests that their stability functions are also suitable for the location of Kohnen. For testing different stability functions

under MOST, a straight-forward and, to our knowledge, not yet employed method has been tried which only needs one measurement level for turbulent fluxes, wind speed and temperature. Usually, two levels of temperature and wind speed measurements are employed to test the parametrizations in their gradient form but since there are only single-level data available from the campaign, we were forced to find an alternative. The application of MOST on our data requires the determination of the aerodynamic roughness length z_0 and the temperature roughness length z_{0t} . Both showed to be hard to find a constant value for, maybe due to an increase of surface roughness with wind speed over the snow surface or a dependence on wind direction (via sastrugi orientation). We find z_0 from individual days to range between 10^{-6} to 10^{-4} m with a mean and median value of $8 \cdot 10^{-5}$ m and $6 \cdot 10^{-5}$ m, respectively. A different method based on linear regression yields $1.2 \cdot 10^{-4} \text{ m} \pm 0.3 \cdot 10^{-4} \text{ m}$. Since the determination of z_{0t} depends on z_0 , we find it to be $z_{0t} = 9.6 \cdot 10^{-7} \text{ m}$ with a large error margin between $1.3 \cdot 10^{-7} \text{ m}$ and $1.35 \cdot 10^{-4} \text{ m}$. The latter is the z_{0t} value determined based on the model by Andreas (1987). The scatter of neutral bulk transfer coefficients is therefore large as well. C_{Dn} ($z=10$ m) lies between 0.9 and $1.2 \cdot 10^{-3}$, C_{Hn} between 0.8 and $1.2 \cdot 10^{-3}$.

Values for the stability functions in their integrated form ψ_M and ψ_H have been determined based on our measurements via the profile functions for wind speed and temperature of MOST. They have been depicted against the stability parameter ζ together with different functions for ψ_M and ψ_H from literature. By this way, we hoped to compare different literature parametrizations to our data and find which stability function fits the Kohnen data and conditions best. However, we found that the method is not suitable for the comparison of different functions because (I) stability during the (summer) campaign does not reach a strength where parametrizations differ significantly from one another and (II) the scatter due to measurement uncertainties or the method itself is too large, in particular concerning roughness lengths z_0 and z_{0t} . The large scatter of measured ψ_M and ψ_H data points showed the method only little helpful for the use of comparison to MOST predictions at all. The method could be tested in the future based on other data sets which popular parametrizations have been developed for (e.g. SHEBA or Kansas data) to see whether our problems relate to the method itself or mainly to measurement uncertainties. Under stable conditions, the slope of our ψ_M data points for momentum flux parametrization, however, seemed somewhat promising, encouraging us to use a bulk method for a direct comparison of predicted friction velocity u_* according to three different parametrizations against measured values of u_* . This comparison shows that the data in fact agree well with MOST prediction under the stable regime if a z_0 of the order of 10^{-5} m is used although a slight underestimation of momentum flux sets in for $u_* > 0.16$ m/s. In the only other study that compares measured fluxes at Kohnen to parametrized fluxes, van As et al. (2005) also found a slight underestimation, but they only investigated the SHF. If z_0 from this study

is employed, momentum flux in the stable regime is slightly overestimated for almost the full u_* range which would agree with the findings in the study by Vignon et al. (2016). They found that heat and momentum fluxes under stable stratification are generally overestimated at Dome C when parametrized according to MOST. Possible reasons why the local conditions at Kohnen Station may not fulfill well the requirements of MOST include the influence of katabatic winds, the occurrence of LLJs at very low heights (*observed*), by-passing gravity waves (*not investigated*) or a potentially corrupted wind profile in the lower 10 m that does not satisfy theoretical assumptions and should be investigated further (*observed in radiosoundings*). A future campaign could employ two measurement levels on a mast. Additionally, a tethered balloon could be used for a better vertical resolution of wind speed and temperature within the lowermost metres and in order to gain an independent data set.

A further result of the study is that the measured bulk transfer coefficient for heat C_H showed to be very sensitive to the choice of surface longwave emissivity ε which is used in surface temperature calculation from broadband longwave radiation. We observed periods of different sign of kinematic heat flux $\overline{\theta'w'}$ and vertical temperature difference $\theta_0 - \theta_{air}$ that are due to measurement uncertainties in $\overline{\theta'w'}$ (when it becomes very small during near-neutral conditions that occur twice a day) and uncertainties in $\theta_0 - \theta_{air}$. The latter is known to be particularly influenced by uncertainties in surface temperature. Not only the C_H values differed significantly with slight variations of ε but also the duration of these artificially created periods of counter-gradient fluxes varied with the choice of ε . We conclude that the temporal variability of ε introduces a significant measurement error for surface temperature if a constant ε is assumed. We found $\varepsilon=0.97$ to be a reasonable choice for the site in order to receive reasonable C_H values while minimizing the duration of the artificial episodes of counter-gradient fluxes.

Another result is that measured momentum and heat fluxes showed to depend on the choice of averaging length in the flux calculation procedure from Sonic data (eddy-covariance method). Under stable stratification a much smaller averaging length is needed (5 min) to optimize data quality than under unstable stratification (30 min). Using a constant averaging length in between these values automatically introduces an uncertainty to the measured fluxes that we estimated to be about 10%.

At last, another outcome of this study is a processing script suitable for calculating turbulence quantities from raw Sonic measurements (i.e. runtimes of the signal between the sensors of the instrument) which can process many days of Sonic measurements at once. It is written in Python and can be used flexibly for data processing of upcoming campaigns.

The advantage of raw data processing against using the internal software of the instrument is the possibility of choosing an averaging length for flux calculation after the campaign instead of fixing it beforehand. This way, an averaging length can be chosen that maximizes the quality of the measured fluxes because the optimal averaging length depends on stratification and therefore on the individual conditions at the measurement location. In the obtained processing script, the time interval for rotation into streamline coordinates in order to compensate for tilt of the measurement mast can also be chosen freely and therefore does not need to equal the averaging length. Furthermore, using raw Sonic data processing, it is possible to perform measures of quality control directly on the raw sonic travel times between the Sonic sensors instead of removing doubtful fluxes afterwards based on threshold methods. The probability of eliminating turbulent bursts, because they are mistaken for outliers, is therefore reduced which is of particular importance for stable boundary layers where turbulence is generally small.

APPENDIX A

Derivation of wind speed and temperature from sonic travel times

A.1 Derivation of wind speed from sonic travel times

The shown derivation is an enhancement of the derivation in the Kaijo Denki Co. (1995) manual. The travel time t of a sound pulse from one sensor head to the other along the path length L is dependent on wind speed v (wind component in direction of L). Additionally, the effect of some scalar quantity on speed of sound is denoted α so that the travel speed of the sound pulse c can be displayed as $c = c_0 + v + \alpha$ where c_0 is the speed of sound in calm air and without the influence of the scalar quantity. For simplicity, we can imagine $v > 0$ in direction parallelly upwards along the measurement path. The sonic travel times t_u (upwards the path) and t_d (downwards the path) as measured by the device can therefore be expressed as

$$t_u = \frac{L}{c_0 + v + \alpha} \quad \text{and} \quad t_d = \frac{L}{c_0 + \alpha - v} \quad (\text{A.1})$$

$$\Leftrightarrow c_0 + v + \alpha = \frac{L}{t_u} \quad \text{and} \quad c_0 + \alpha - v = \frac{L}{t_d} \quad (\text{A.2})$$

Solving for c_0 and combining the left and right equation results in

$$\Leftrightarrow \frac{L}{t_u} - v = \frac{L}{t_d} + v \quad (\text{A.3})$$

We see that v is independent of c_0 and α , if c_0 and α are constant during the time it takes the signal to run up and down the path.

$$\Leftrightarrow 2v = \frac{L}{t_u} - \frac{L}{t_d} \quad (\text{A.4})$$

$$\Leftrightarrow v = \frac{L}{2} \left(\frac{1}{t_u} - \frac{1}{t_d} \right) \quad (\text{A.5})$$

When projecting the 3D wind vector onto the three measurement paths of the instrument, each of the projected wind components can be calculated by equ. A.5. Therefore, six sensor heads (three independent measurement paths) are needed to conclude the 3D wind vector.

A.2 Derivation of temperature from sonic travel times

Reproduced from the manual by Kaijo Denki Co. (1995). The starting point is the same as in the previous one:

$$t_u = \frac{L}{c_0 + v + \alpha} \quad \text{and} \quad t_d = \frac{L}{c_0 + \alpha - v} \quad (\text{A.6})$$

Solving for v and then joining both equations cancels v while this time, c_0 and α remain.

$$\Leftrightarrow \frac{L}{t_u} - c_0 - \alpha = -\frac{L}{t_d} + c_0 + \alpha \quad (\text{A.7})$$

$c_0 + \alpha$ is the current speed of sound, denoted as C from here on, which includes scalar dependencies (α) such as temperature.

$$\Leftrightarrow \frac{L}{t_u} - C = -\frac{L}{t_d} + C \quad (\text{A.8})$$

$$\Leftrightarrow 2C = \left(\frac{L}{t_u} + \frac{L}{t_d} \right) \quad (\text{A.9})$$

$$\Leftrightarrow C = \frac{1}{2} \left(\frac{L}{t_u} + \frac{L}{t_d} \right) \quad (\text{A.10})$$

APPENDIX B

Stability functions according to MOST

Stability functions

in the following we use $\zeta = z/L$.

For stable stratification

Holtslag and De Bruin (1988)

$$\psi_m = -a \zeta - b \left(\zeta - \frac{c}{d} \right) \exp(-d \zeta) - \frac{bc}{d} \quad (\text{B.1})$$

$$\psi_h = \psi_m \quad (\text{B.2})$$

$a = 0.7, b = 0.75, c = 5, d = 0.35$

developped for $\zeta \geq 5$, proven for up to $\zeta = 7 \dots 10$ using Cabauw wind profiles.

Beljaars and Holtslag (1991)

is a revision of Holstlag-DeBruin.

$$\psi_m = -a \zeta - b \left(\zeta - \frac{c}{d} \right) \exp(-d \zeta) - \frac{bc}{d} \quad (\text{B.3})$$

$$\psi_h = - \left(1 + \frac{2}{3} a \zeta \right)^{1.5} - b \left(\zeta - \frac{c}{d} \right) \exp(-d \zeta) - \frac{bc}{d} + 1 \quad (\text{B.4})$$

$a = 1, b = 0.667, c = 5, d = 0.35$

ψ_m is the same as the Holtslag and De Bruin Function.

Dyer-Businger (Dyer 1974; Dyer and Hicks (1970); Businger et al. 1971)

The equations of Businger use different parameters and are based on $\kappa = 0.35$, but are of the same form as Dyer. Dyer equations are based on $\kappa = 0.41$. Högström (1988) modified both for $\kappa = 0.40$. Nevertheless, Dyer equations are commonly used with the old parameters together with $\kappa = 0.40$ (which is not really correct but established).

$$\psi_m = -5 \zeta \quad (\text{B.5})$$

$$\psi_h = -5 \zeta \quad (\text{B.6})$$

Businger et al. (1971), as modified by Högström (1988)

$$\psi_m = -6 \zeta \quad (\text{B.7})$$

$$(\text{B.8})$$

Grachev et al. (2007)

$$\psi_m = -\frac{3a_m}{b_m}(x-1) + \frac{a_mB_m}{2b_m} \cdot \left[2 \ln \frac{x+B_m}{1+B_m} - \ln \frac{x^2-xB_m+B_m^2}{1-B_m+B_m^2} + 2\sqrt{3} \left(\arctan \frac{2x-B_m}{\sqrt{3}B_m} - \arctan \frac{2-B_m}{\sqrt{3}B_m} \right) \right]$$

where $x = (1 + \zeta)^{1/3}$, $B_m = \left(\frac{1-b_m}{b_m} \right)^{1/3} > 0$, $a_m = 5$, $b_m = a_m/6.5$

$$(\text{B.9})$$

$$\psi_h = -\frac{b_h}{2} \ln (1 + c_h \zeta + \zeta^2) + \left(-\frac{a_h}{B_h} + \frac{b_h c_h}{2B_h} \right) \cdot \left(\ln \frac{2\zeta + c_h - B_h}{2\zeta + c_h + B_h} - \ln \frac{c_h - B_h}{c_h + B_h} \right)$$

where $B_h = \sqrt{c_h^2 - 4} = \sqrt{5}$, $a_h = b_h = 5$, $c_h = 3$

$$(\text{B.10})$$

For unstable stratification

Dyer-Businger (Dyer 1974; Dyer and Hicks (1970); Businger et al. 1971)

The equations of Businger use different parameters and are based on $\kappa = 0.35$, but are of the same form as Dyer. Dyer equations are based on $\kappa = 0.41$. Högström (1988) modified both for $\kappa = 0.40$. Nevertheless, Dyer equations are commonly used with the old parameters together with $\kappa = 0.40$ (which is not really correct but established).

$$\psi_m = \ln \left[\frac{1+x^2}{2} \cdot \left(\frac{1+x}{2} \right)^2 \right] - 2 \arctan x + \frac{\pi}{2} \quad (\text{B.11})$$

$$\text{where } x = (1 - 16 \zeta)^{1/4} \quad (\text{B.12})$$

$$\psi_h = 2 \ln \frac{1+x}{2} \quad (\text{B.13})$$

$$\text{where } x = (1 - 16 \zeta)^{1/2} \quad (\text{B.14})$$

APPENDIX C

Test of different filter frequencies for FFT (Sonic high-pass filter)

In an earlier version of the Sonic raw data processing, high-pass filtering was done using a Fast Fourier Transform in combination with detrending on the block of data corresponding to one averaging length (the time interval of data where the covariance is calculated). Low frequencies are filtered away but it must be assumed that the choice of threshold frequency (here "filter frequency") has an impact on the flux results. Therefore, the following investigation was made and shall be mentioned here.

In order to get an estimate about the impact of the chosen filter frequency on heat fluxes, momentum fluxes and TKE, data have been processed for one month (Dec 27 to Jan 26) using two different filter frequencies: one corresponding to a wave periodic time of 15 minutes, the other corresponding to a periodic time of 30 minutes. Moreover, two different averaging intervals were employed: 15 minutes and 5 minutes. A more complete study is not conducted here because results from these four parameter combinations are meaningful already in order to estimate the impact of the filter frequency.

The main question is whether any systematic change in fluxes can be observed for changing filter frequencies. To answer this question, the relative difference in percent is used as the critical quantity for comparison. It is calculated for every flux time step by

$$RD = \frac{|F_{f_1}| - |F_{f_2}|}{|F_{f_1}|} \cdot 100\% \quad (C.1)$$

where F is the heat flux, momentum flux or TKE, f_1 signifies the results gained by 15 minutes periodic time employed in the high-pass filter and f_2 the ones for 30 minutes periodic time. $RD < 0$ means that f_2 created larger results F while $RD > 0$ means that f_1 created

larger results.

In the following, the findings for the heat flux impact are described, summarized for both employed averaging intervals. More than 88% of the analysed data lie within an RD range of $\pm 10\%$. Differences due to a change in filter frequency that lie within this interval are considered not significant since the assumed error for the heat flux is of the same order (concerning common heat flux values of about $\pm 10 \text{ W/m}^2$). The mean and median RD value within this error interval are negligibly close to zero, meaning that none of the tested periodic times creates any significant increase or decrease in heat flux over the other. For the max. 11% of data points outside this $\pm 10\%$ interval, we see that about two third of them belong to heat fluxes below 1 W/m^2 in absolute value, that means the largest differences created by the different filter frequencies occur at neutral thermal stratification, when the covariances between filtered temperature and vertical wind component are very close to zero and therefore most sensitive to small changes. Larger differences must be expected for this case since the 30 minutes periodic time for filter leaves in more waves in the data stream and thus can influence such negligibly small covariances easily. In max. 1% of the analysed data, the heat flux switches its sign due to the use of different filter frequencies. But this only occurs during neutral stratification. These cases of changing sign have been neglected for this analysis, so that RD can be used for a clear statement. Overall, 4.3% of the analysed data show differences outside the $\pm 10\%$ interval that cannot be explained by neutral stratification insecurities. Looking at this more closely, we see that the 30 minutes periodic time enlarges the positive and negative maxima in heat flux significantly against the 15 minutes periodic time but on the other hand, the larger part of the data apart from the maxima show significantly larger heat fluxes for 15 minutes periodic time. For these 4.3% of the data, no statement about systematic heat flux changes depending on filter frequency can thus be made, just like for the rest of the analysed month of data. The same conclusion holds for the momentum flux without explaining the details here. In conclusion, this little test on filter frequencies showed that they do influence the flux results, but only to a non-systematic extent mostly within the results' error bars. There may be systematic differences between day and night but the same filter frequency shall be used for all data. Therefore, this will not be investigated here.

The TKE is mostly larger based on a 30 minutes periodic time for high-pass filter with a mean RD of -7 to -2% (while neglecting RDs smaller than -100%). This can easily be explained because the TKE is the sum of the wind components' variances, which increase if the data stream is allowed to keep more low-frequency waves. For all main output quantities, namely heat and momentum flux, drag coefficient, friction velocity and TKE (without including Obukhov length in this comparison), the 30 minutes periodic time for filtering

seems to increase the relative maxima in the quantities' time series. At the same time, it creates some new very narrow relative maxima that look like artefacts. Since no general systematic advantage of the 30 min periodic time could be found for the fluxes, we decide for using the smaller (15 minutes) periodic time for filtering away the low frequencies from the Sonic wind and temperature data.

APPENDIX D

Time series graphs

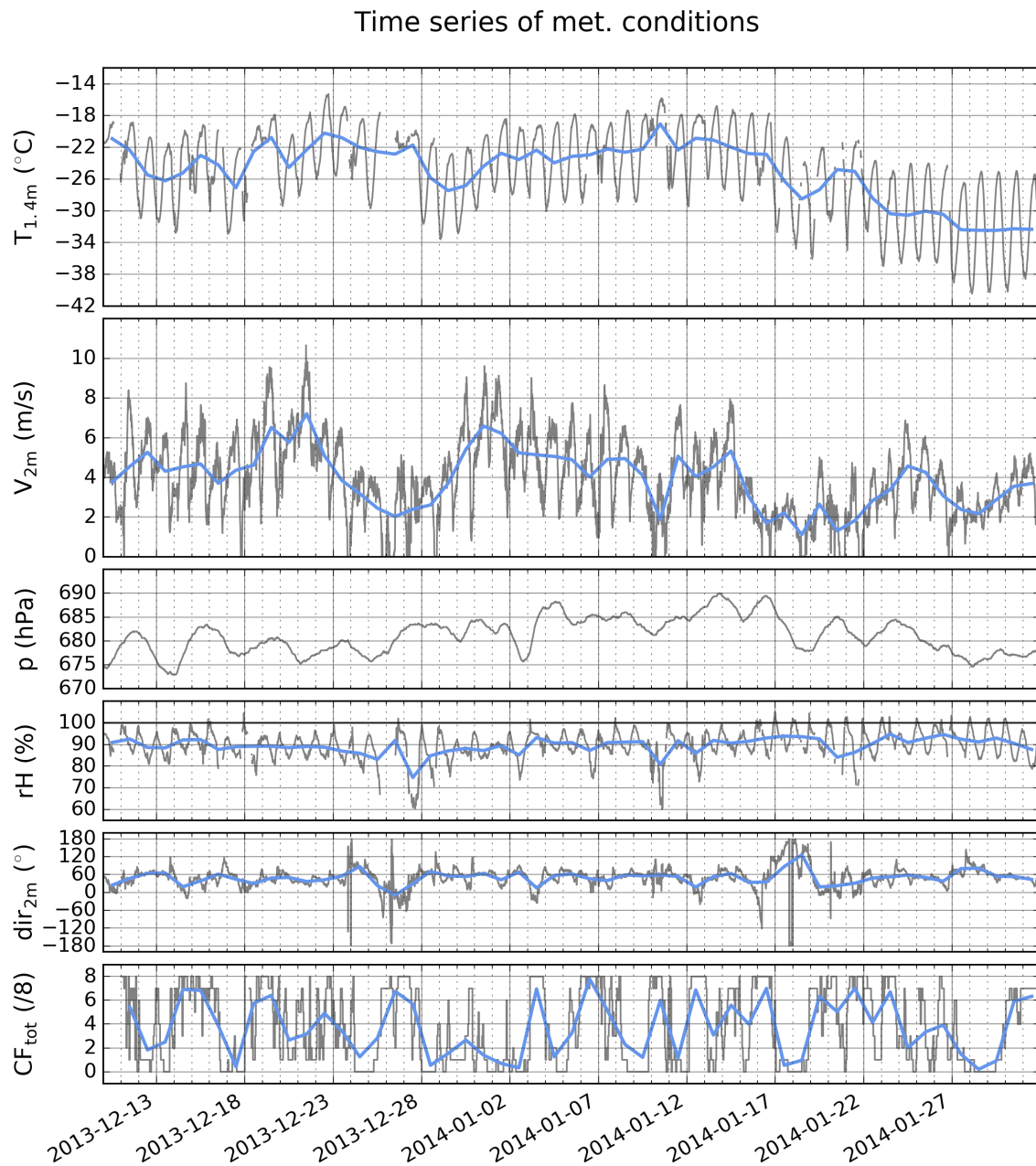


FIGURE D.1: Time series of main meteorological quantities as measured by the AWS from 13 December 2013 to 31 January 2014: 10 minute averages of temperature (T) at 1.4 m height, wind speed (ws) at 2 m height, pressure (p, minutewise), relative humidity (rH) with respect to ice at 1.4 m height (measurements with respect to water) and wind direction (wd) at 2 m height (0° from north, 90° from east, $\pm 180^\circ$ from south, -90° from west). Total cloud fraction CF from observation by eye. Daily means indicated as blue lines. Doubtful values for temperatures and relative humidity left out based on comparison to Sonic temperature (see text) because radiation shield that housed both sensors was not ventilated.

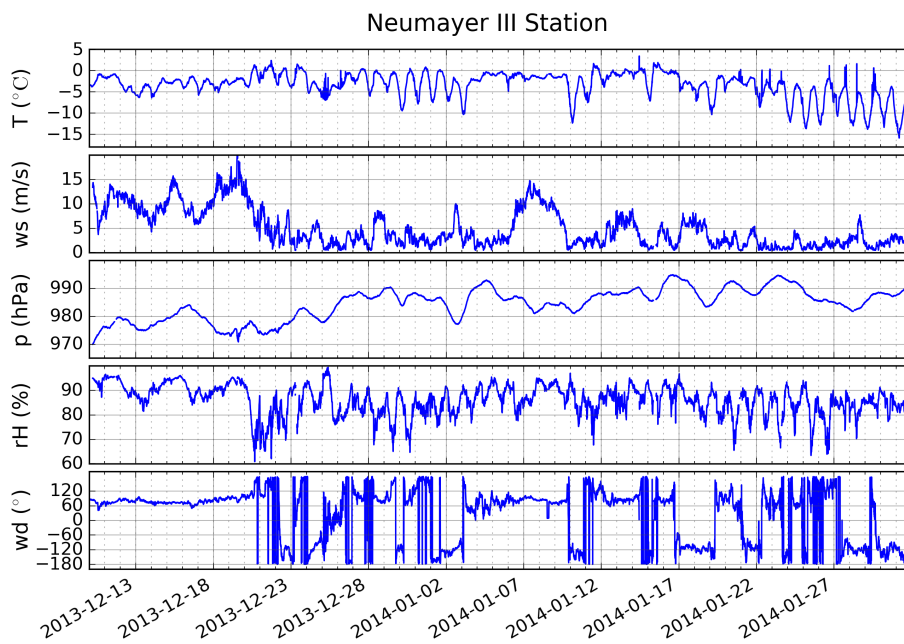


FIGURE D.2: AWS data from Neumayer III Station at 2m height from 13 December 2013 to 31 January 2014: 10 minute averages of temperature (T), wind speed (ws), pressure (p, minutewise), relative humidity (rH) with respect to water and wind direction (wd), based on (roughly corrected) minutewise data from König-Langlo (2014). Wind dir: 0° from north, 90° from east, $\pm 180^\circ$ from south, -90° from west.

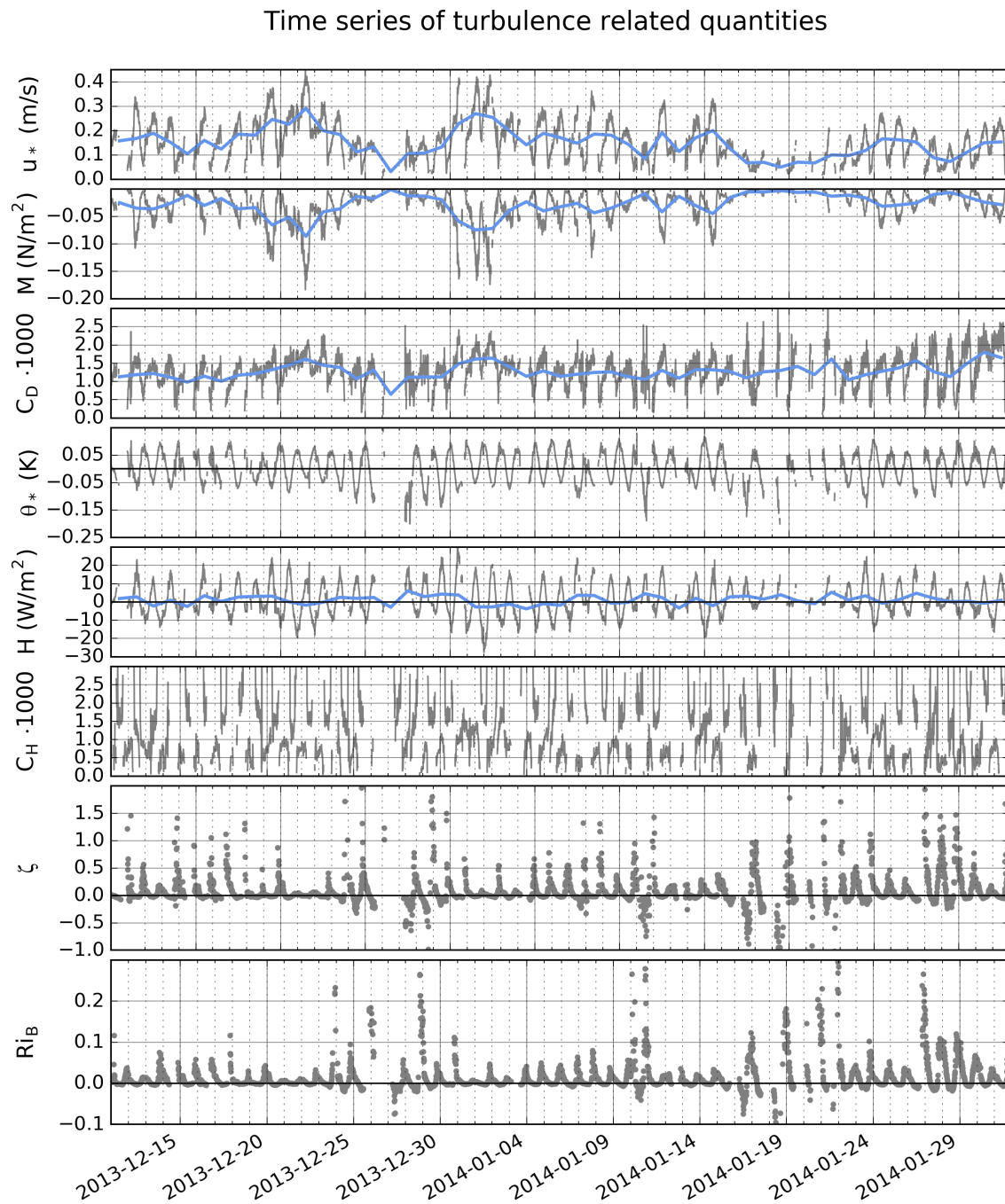


FIGURE D.3: Time series of turbulence related quantities as measured by the sonic anemometer-thermometer from 13 December 2013 to 31 January 2014 at 1.9m height. Daily means indicated as blue line. Top down: friction velocity, vertical turbulent momentum flux, drag coefficient (at 1.9 m height), turbulent temperature scale, sensible heat flux, bulk transfer coefficient for heat (at 1.9 m height, also dependent on surface temperature, $\varepsilon = 0.97$), stability parameter z/L , bulk Richardson number (also dependent on surface temperature).

APPENDIX E

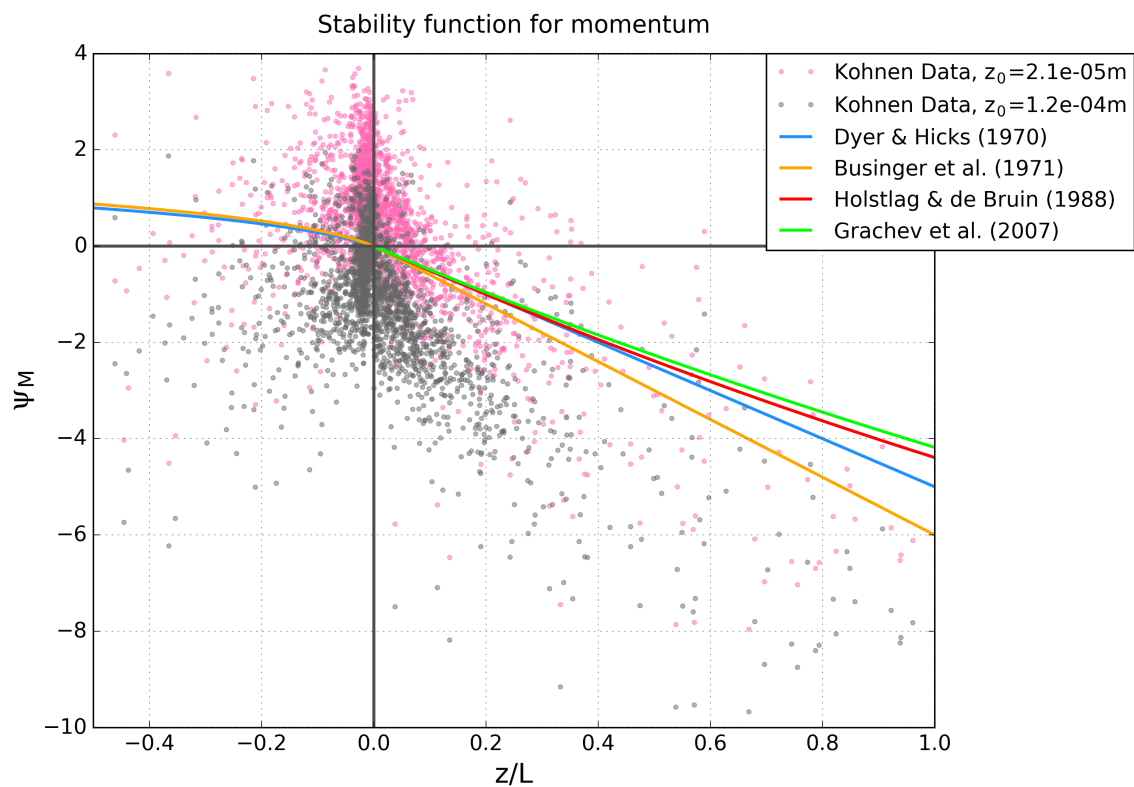
Linear depiction of measured ψ_M 

FIGURE E.1: Measured stability function for momentum vs. z/L (linear scale).

Bibliography

Andreas, E. L.

1987. A theory for the scalar roughness and the scalar transfer coefficients over snow and sea ice. *Boundary-Layer Meteorology*, 38:159–184.

Andreas, E. L., T. W. Horst, A. A. Grachev, P. O. G. Persson, C. W. Fairall, P. S. Guest, and R. E. Jordan

2010. Parametrizing turbulent exchange over summer sea ice and the marginal ice zone. *Q. J. R. Meteorol. Soc.*, 136:927–943.

Arck, M. and D. Scherer

2001. A physically based method for correcting temperature data measured by naturally ventilated sensors over snow. *Journal of Glaciology*, 159:665–670.

Argentini, S., I. Petenko, A. Viola, G. Mastrantonio, I. Pietroni, G. Casasanta, E. Aristidi, and C. Ghenton

2013. The surface layer observed by a high-resolution sodar at dome c, antarctica. *Annals of Geophysics*, 56(5).

Argentini, S., I. V. Petenko, G. Mastrantonio, V. A. Bezverkhii, and A. P. Viola

2001. Spectral characteristics of east antarctica meteorological parameters during 1994. *Journal of Geophysical Research: Atmospheres*, 106(D12):12463–12476.

Argentini, S., A. Viola, A. M. Sempreviva, and I. Petenko

2005. Summer boundary-layer height at the plateau site of dome c, antarctica. *Boundary-Layer Meteorology*, 115(3):409–422.

Ball, F. K.

1956. The theory of strong katabatic winds. *Australian Journal of Physics*, 9:373–386.

- Beljaars, A. C. M. and A. A. M. Holstlag
1991. Flux parametrization over land surfaces for atmospheric models. *Journal of Applied Meteorology*, Pp. 327–341.
- Belka Brea, M.
2015. The impact of snow specific surface area and clouds on snow albedo - investigations made at kohnen station, antarctica, during summer 2013/2014. Master's thesis, Marine Geosciences, University of Bremen.
- Birnbaum, G.
2013. Application for the expedition –meteorological measurements at kohnen station, dronning maud land 2013/2014– to the german federal environmental agency (umweltbundesamt), including attachments.
- Birnbaum, G., R. Brauner, and H. Ries
2006. Synoptic situations causing high precipitation rates on the antarctic plateau: observations from kohnen station, dronning maud land. *Antarctic science*, 18(2):279–288.
- Birnbaum, G., J. Freitag, R. Brauner, G. König-Langlo, E. Schulz, S. Kipfstuhl, H. Oerter, C. H. Reijmer, E. Schlosser, S. H. Faria, R. H., B. Loose, A. Herber, M. G. Duda, J. G. Powers, K. W. Manning, and M. R. van den Broeke
2010. Strong-wind events and their influence on the formation of snow dunes: Observations from kohnen station, dronning maud land, antarctica. *Journal of Glaciology*, 56(199):891–902.
- Bonner, C. S., M. C. B. Ashley, X. Cui, L. Feng, X. Gong, J. S. Lawrence, D. M. Luong-Van, Z. Shang, J. W. V. Storey, L. Wang, H. Yang, J. Yang, X. Zhou, and Z. Zhu
2010. Thickness of the atmospheric boundary layer above dome a, antarctica, during 2009. *Publications of the Astronomical Society of the Pacific*, 122:1122–1131.
- Bremerhaven, A.
. Description of kohnen station.
- Businger, J. A., J. C. Wyngaard, Y. Izumi, and E. F. Bradley
1971. Flux-profile relationships in the atmospheric surface layer. *Journal of the Atmospheric Sciences*, 28:181–189.
- Carleton, A. M. and D. A. Carpenter
1990. Satellite climatology of ‘polar lows’ and broadscale climatic associations for the southern hemisphere. *Int. J. Climatol.*, 10(3):219–246.
- Chamberlain, A. C.
1983. Roughness length of sea, sand and snow. *Boundary-Layer Meteorology*, 25:405–9.

Dyer, A. J.

1974. A review of flux-profile relationships. *Boundary-Layer Meteorology*, 7:363–372.

Erbrecht, R., H. König, K. Martin, W. Pfeil, and W. Würstenfeld

1999. *Das grosse Tafelwerk, Formelsammlung fuer die Sekundarstufe I und II [German] (Collection of scientific formulas for school/college)*, 1 edition. Berlin, Germany: Volk und Wissen.

Etling, D.

2008. *Theoretische Meteorologie, Eine Einführung*, 3 edition. Berlin Heidelberg: Springer.

Foken, T.

2006. 50years of the monin–obukhov similarity theory. *Boundary-Layer Meteorology*, 119:431–447.

Foken, T., M. Aubinet, and R. Leuning

2012. The eddy covariance method. In *Eddy Covariance: A Practical Guide to Measurement and Data Analysis*, M. Aubinet, T. Vesala, and D. Papale, eds., chapter 1. Springer Atmospheric Sciences.

Gallée, H., S. Preunkert, S. Argentini, M. M. Frey, C. Genthon, B. Jourdain, I. Pietroni, G. Casasanta, H. Barral, E. Vignon, C. Amory, and M. Legrand

2015. Characterization of the boundary layer at dome c (east antarctica) during the opale summer campaign. *Atmos. Chem. Phys. (EGU Open Access)*, 15:6225–6236.

Garratt, J. R.

1992. *The atmospheric boundary layer*. Cambridge University Press.

Garratt, J. R. and R. A. Brost

1981. Radiative cooling effects within and above the nocturnal boundary layer. *Journal of Atm. Sciences*, 38:2370–2745.

Genthon, C., D. Six, H. Gallée, P. Grigioni, and A. Pellegrini

2013. Two years of atmospheric boundary layer observations on a 45-m tower at dome c on the antarctic plateau. *Journal of Geophysical Research: Atmospheres*, 118(8):3218–3232.

Georges, C. and G. Kaser

2002. Ventilated and unventilated air temperature measurements for glacier-climate studies on a tropical high mountain site. *Journal of Geophysical Research*, 107(D24):4775.

- Grachev, A. A., E. L. Andreas, C. W. Fairall, P. S. Guest, and P. O. G. Persson
2007. Sheba flux-profile relationships in the stable atmospheric boundary layer. *Boundary-Layer Meteorology*, 124:315–333.
- Gryanik, V. M. and C. Lüpkes
2017. An efficient bulk parametrization of surface fluxes for stable atmospheric conditions based on grachev et al. (2007) stability functions. *Boundary-Layer Meteorology*, submitted.
- Handorf, D.
1996. Zur parametrisierung der stabilen atmosphärischen grenzschicht ueber einem antarktischen schelfeis [german] (parametrization of the stable atmospheric boundary layer over an antarctic ice shelf). Technical report, Alfred-Wegener-Institut fuer Polar- und Meeresforschung, Bremerhaven. Berichte zur Polarforschung 204 (Reports an Polar Research 204).
- Handorf, D., T. Foken, and C. Kottmeier
1999. The stable atmospheric boundary layer over an antarctic ice sheet. *Boundary-Layer Meteorology*, 91(2):165–189.
- Hock, R., ed.
1994. *Comparison of ventilated and unventilated temperature measurements*. Dep. of Phys. Geogr., Stockholm Univ., Stockholm.
- Holstlag, A. A. M. and D. B. H. A. R.
1988. Applied modeling of the nighttime surface energy balance over land. *Journal of Applied Meteorology*, 27:689–704.
- Holton, J. R.
2004. *An Introduction to Dynamic Meteorology*, 4 edition. Elsevier Academic Press.
- Holtslag, A. A. M., G. Svensson, P. Baas, S. Basu, B. Beare, A. C. M. Beljaars, F. C. Bosveld, J. Cuxart, J. Lindvall, G. J. Steeneveld, M. Tjernström, and B. J. H. Van De Wiel
2013. Stable atmospheric boundary layers and diurnal cycles: Challenges for weather and climate models. *Bulletin of the American Meteorological Society*, 94(11):1691–1706.
- Hori, M., T. Aoki, T. Tanikawa, H. Motoyoshi, A. Hachikubo, K. Sugiura, T. J. Yasunari, H. Eide, R. Storvold, Y. Nakajima, and F. Takahashi
2006. In-situ measured spectral directional emissivity of snow and ice in the 8–14 micrometer atmospheric window. *Remote Sensing of Environment*, 100(4):486 – 502.

- Hudson, S. R. and R. E. Brandt
2005. A look at the surface-based temperature inversion on the antarctic plateau. *Journal of Climate*, 18(11):1673–1696.
- Huwald, H., C. W. Higgins, M.-O. Boldi, E. Bou-Zeid, M. Lehning, and M. B. Parlange
2009. Albedo effect on radiative errors in air temperature measurements. *Water resources research*, 45(W09431).
- Kaijo Denki Co., L.
before 1995. *Instruction manual, Digitized Ultrasonic Anemometer Thermometer Model DAT-300*. Tokyo, Japan.
- Kaimal, J. C. and J. J. Finnigan
1994. *Atmospheric Boundary Layer Flows - Their structure and measurement*. Oxford University Press.
- King, J. and J. Turner
1997. *Antarctic Meteorology and Climatology*. Cambridge University Press.
- König-Langlo, G.
2014. Continuous meteorological observations at neumayer station 2013-12 and 2014-01. Technical report, Alfred Wegener Institute, Helmholtz Center for Polar and Marine Research, Bremerhaven. accessed through <https://pangaea.de/>, info: <http://www.awi.de/en/science/long-term-observations.html>.
- Kraus, H.
2004. *Die Atmosphäre der Erde, Eine Einführung in die Meteorologie [German] (Die Earth's atmosphere, an Introduction to Meteorology)*, 3 edition. Berlin, Heidelberg: Springer.
- Kraus, H.
2008. *Grundlagen der Grenzschicht-Meteorologie [German] (Introduction to Boundary Layer Meteorology)*. Berlin Heidelberg: Springer.
- Louis, J. F.
1979. A parametric model of vertical eddy fluxes in the atmosphere. *Boundary Layer Meteorology*, 17:187–202.
- Mahrt, L.
1999. Stratified atmospheric boundary layers. *Boundary-Layer Meteorology*, 90:375–396.

- Mastrantonio, G., V. Malvestuto, S. Argentini, T. Georgiadis, and A. Viola
1999. Evidence of a convective boundary layer developing on the antarctic plateau during the summer. *Meteorology and Atmospheric Physics*, 71(1):127–132.
- Mauritsen, T. and G. Svensson
2007. Observations of stably stratified shear-driven atmospheric turbulence at low and high richardson numbers. *Journal of the Atmospheric Sciences*, 64(2):645–655.
- Metek, G.
2006. *Manual of USA-1 Ultrasonic anemometer*. Elmshorn, Germany.
- Monin, A. S. and A. M. Obukhov
1954. Basic laws of turbulent mixing in the atmospheric surface layer. *Trudy Geofiz. Inst. Akad. Nauk SSSR*, 24(151):163–187.
- Munger, J. W., H. W. Loeschner, and H. Luo
2012. Measurement, tower, and site design considerations. In *Eddy Covariance: A Practical Guide to Measurement and Data Analysis*, M. Aubinet, T. Vesala, and D. Papale, eds., chapter 2. Springer Atmospheric Sciences.
- Noone, D., J. Turner, and R. Mulvaney
1999. Atmospheric signals and characteristics of accumulation in dronning maud land, antarctica. *Journal of Geophysical Research*, 104(D16)(19):191–211.
- Oerter, H., F. Wilhelms, F. Jung-Rothenhäusler, F. Göktas, H. Miller, W. Graf, and S. Sommer
2000. Accumulation rates in dronning maud land, antarctica, as revealed by dielectric-profiling measurements at shallow firn cores. *Annales of Glaciology*, 30:27–34.
- Oke, T. R.
1987. *Boundary Layer Climates, Second Edition*. Routledge.
- Phillpot, H. R. and J. W. Zillman
1970. The surface temperature inversion over the antarctic continent. *Journal of Geophysical Research*, 75(21):4161–4169.
- Pietroni, I., S. Argentini, and I. Petenko
2014. One year of surface-based temperature inversions at dome c, antarctica. *Boundary-Layer Meteorology*, 150:131–151.
- Rebmann, C., O. Kolle, B. Heinesch, M. Aubinet, R. Queck, and A. Ibrom
2012. Data acquisition and flux calculations. In *Eddy Covariance: A Practical Guide to Measurement and Data Analysis*, M. Aubinet, T. Vesala, and D. Papale, eds., chapter 3. Springer Atmospheric Sciences.

Reijmer, C. and M. van den Broeke

2003. Temporal and spatial variability of the surface mass balance in dronning maud land, antarctica, as derived from automatic weather stations. *Journal of Glaciology*, 49(167):512–520.

Rodrigo, J. S. and P. S. Anderson

2013. Investigation of the stable atmospheric boundary layer at halley antarctica. *Boundary-Layer Meteorology*, 148:517–539.

Schlosser, E., K. W. Manning, J. G. Powers, M. G. Duda, G. Birnbaum, and K. Fujita

2010. Characteristics of high-precipitation events in dronning maud land, antarctica. *Journal of Geophysical Research*, 115(D14107).

Sinclair, M. R.

1994. An objective cyclone climatology for the southern hemisphere. *Mon. Weather Rev.*, 122(10):2239–2256.

Steenefeld, G. J., M. J. J. Wokke, C. D. Groot Zwaafink, S. Pijlman, B. G. Heusinkveld, A. F. G. Jacobs, and A. A. M. Holtslag

2010. Observations of the radiation divergence in the surface layer and its implication for its parameterization in numerical weather prediction models. *Journal of Geophysical Research: Atmospheres*, 115(D6).

Stull, R. B.

1988. *An Introduction to Boundary Layer Meteorology*. Dordrecht, The Netherlands: Kluwer Academic Publishers.

van As, D. and M. R. van den Broeke

2006. Structure and dynamics of the summertime atmospheric boundary layer over the antarctic plateau: 2. heat, moisture, and momentum budgets. *Journal of Geophysical Research: Atmospheres*, 111(D7).

van As, D., M. R. van den Broeke, and M. M. Helsen

2006. Structure and dynamics of the summertime atmospheric boundary layer over the antarctic plateau: 1. measurements and model validation. *Journal of Geophysical Research: Atmospheres*, 111(D7).

van As, D., M. R. van den Broeke, and M. M. Helsen

2007. Strong-wind events and their impact on the near-surface climate at kohnen station on the antarctic plateau. *Antarctic Science*, 19(4):507–519.

- van As, D., M. R. van den Broeke, C. Reijmer, and R. Van de Wal
2005. The summer surface energy balance of the high antarctic plateau. *Boundary-Layer Meteorology*, 115:289–317.
- van den Broeke, M., C. Reijmer, D. Van As, and W. Boot
2006. Daily cycle of the surface energy balance in antarctica and the influence of clouds. *International Journal of Climatology*, 26:1587–1605.
- van den Broeke, M., D. Van As, C. Reijmer, and R. Van de Wal
2005. Sensible heat exchange at the antarctic snow surface: a study with automatic weather stations. *International Journal of Climatology*, 25:1081–1101.
- van den Broeke, M. R. and N. P. M. van Lipzig
2003. Factors controlling the near-surface wind field in antarctica. *Monthly Weather Review Am. Met. Soc.*, 131(4):733–743.
- Vignon, E., C. Genthon, H. Barral, C. Amory, G. Picard, H. Gallée, G. Casasanta, and S. Argentini
2016. Momentum- and heat-flux parametrization at dome c, antarctica: A sensitivity study. *Boundary-Layer Meteorology*.
- Wacker, U., H. Ries, and U. Schättler
2006. Precipitation simulation for dronning maud land using the cosmo-model. *Antarctic Science*, 21(6):643–662.

.

Nachname _____ Matrikelnr. _____
Vorname/n _____

Diese Erklärungen sind in jedes Exemplar der Bachelor- bzw. Masterarbeit mit einzubinden.

Urheberrechtliche Erklärung

Hiermit versichere ich, dass ich die vorliegende Arbeit selbstständig verfasst und keine anderen als die angegebenen Quellen und Hilfsmittel verwendet habe.

Alle Stellen, die ich wörtlich oder sinngemäß aus anderen Werken entnommen habe, habe ich unter Angabe der Quellen als solche kenntlich gemacht.

Datum

Unterschrift

Erklärung zur Veröffentlichung von Abschlussarbeiten

Die Abschlussarbeit wird zwei Jahre nach Studienabschluss dem Archiv der Universität Bremen zur dauerhaften Archivierung angeboten.

Archiviert werden:

- 1) Masterarbeiten mit lokalem oder regionalem Bezug sowie pro Studienfach und Studienjahr 10 % aller Abschlussarbeiten
- 2) Bachelorarbeiten des jeweils der ersten und letzten Bachelorabschlusses pro Studienfach und Jahr.

- Ich bin damit einverstanden, dass meine Abschlussarbeit im Universitätsarchiv für wissenschaftliche Zwecke von Dritten eingesehen werden darf.
- Ich bin damit einverstanden, dass meine Abschlussarbeit nach 30 Jahren (gem. §7 Abs. 2 BremArchivG) im Universitätsarchiv für wissenschaftliche Zwecke von Dritten eingesehen werden darf.
- Ich bin nicht damit einverstanden, dass meine Abschlussarbeit im Universitätsarchiv für wissenschaftliche Zwecke von Dritten eingesehen werden darf.

Datum

Unterschrift